SOLAR MAGNETIC FIELDS - SOURCE, EVOLUTION, AND INTERACTION WITH PLANETARY MAGNETOSPHERES

Brandon Burkholder

A Dissertation Submitted in Partial Fulfillment of the Requirements for the Degree of

Doctor of Philosophy in Space Physics

University of Alaska Fairbanks

August 2019

APPROVED:

Peter Delamere, Committee Chair
Antonius Otto, Committee Member
David Newman, Committee Member
Chung-Sang Ng, Committee Member
Hyunju Connor, Committee Member
Renate Wackerbauer, Chair
Department of Physics
Leah Berman, Dean
College of Natural Sciences and Mathematics
Michael Castellini, *Dean of the Graduate School*

Abstract

Magnetized plasmas with twisted and filamented magnetic fields are pervasive throughout the heliosphere. In the solar magnetic field, photospheric convection on scale sizes from granules to differential rotation is responsible for driven magnetic reconnection. These reconnection sites are closely related to the magnetic topology, which is highly complex as the magnetic field is structured by a network of many thousands of magnetic flux concentrations. The coronal plasma overlying this "magnetic carpet" is the source of the solar wind flow, which has been found to be turbulent as close to the sun as our observations can currently resolve. At 1 AU, observations have also revealed a highly structured solar wind which we posit in this thesis originates in the corona rather than forming in-transit. Further, the solar wind-magnetosphere interaction depends on variability in the solar wind. When the boundary between solar wind plasma and magnetospheric plasma is unstable to the growth of Kelvin-Helmholtz waves, driven magnetic reconnection can occur on the magnetopause boundary. Such reconnection allows magnetic field to thread the boundary and transport can take place. We quantify the solar wind interaction for a corotation dominated system in terms of the mass and momentum transport driven by Kelvin-Helmholtz instabilities. Model-data comparisons are performed in this thesis using both the magnetohydrodynamic and hybrid-kinetic approaches for fluid simulations.

This page intentionally left blank.

Acknowledgements

I would like to give all credit where it is due, so I suppose I should start where my academic career really began, or at least at the point where teaching quality could influence my life goals. In high school I was inspired by Dr. Celeste MacMillan, my chemistry teacher, whose incredible knowledge made me respect what it meant to have a PhD. My calculus teacher Ted Guerard was the first person to really make me think hard about mathematics, and I have spent most of my waking hours doing so ever since! Growing up my time was mostly spent playing the incredible game of soccer, so I should thank John Devereux, Shilo Tisdale, and Nick Finotti for coaching me to the greatest victories in my life.

At Clemson I worked with Gerald Lehmacher on mesospheric turbulence and he brought me to Fairbanks to oversee assembly for the M-Tex sounding rocket mission. This wonderful visit to Alaska was a big reason why I ended up here for graduate school. My other college research advisor, Jeremy King, is the best teacher I have ever had. Taking a test from Prof King felt like show and tell rather than a stressful time limited problem set. In addition, I would have never been able to produce a large part of this thesis without a lot of training in computer science, which is due largely to Brian Malloy.

The first person that I befriended after moving to Fairbanks was a fellow physics graduate student, Randle Affholter. He provided me with countless hours of stimulating discussion on topics ranging from the origin of consciousness to plasma instabilities in the ionosphere. Without Randle, I would have never taken the fundamentals of plasma physics course during my first year, and likely pursued a whole different research path. I was deeply saddened when Randle was no longer able to continue as a graduate student. His friendship left a lasting impact on me because I am certain that his out of the box thinking is exactly what this world needs now and for the future.

I must thank Stefan Awender and Will Swanson. Between the two of them I made it to the skiing hill almost every weekend for three consecutive winters, and the many treks we made to Budweiser Rock will never be forgotten. My office-mates Nathan Barnes, Drew Coffin, and Bishwa Neupane were a pleasure to work alongside. Nathan has provided me insight on many difficult problems and is one of the most genuinely intelligent people I have ever known. I have

learned and forgotten so many amazing facts from Drew. Bishwa and I share a love of soccer, but his video feed is always ahead of mine and he tells me about the goals before I see them!

The teaching that I received as a student at UAF has been nothing short of outstanding. I particularly would like to note Renate Wackerbauer, Mark Conde, and Channon Price who were incredibly engaging and competent as classroom instructors. I should also mention that the math department at this university is excellent. Ed Bueler, David Maxwell, and John Rhodes each could rival for the namesake of my favorite teacher. I most certainly learned more in each of those three classes than any physics class I have taken.

I am extraordinarily grateful for the guidance and input of my committee members David Newman, Hyunju Connor, and Chung-Sang Ng. I would also like to thank Roman Makarevich for serving on my committee for a period. I have been helped along immensely by my coauthors Michelle Thomsen, Fran Bagenal, Rob Wilson, Joe Borovsky, and Jay Johnson, and deserving special attention are the many contributions of Xuanye Ma. I hope to continue working with all of these great people in the future. My mentor Antonius Otto provided a great deal of help cultivating the ideas of this thesis. We spent many hours on the phone from Alaska to Germany working through the technical details of my research. I am extremely grateful that he was willing to give me so much of his time and he did so with a passion that I hope to portray in my space physics career. In the words of Katariina Nykyri "I think he is one of the smartest people on this planet and should get the Nobel Prize." To my advisor Peter Delamere, I am forever indebted. His intellectual contribution to this thesis was significant, but the truly incredible portion of working with Peter was the chance to explore the Alaskan wilderness in extraordinary company.

Table of Contents

This page intentionally left blank.

List of Figures

This page intentionally left blank.

List of Tables

This page intentionally left blank.

List of Appendices

Page

This page intentionally left blank.

Chapter 1

Introduction

A common physical scenario which allows to describe many interesting phenomena in the universe is the conversion of one form of energy to another, to a state of the system which is energetically favorable. Nuclear and chemical reactions are some of the most interesting examples but the flowing of a stream downhill and a steady sea-breeze also represent a conversion of energy to relax some imbalance in the system. In a magnetized plasma, energy in the magnetic field can be converted into kinetic and thermal energy in a process called magnetic reconnection. Non-equilibrium states of the plasma can be relaxed due to reconnection, as was systematically studied in the Geospace Environmental Modeling (GEM) Magnetic Reconnection Challenge (*Birn et al.*, 2001), while an injection of energy can lead to driven reconnection.

Magnetic reconnection involves the annihilation of magnetic field and allows plasma to be transported across a boundary with no magnetic connection. An illustration of the typical reconnection configuration is given in Figure 1.1. As anti-parallel field lines ℓ_1 and ℓ_2 come together, ion and electron motions are allowed to decouple in some small region (the diffusion region) surrounding the "X" point. Note that associated with this X-point are a pair of field lines which cross, defining the infinitesimally thin boundary between magnet-

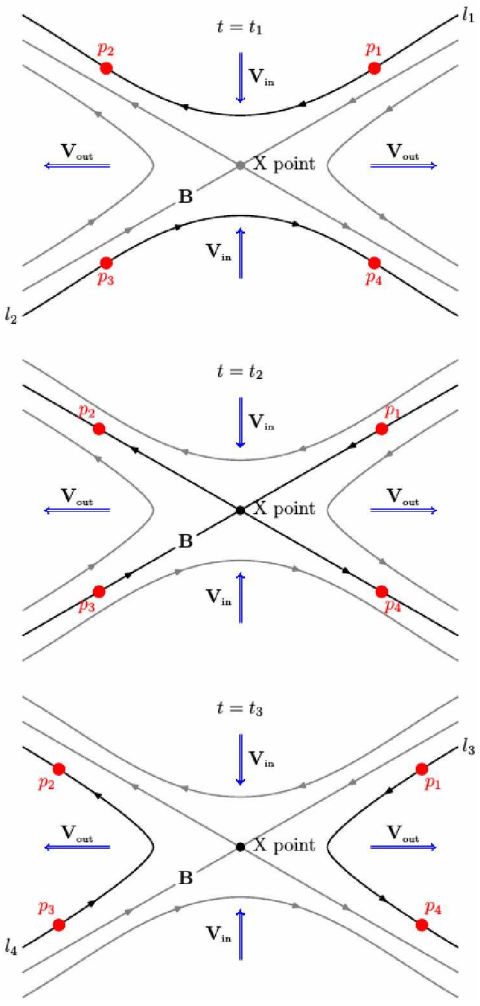

Figure 1.1: Sketch of two-dimensional magnetic reconnection. *Reproduced from Ma* (2012).

ically disconnected regions. These field lines are called separatrix field lines and for one instant of time, the field lines ℓ_1 and ℓ_2 define the separatrices. After the reconnection event takes place, it is as if ℓ_1 and ℓ_2 have been snipped in half and tied to one another. The changing connection is understood by considering the points $p_1 - p_4$. Initially, p_1 and p_2 lie on the same field line but after the reconnection event p_1 and p_4 lie on the same field line. Similarly, p_3 and p_4 initially lie on the same field line but after the reconnection event p_2 and p_3 lie on the same field line.

In a collisionless space plasma the kinetic physics in the diffusion region can be modeled in the framework of magnetohydrodynamics (MHD) by including a resistive term in the Ohm's law. While most space plasmas can be considered infinitely conducting, this allows to perform simulations using far less computational power than a fully kinetic simulation. In this thesis, we will perform such simulations of driven reconnection on the sun but also use a hybrid-kinetic simulation to study driven reconnection in the Kelvin-Helmholtz instability. The hybrid simulation includes some of the additional physics in a reconnection layer which the MHD framework reproduces only through an ad hoc resistivity.

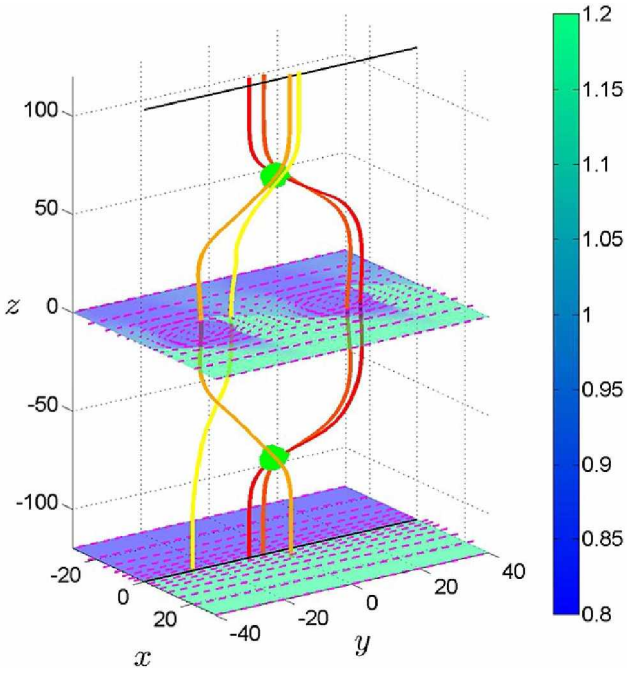

Figure 1.2: "Candy wrapper" reconnection driven by the Kelvin-Helmholtz instability can occur in three-dimensions. *Images reproduced from Ma et al.* (2015).

One straighforward way to drive reconnection is with a vortical flow. In an initially uniform magnetic field, a twisting motion produces anti-parallel magnetic field components that are responsible for a thin current sheet. An example of this is given in Figure 1.2, where field lines tied at both boundaries are perturbed by vortical plasma flows in the center of the simulation. Continuous driving can lead to the onset of reconnection for sufficiently twisted magnetic field lines (intense current density). During such driven reconnection the rate of magnetic flux transfer across the X-point, known as the reconnection rate, has been shown to be insensitive to the inclusion of kinetic physics or Hall physics (*Ma et al.*, 2014a,b). In the following chapters we consider the effects of driven reconnection in the context of magnetic field line connectivity and transport properties,

particularly in the solar corona and at the magnetopause boundary of a fast rotating magnetodisc, both of which are environments driven by vortical flows.

1.1 The Highly Structured Solar Wind

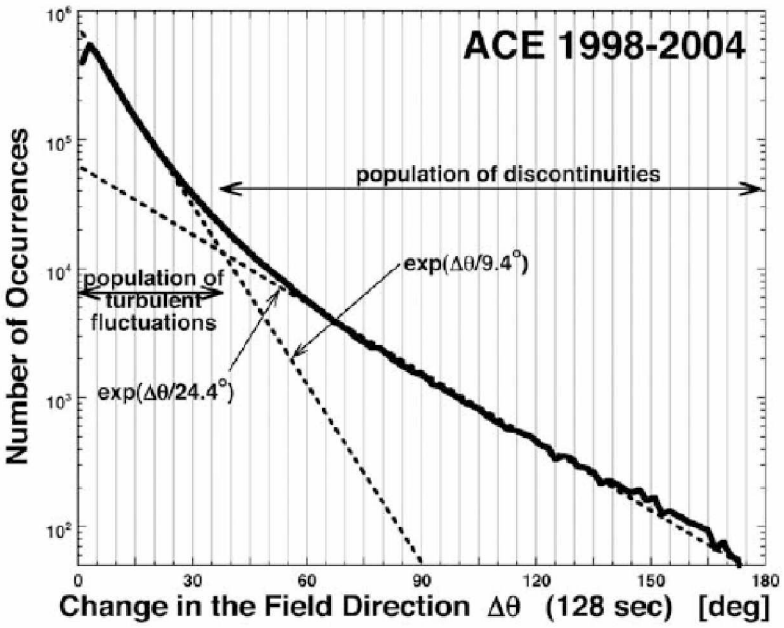

Figure 1.3: Solar wind magnetic field changes. *Reproduced from Borovsky* (2008).

The solar wind is a stream of charged particles and magnetic fields that emanates in all directions from the sun. Characteristics of the flow can fluctuate in tandem with the 11-year solar cycle. In addition, a spacecraft observing the solar wind from a fixed position with respect to the sun will find large variability over short time scales. The question of the origin of the small scale variability remains open (*Owens et al.*, 2011; *Neugebauer and Giacalone*, 2010; *Arnold et al.*, 2013). Some argue that in-transit effects are largely responsible for the observed structure while others contend that it is the fossilized remnant of coronal magnetic fields and plasma (*Borovsky*, 2008).

A picture of this variability is given in Figures 1.3 and 1.4 using 6 years of solar wind observations from the Advanced Composition Explorer (ACE). This spacecraft orbits the L1 point and constantly monitors the solar wind by collecting particles and measuring magnetic fields. Figure 1.3 shows the distribution of angular change in the magnetic field direction for 128 second intervals. The distribution shows a population of large magnetic field rotations that has a distinct slope from the small angle rotations. A number of other properties as given in Figure 1.4 show similar distributions.

It is postulated that the population of large changes in magnetic field and plasma are the spacecraft passing through the boundary between flux tubes with different origins on the solar surface (*Bruno et al.*, 2001; *Borovsky*, 2008). These different origins would be responsible for the different magnetic fields and plasmas inside the flux tubes. The population of small changes are hypothesized as turbulent fluctuations in the solar wind rather than its intrinsic structure. Compelling evidence that these flux tubes are seeded into the solar wind in the corona is given in Figure 1.5. In the left panel, the wall-to-wall distances for successive flux tube boundaries is mapped back to the sun. The comparison between other scales indicates that flux tube sizes map to the scale of granules and supergranules on the solar surface. The right panel shows magnetic flux contained within the solar wind flux tubes and concentrations of magnetic flux observed in the solar magnetic carpet. The distributions are remarkably similar for the range of observations and it is assumed that greater resolution would continue this trend for smaller values of magnetic flux.

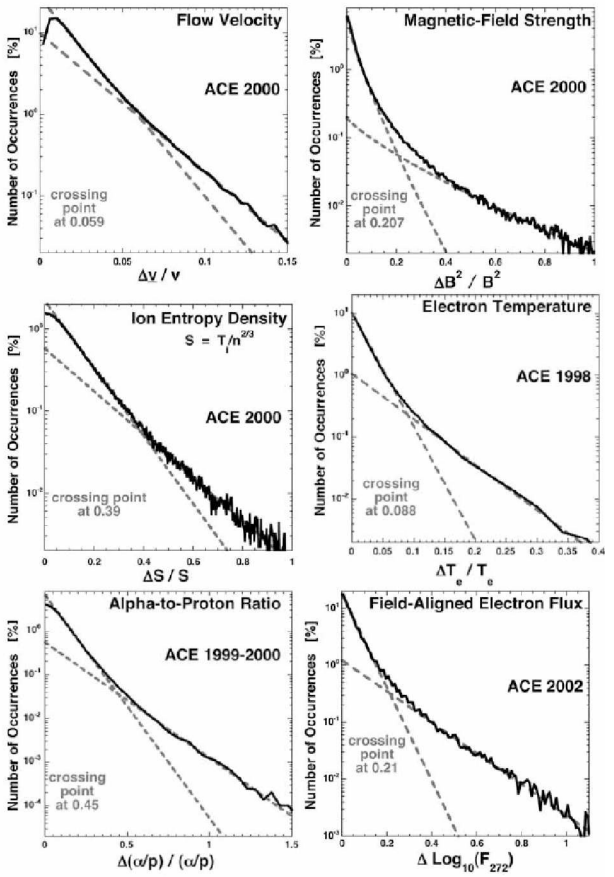

Figure 1.4: Solar wind magnetic field and plasma property changes. *Reproduced from Borovsky* (2008).

Chapter 2 of this thesis uses numerical simulations to understand the origin of flux tube boundaries in the solar wind, specifically the role that magnetic topological boundaries in the sun's corona can play in sourcing solar wind structure (*Burkholder et al.*, 2018). Chapter 3 is a continuation of this investigation, focusing more on the time-dependent connection of a flux tube, and the exact form of structure that would be observed at such boundaries. This chapter concludes with a model-data comparison of solar wind current sheets at 1 AU using the Magnetospheric Multi-Scale spacecraft constellation (*Burkholder and Otto*, Submitted - 2019).

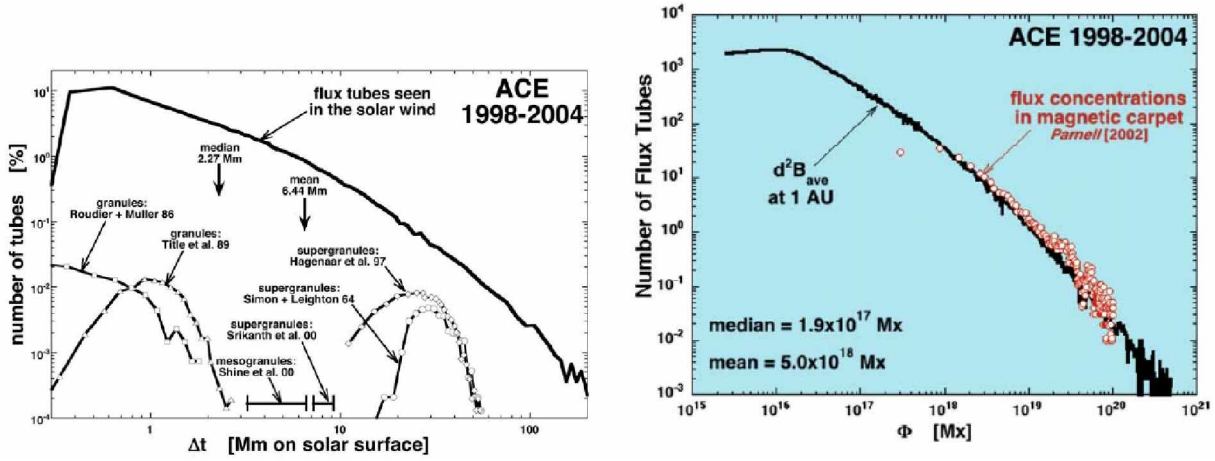

Figure 1.5: Correlation of solar wind flux tubes to features of the solar atmosphere. *Reproduced from Borovsky* (2008).

1.2 Solar Wind Flow Past an Obstacle

The typical picture for comparative magnetospheric studies is given by Figure 1.6 and a vast store of knowledge on the subject is contained in *Keiling et al.* (2015). This graphic shows the marked difference in scales between Mercury, Earth, and the outer planet magnetospheres generated by the difference in internal magnetic fields for these bodies. A stronger magnetic field provides more magnetic pressure to balance with solar wind dynamic pressure. At Jupiter and Saturn, the magnetospheric cavity is puffed up even more by pressure exerted from internally sourced plasma. These examples only provide a picture of the different magnetized obstacles which the solar wind will encounter. There are also unmagnetized bodies like comets and Earth's moon whose interactions are the results of mass loading and electrical conductivity.

The dynamic pressure of the solar wind flow exerts a force on anything in its path but the coupling can also be facilitated by the magnetic field. As a first example, consider the interplanetary magnetic field (IMF) interacting with an unmagnetized body, such as the comet shown in Figure 1.7. The coma of ionized gas surrounding a comet mass loads the magnetized solar wind flow with stationary ions. The pick-up process drapes magnetic field lines around the obstacle as momentum is transported from the high-speed solar wind. A similar interaction can occur for a non-magnetized body lacking an atmopshere such as the moon or an asteroid. In this case the field lines do not drape, but rather are perturbed in the wake of the body where a void forms in the flow.

The comet example provides a good starting point for how the solar wind can "sink its teeth" into an obstacle through an electromagnetic interaction. The next important example is the solar wind flowing by a magnetized body, and the best studied case is the terrestrial

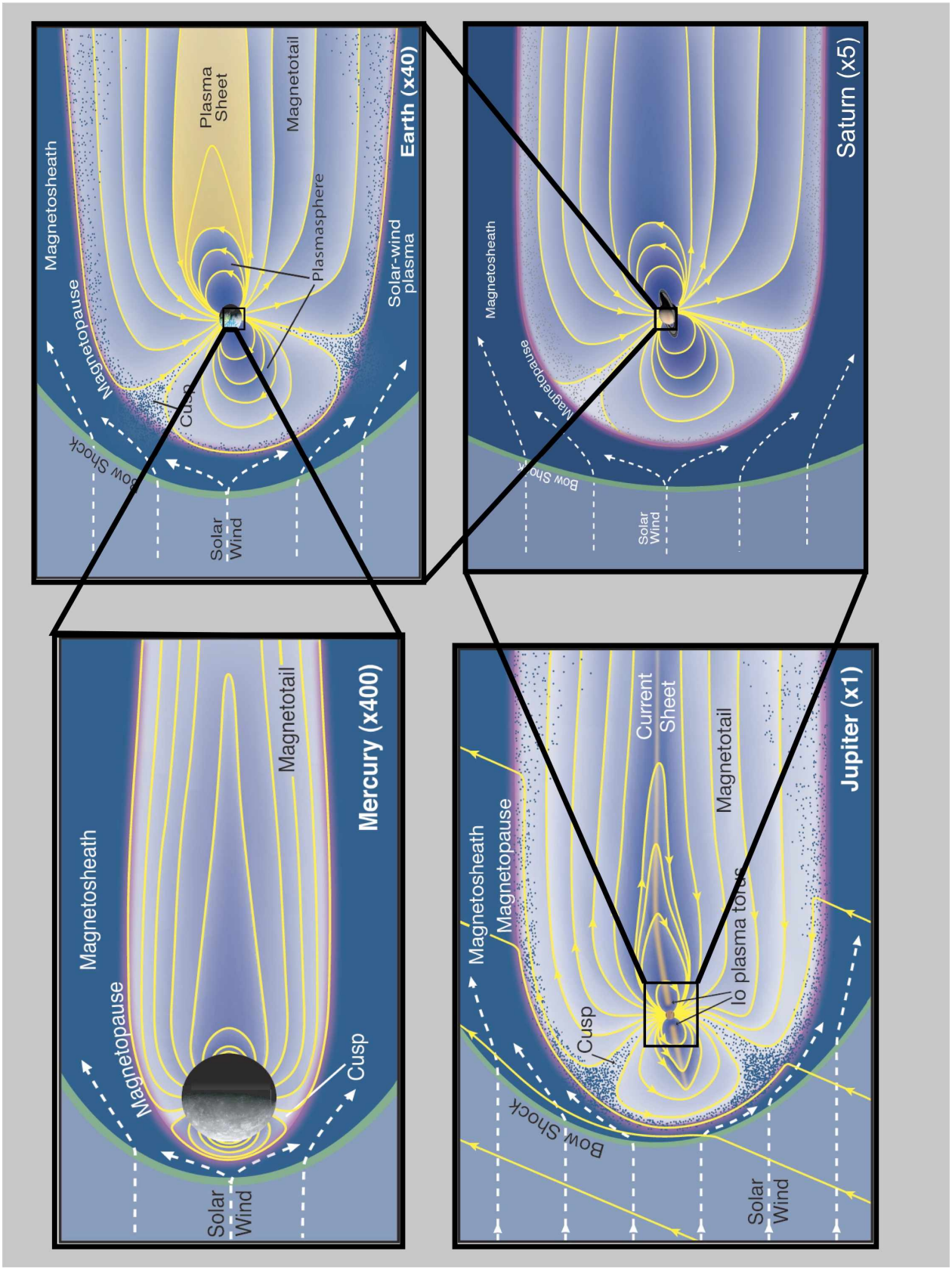

Figure 1.6: Relative sizes of magnetospheres throughout the solar system. *Image credit* Fran Bagenal and Steve Bartlett.

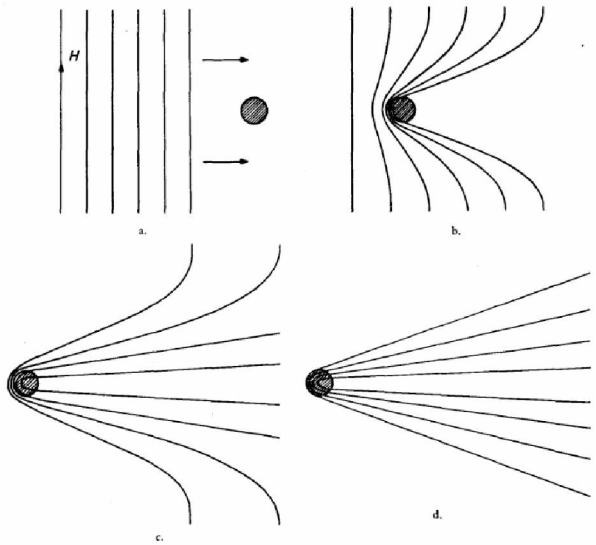

Figure 1.7: Interplanetary magnetic field lines draping around a non-magnetized obstacle. *Reproduced from Alfvén* (1957).

magnetosphere, where the Dungey cycle (*Dungey*, 1961) of magnetic flux circulation dominates. The solar wind grabs hold of Earth's magnetosphere through large scale magnetic reconnection that proceeds in a fashion dependent on the specific parameters of the solar wind. In this process polar cap flux is connected to IMF and advected into the magnetotail with the solar wind flow. The reconnection sites and pattern of flow produced in the ionosphere are dependent on the direction of the IMF, so it is important to note that the classic case of B_z aligned opposite to Earth's dipole field given by Figure 1.8 only applies to a steady solar wind. In this Figure, the numbers 1-3 show an IMF field line being pressed against the magnetopause which is subsequently reconnected and swept downtail. The numbers 4-6 begin with another reconnection event in the tail which launches a plasmoid and the release of tension on the field line means it snaps into the inner magnetosphere. Finally 7 shows the field line circulates back to the dayside and completes the Dungey cycle. In Figure 1.9, the circulation pattern of a magnetic field line is illustrated in three-dimensions, showing how a field line reconnected in the tail can be brought back to the dayside magnetopause. Through this cycle, the solar wind can be considered the most important driver in the system.

At the outer planet magnetospheres, the solar wind has been flowing for a week or more since leaving the corona but still contains plenty of structure and variability (*McComas et al.*, 2014). As it passes by Jupiter and Saturn, the interaction that takes place is different than the interaction at Earth due in part to the much larger size of the obstacle (*Masters*, 2018). The moons Io of Jupiter and Enceladus of Saturn feed material that is ionized, magnetized with the planetary dipole, and centrifugally confined to create a fast rotating magnetodisc.

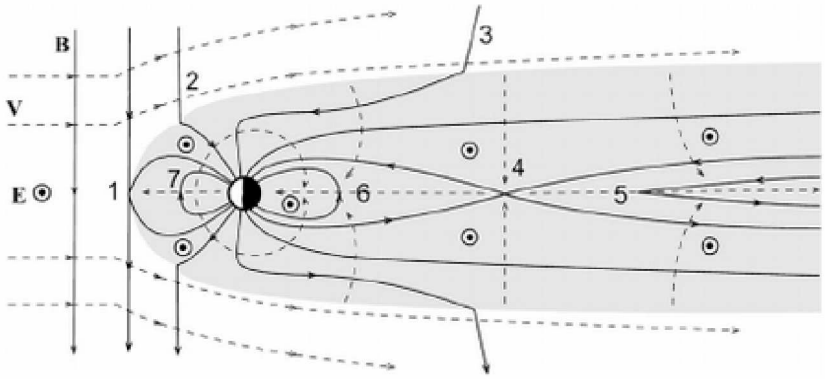

Figure 1.8: The Dungey cycle of magnetic flux circulation. *Reproduced from Seki et al.* (2015).

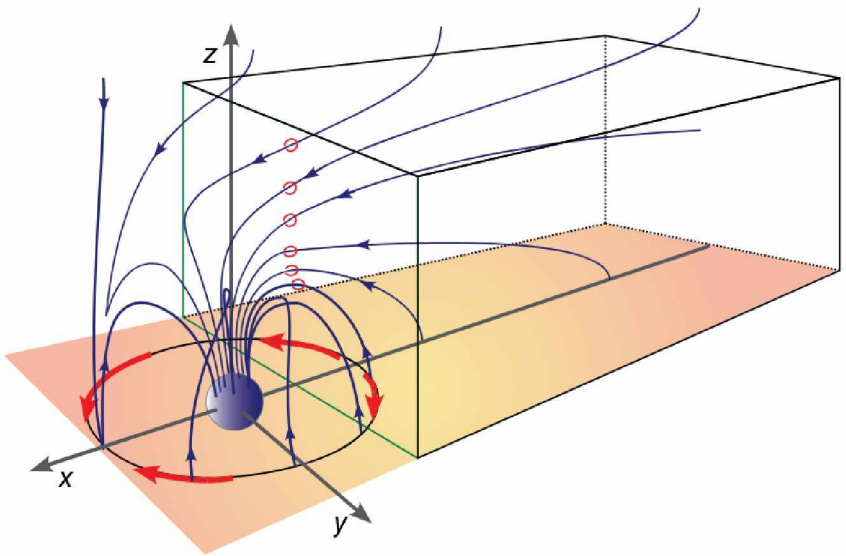

Figure 1.9: Three-dimensional circulation pattern of the Dungey cycle.

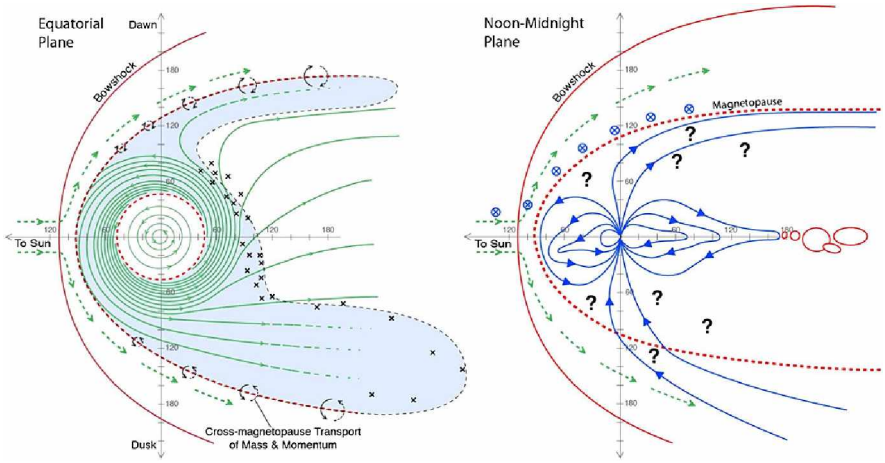

Figure 1.10: The fast rotating magnetodisc configurations of Jupiter and Saturn's magnetospheres. *Reproduced from Delamere et al.* (2013).

At the magnetopause boundary a shear flow exists between the subcorotating magnetospheric plasma and solar wind flow which has important consequences for the coupling.

The left panel of Figure 1.10 shows the equatorial plane for a magnetosphere of this type (*Delamere and Bagenal*, 2013). Green streamlines show the paths for particles generated by the source in the inner magnetosphere. The solar wind grabs hold of this magnetosphere mainly through a viscous interaction facilitated by intermittent reconnection on the magnetopause boundary (*Delamere and Bagenal*, 2010). This transports mass and momentum across the boundary in a two way process. The first part of chapter 4 in this thesis uses Cassini plasma data to understand the momentum budget near Saturn's magnetopause. The right panel of Figure 1.10 shows a structure of open flux that would exist where a Dungey cycle interaction is important. Since an open polar cap is not observed this picture is under question, which will be discussed in the conclusion of this thesis. Because of the large size of the obstacle, steady state Dungey-type reconnection is never established because the time to advect a reconnected field line down tail is far too long compared to the characteristic time scale for variability in the solar wind (*Delamere et al.*, 2015a; *Masters*, 2018).

1.3 Kelvin-Helmholtz Waves on Saturn's Magnetopause

Without taking into account the negligible contribution of Dungey-type reconnection, no magnetic field threads the magnetopause boundary and therefore plasma that is frozen-in to magnetic field lines must all be deflected around the obstacle. However, the shear flow between shocked solar wind plasma and subcorotating magnetospheric plasma excites Kelvin-Helmholtz instabilities (whose growth rate is derived in Appendix A) which drive

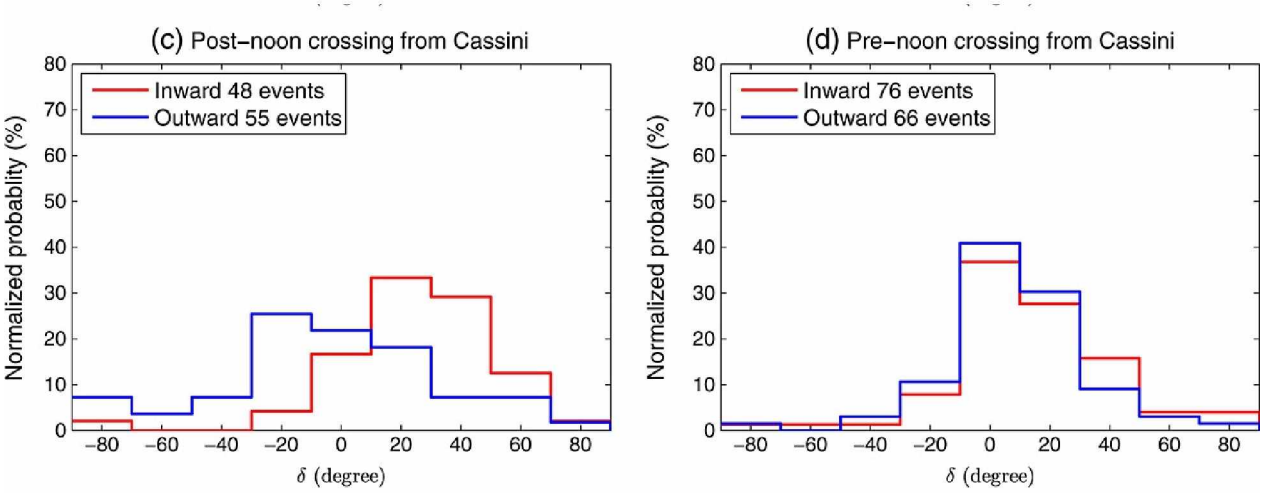

Figure 1.11: Boundary normal direction for Cassini magnetopause boundary encounters. *Reproduced from Ma et al.* (2015).

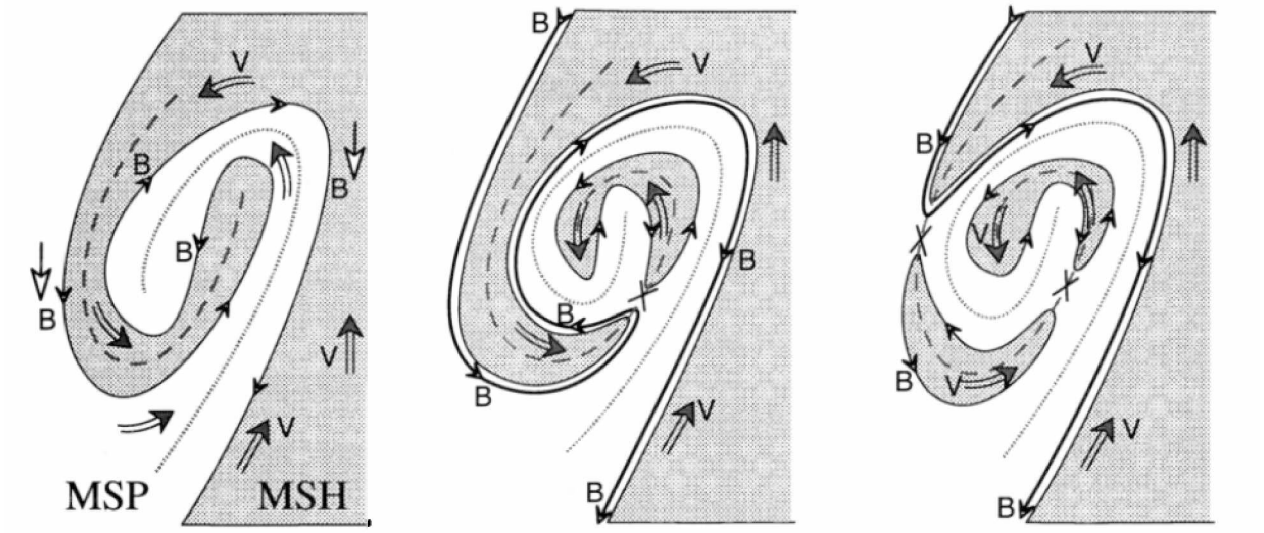

Figure 1.12: Magnetic reconnection in a Kelvin-Helmholtz vortex pinches off blobs of plasma to produce transport (a) *Images reproduced from Otto and Nykyri* (2003).

intermittent reconnection (*Delamere and Bagenal*, 2010). This patchy network of small scale reconnection produces magnetic field which threads the boundary, allowing for cross-magnetopause transport of mass and momentum as labeled in Figure 1.10. Reconnection on the magnetopause boundary driven by KH is illustrated in Figure 1.12. The rolling-up of a vortex forms a thin current sheet (given by the dashed line) which can subsequently reconnect and allow blobs of plasma to be transported across the boundary.

In the first part of Chapter 4, the magnetosheath flows at Saturn are found to be asymmetric in local time due to the cross-magnetopause transport of momentum (*Burkholder et al.*, 2017). However they are also highly variable, as discussed in the second part of Chapter 4 (*Burkholder et al.*, Submitted - 2019). Such variability results from the variability in the solar wind plasma and magnetic field that is driving the Kelvin-Helmholtz. Chapter 4 also discusses mass transport due to kinetic Alfvén wave turbulence, and the diffusion coefficient for this mechanism is derived in Appendix B.

The Cassini spacecraft orbited Saturn for 10+ years before crashing spectacularly into the planet. During this mission thousands of magnetopause boundary crossings allow for many different investigations into the nature of the viscous interaction occurring on this boundary. Some evidence for Kelvin-Helmholtz waves and their distribution with respect to local time is given in Figure 1.11 (*Ma et al.*, 2015). In the dusk sector, the preference for negative angles during outward crossings and positive angles for inward crossings is exactly as expected for large wavelength KH waves being swept tailward across the spacecraft. Pre-noon, the large growth rate for KH waves means that boundary normals are well distributed around zero. In the dawn sector many vortices often roll up quickly to produce a well-mixed boundary layer. The second part of Chapter 4 focuses on finding active KH vortices and their occurrence rate near Saturn's magnetopause.

Simulation results also can resolve the presence of Kelvin-Helmholtz waves on Saturn's magnetopause. Appendix C is included as a follow-on to the first part of Chapter 4, showing hybrid simulation results which quantitatively verify the data analysis. In addition, the Lyon-Fedder-Mobarry global magnetosphere model very nicely produces Kelvin-Helmholtz waves for a range of IMF directions as shown in Figure 1.13 (*Zhang et al.*, 2018). The panels give three different directions for the IMF during the simulation showing that the waves are a robust feature of the model. Since the magnetopause is unstable to the growth of these waves for different IMF directions a variable solar wind direction does not inhibit the instability but will complicate the situation. Solar wind variability in flow velocity, density, and magnetic field strength can, however, determine whether the magnetopause meets the instability criterion for the growth of KH waves.

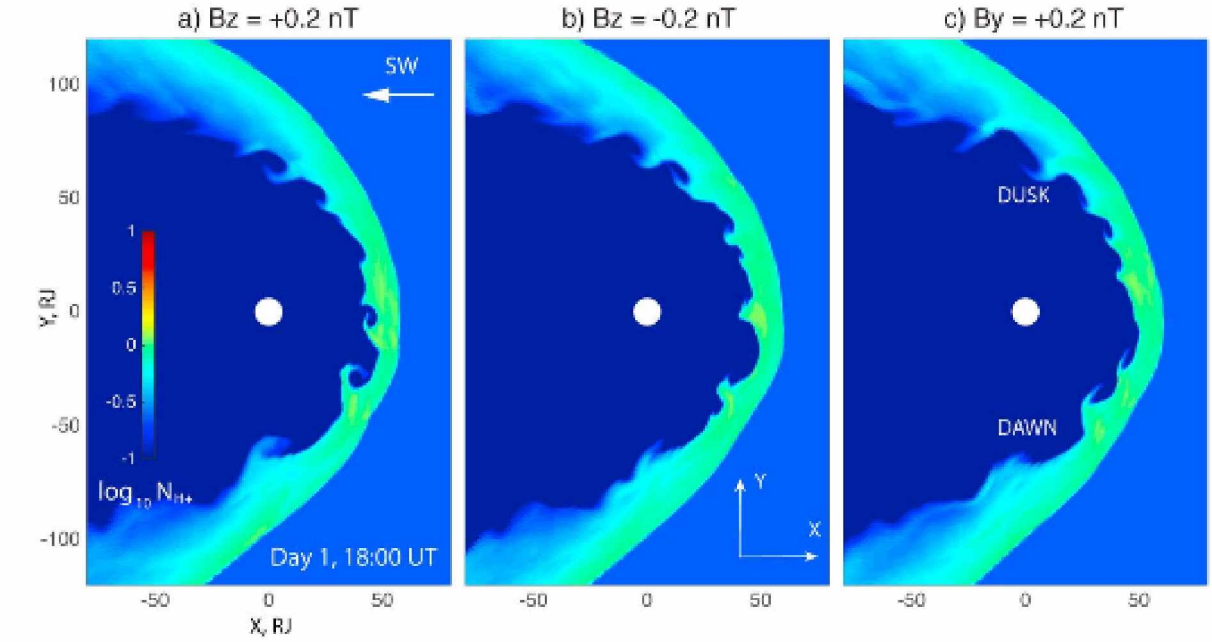

Figure 1.13: Global Saturn magnetosphere simulation for different orientations of interplanetary magnetic field. *Reproduced from Zhang et al.* (2018).

Chapter 2

Magnetic Connectivity in the Corona as a Source of Solar Wind Structure

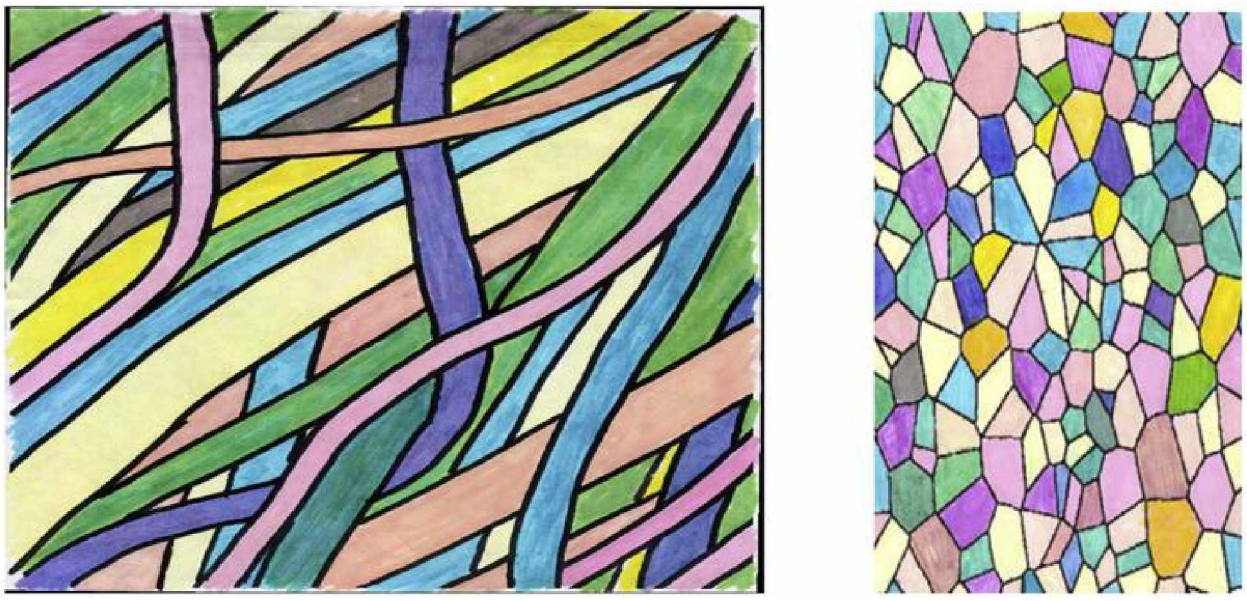

Figure 2.1: Hypothesized spaghetti structure of the solar wind as seen from above the solar system plane and as a satellite immersed in the flow sees it. *Reproduced from Borovsky* (2008).

Abstract[1]

Five decades of satellite data confirm the solar wind contains many boundaries separating flow with distinct magnetic and plasma properties. Some speculate the boundaries in the solar wind found at Earth originate at the solar surface, and are carried along with the expanding solar wind as fossil structures to 1 AU. This begs the question, is it the physics and magnetic structure above the photosphere that creates well defined boundaries between different magnetic flux regions at 1 AU in the solar wind? Magnetic boundaries in the corona exist all the time as topological features of null points in the field. These topological magnetic boundaries seem to be likely locations for plasma boundaries. It can be expected that these boundaries are typical locations where field line-integrated quantities, such as field-aligned current, experience large and abrupt changes. We perform three dimensional resistive magnetohydrodynamic simulations of the solar corona driven by photospheric footpoint motions. We find that large and abrupt changes occur for field line integrated quantities across a magnetic topological boundary and the cause for these changes is the discontinuous mapping for magnetic field lines and thus for Alfvén waves across these boundaries. It is also demonstrated via in-situ properties that thin layers of field-aligned and perpendicular currents are frequently located at or close to topological boundaries.

2.1 Introduction

Solar wind (SW) observations indicate when the flow reaches Earth a spacecraft immersed in it will find many large changes in the magnetic field direction accompanied by jumps in plasma properties. The first definitive evidence came from Pioneer 6 observations (*Bartley et al.*, 1966; *McCracken and Ness*, 1966), just a few years after a brief excursion into the SW by Explorer X provided inconclusive evidence (*Parker*, 1963). A range of statistical analyses and remote sensing data from newer generations of satellites has led to the picture (see *Borovsky* (2008) Figure 1 and *Bruno et al.* (2001) Figure 5) of a highly structured SW with boundaries separating distinct plasma and magnetic fields (*Arnold et al.*, 2013; *Buffington et al.*, 2008; *Mariani et al.*, 1973; *Owens et al.*, 2011; *Thieme et al.*, 1989; *Tu and Marsch*, 1990, 1993; *Viall et al.*, 2009). These authors speculate that the source of SW structure lies near the solar surface, such that flux boundaries are a fossilized remnant of coronal structure.

There are other ideas attempting to explain the origin of SW structure. A discussion of some of these is given in section 8.3 of *Borovsky* (2008) and a short review is found in *Neugebauer and Giacalone* (2010). The most prevalent competing idea posits that turbulence

[1]Manuscript coauthors: A. Otto, P. A. Delamere, J. E. Borovsky

in the SW can generate current sheets in the flow as it traverses interplanetary space to 1 AU, which implies that no preferred scale size would exist. However, estimates by *Borovsky* (2008) indicate that the mean distance between successive boundaries maps to the scale of granules and supergranules on the sun, and further, if the geometry of the boundaries is in the form of "flux tubes", then the amount of magnetic flux contained within a flux tube agrees with individual concentrations of magnetic flux in the solar magnetic carpet. This correlation is compelling evidence that some structure is seeded into the SW as a consequence of processes occurring at the solar surface.

The source for both fast and slow components of SW is the coronal plasma and magnetic field embedded within (*Priest*, 1984). Fast wind emanates from coronal holes along open field while the slow wind is likely linked with coronal streamers (*Zurbuchen*, 2007). The release of fast wind into the heliosphere was originally explained by the *Parker* (1958) thermal expansion model, but modern observations suggest additional acceleration mechanisms are acting as the temperature within coronal holes would give a slow wind speed (*David et al.*, 1997). Further, the *Parker* (1958) model would seemingly suggest that slow wind originates from coronal holes, but the model predicts a steady outflow. This is counter to the observation that slow wind is often better characterized by its variability than the flow speed (*Bame et al.*, 1977), and its composition suggests that it originates from closed coronal field (*Geiss et al.*, 1995).

In the quiet solar corona, looping arcades of the magnetic carpet entrain plasma on closed field lines. In addition, there is everywhere some open flux (*Fisk and Zurbuchen*, 2006) containing the mapped structure and conditions of the underlying photosphere. Some of this open flux is visible in a white light coronograph as the field surrounding the closed arcade within a streamer (*Priest*, 1984). In addition, *Antiochos et al.* (2007) argues that thin corridors of open flux link polar coronal holes to detached coronal holes. The open fraction of the magnetic field can undergo interchange reconnection (*Crooker et al.*, 2002) with closed field when photospheric motions stress the field.

A possible source for structures in the solar wind are the topological features associated with null points in the coronal magnetic field. The magnetic topology associated with a null point contains a fan plane (separatrix layer) in which field lines recede from the null into a two-dimensional planar structure, and a spine, where the field lines converge to a one-dimensional line (see Figure 2.3(a)). The curve that is traced out by the intersection of separatrix surfaces defines a separator field line connecting two nulls. The so-called "topological skeleton" gives a complete description of the field in terms of spines and separatrices (*Priest et al.*, 1997).

The many null points in the solar magnetic field (*Close et al.*, 2004; *Platten et al.*, 2014) separate regions of flux with a myriad of separatrix surfaces. These boundaries are important

since the field line connectivity is discontinuous between neighboring points either side of the separatrix. Three-dimensional null points take on a different character according to the eigenvalues of a matrix constructed from the magnetic field in the neighborhood of the null (*Parnell et al.*, 1996). In the solar magnetic environment, for instance, these eigenvalues would determine whether a separatrix forms a dome which isolates a volume of the magnetic field, or the separatrix is oriented vertically such that it forms a boundary between regions of open flux (*DeRosa and Barnes*, 2018).

Furthermore, *Titov et al.* (2002) defines quasi-separatrix layers (QSL) in terms of the "squashing," which are magnetic structures that define field lines with dissimilar connectivity. For the QSL, the magnetic field line mapping is not discontinuous but varies rapidly. These layers are important for the study of boundary structure in the solar magnetic field since the magnetic separatrix associated with a null point is surrounded by QSLs (*Masson et al.*, 2009). The separatrix layer and QSL can be the location of magnetic reconnection and the change in connectivity can be quite different in the two layers (*Masson et al.*, 2017).

For the general three-dimensional reconnection scenario, it has been proposed using kinematic models that topological features, i.e. null points, separatrices, separators, QSLs, and spine field lines, all play an important role in determining the location of current build up and reconnection sites (*Démoulin et al.*, 1996b; *Parnell et al.*, 2010; *Pontin et al.*, 2004, 2005; *Priest and Démoulin*, 1995; *Priest and Pontin*, 2009). Resistive MHD simulations by *Pontin et al.* (2007) suggest that the kinematic model can capture some important aspects of the topological response to a general perturbation.

The propagation of waves near magnetic topological features is non-trivial due to the dependence of the fast mode and shear Alfvén velocities on the local magnetic field strength. A review of magnetohydrodynamic (MHD) wave behavior near a coronal null is provided by *McLaughlin et al.* (2011). An important feature of the coronal magnetic environment is that many separatrix surfaces interact, giving rise to a complicated topology with many separators and QSLs. Alfvén wave propagation in this context is highly influenced by the magnetic topology.

Shear Alfvén waves, with wave vector $\mathbf{k}$ parallel or anti-parallel to the magnetic field (*Alfvén*, 1942), are a fundamental wave mode for the study of plasma physics. For the coronal field, the convective motion and magnetic field at the photosphere represents a non-uniform source and reflective boundary for Alfvén waves. These waves carry Poynting flux away and toward the photosphere. Alfvén waves launched from all over the photospheric surface interact in accordance with the field line connectivity (determined by the topological skeleton). The resulting distribution of currents has many intense concentrations which lie somewhere along or near the separatrix surfaces of the skeleton. This behavior has been

studied in a solar context in simplified configurations (*Edmondson et al.*, 2010; *Pontin et al.*, 2013; *Santos et al.*, 2011), motivating our investigation of complex fields where separatrix surfaces interact. *Candelaresi et al.* (2016) found that a complicated field topology can affect the propagation of energy and concluded that it is difficult for footpoint motions to propagate a disturbance high into the corona because energy is efficiently trapped near low-lying topological features.

Many numerical investigations of the slow SW structure and origin have been conducted (*Edmondson et al.*, 2009; *Higginson et al.*, 2017a,b; *Higginson and Lynch*, 2018; *Linker et al.*, 2011), although these do not resolve the SW scale sizes in question. The results presented here show field line integrated plasma and magnetic field properties for a rectangular volume of the coronal and photospheric magnetic field. The field line integration provides an easy means to identify boundary features and their relation to magnetic topology. Another important aspect of the simulation is that all the flux which penetrates the top boundary of the simulation can be considered "open" (extending to infinity) although some may still be technically part of the closed "arcade." Integrating along the open portion of flux resolves boundary structure determined by the magnetic topology, and these boundaries can effectively be identified as "flux tube boundaries" separating regions of open coronal field.

The remainder of this paper is organized as follows. Section 2 gives a description of the model. Section 3 provides a brief review of the Alfvénic current system and the concentration of electric current near magnetic topological features. Section 4 presents the results of non-local field line integral properties close to the photosphere and at the open top boundary in the simulation. Section 5 shows the imprint of topology from an in-situ picture which is compared with the integral properties and the effect of reconnection is considered. The conclusions provide a brief summary of results.

2.2 Simulation Model

2.2.1 Numerical Methods

The numerical model employs a finite difference approximation of the normalized resistive MHD equations [e.g., *Adamson et al.,* 2013]:

$$\frac{\partial \rho}{\partial t} = -\nabla \cdot \rho \mathbf{u}$$

$$\frac{\partial \rho \mathbf{u}}{\partial t} = -\nabla \cdot \rho \mathbf{u}\mathbf{u} - \nabla h^{\gamma} + \mathbf{j} \times \mathbf{B} - \nu \rho (\mathbf{u} - \mathbf{u}_0)$$

$$\frac{\partial h}{\partial t} = -\nabla \cdot (h\mathbf{u}) + \frac{(\gamma - 1)}{\gamma h^{\gamma - 1}} \eta \mathbf{j}^2$$

$$\frac{\partial \mathbf{B}}{\partial t} = \nabla \times (\mathbf{u} \times \mathbf{B} - \eta \mathbf{j}),$$

where $\mathbf{B}$ is the vector magnetic field, $\mathbf{u}$ is the vector plasma flow velocity, ρ is the single fluid mass density, η is the resistivity, thermal pressure p determines $h = (p/2)^{1/\gamma}$, (a volumetric entropy measure that only changes through net in- or outflow into any fixed volume or through nonadiabatic effects), and $\mathbf{j} = \nabla \times \mathbf{B}$ is the current density. The polytropic index is $\gamma = \frac{5}{3}$, the parameter ν is a height dependent constant such that the neutral motion at the photosphere only couples to the plasma over the first few grid cells (in the chromosphere), and the horizontal flow profile $\mathbf{u}_0(x, y, t)$ represents the imposed pattern of footpoint motion at the photospheric boundary. The force of gravity is neglected from the momentum equation since the main effect of the sharp transition in density and temperature occuring above the chromosphere can be considered without taking gravity into account (see initial conditions below). Gravity is important in a self consistent model of the chromosphere and the transition layer, or if the physics is highly sensitive to the details of the density and pressure profile in the corona. This is not the goal in this paper.

The dimensionless variables in the above equations have been normalized to characteristic values. A typical length scale is $L_0 = 500$ km, the normalizing number density is $\mathrm{n}_0 = 2 \times 10^{15}$ m^{-3} with mass density $\rho_0 = n_0 m_{proton}$, and the normalizing magnetic field strength is $B_0 = 10^{-4}$ T. The explicit density and magnetic field profiles for the initial equilibrium are presented in section 2.2. With these choices velocity is normalized to the Alfvén speed $u_{A0} = \frac{B_0}{\sqrt{\mu_0 \rho_0}} \approx 50$ km/s. The thermal pressure is normalized to the magnetic pressure $p_0 = \frac{B_0^2}{2\mu_0} \approx 4 \times 10^{-3}$ Pa. This choice implies a plasma β_0 of 1 for the chosen B_0 and $\beta << 1$ in regions of stronger magnetic field where B can be as large as $40 B_0$. The normalization for time is the Alfvén crossing time, $\frac{L_0}{u_{A0}} \approx 10$ s, and the normalizing resistivity is $\eta_0 = \mu_0 L_0 u_{A0} \approx 3 \times 10^4$ Ωm.

The MHD equations are solved using a Leapfrog/Dufort-Frankel scheme on a Cartesian grid of $253 \times 253 \times 153$ points which encloses a volume of $47 \times 47 \times 31$ Mm in the chosen normalization. The grid is uniform in the x and y directions and stretched in the vertical z direction. The resolution along z maximizes at the bottom boundary, remains highly resolved through the transition region, then decreases with height. The grid spacing in the x and y directions is $\Delta x = \Delta y = 0.37 = 185$ km, while in the z direction its smallest spacing is $\Delta z = 0.30 = 150$ km and largest is $\Delta z = 0.72 = 360$ km. Note, that this grid scale is appropriate to resolve and cover lengths from typical granular to supergranular scales. Other key aspects of the numerics of the simulation are described in *Otto et al.* (2007) and *Adamson et al.* (2013).

2.2.2 Initial and Boundary Conditions

The three-dimensional magnetic field is initialized as a linear force free extrapolation of a two-dimensional magnetic polarity distribution at the photospheric surface. The extrapolation is calculated following the approach suggested by *Otto et al.* (2007), which is a linear spectral method similar to *Seehafer* (1978) but suitable for MHD simulations. The specific boundary conditions are presented at the end of this section. We represent the polarity distribution at the photospheric surface as a superposition of Fourier modes. For the presented simulation results, the smallest wavelengths that contribute are determined not by the x, y grid resolution but by the smallest value of Δz in order to resolve the small scale height for the largest mode numbers in the expansion.

In the forthcoming sections, we use the magnetic configuration given by an observed magnetic polarity distribution at the photospheric boundary as in *Adamson et al.* (2013). However, the construction of synthetic magnetograms can also provide insight as we are concerned with the propagation of waves in a complicated field topology, and the coronal field can be assumed to take on any conceivable force free state in its evolution. A visualization of the magnetic field configuration used for the majority of the discussion to follow is shown in Figure 2.2. Although all of the results which follow use the field shown in Figure 2.2, we have examined numerous different choices for the magnetic field with qualitatively the same results as will be presented.

The flow pattern is approximated as a combination of divergence-free (i.e., incompressible flow) vortices each in the form

$$\mathbf{u}_n(x,y,t) = \nabla \times \left[\frac{\phi_n}{\cosh(\frac{x-y+c_n}{l_n})\cosh(\frac{x+y+d_n}{k_n})}\right]\hat{\mathbf{z}}$$

so that $\mathbf{u_0} = \sum \mathbf{u}_n$. Example values for the constants c_n, d_n and l_n, k_n, which adjust the position and shape of each vortex, are given in Table 2.1. The magnitude of the driving is given by the parameter ϕ_n. Case 1, which is shown by the flow vectors on the photosphere surface of Figure 2.2, is used for an in-depth analysis and case 2 is used for a quick comparison in section 4.3. The perturbation is such that the magnitude of the chosen photospheric

Table 2.1: Coefficients for velocity perturbation. The number of coefficients in brackets indicates the number of perturbation vortices.

	c_n	d_n	l_n	k_n	ϕ_n
case 1	[-18,10,38]	[-102,-56,-76]	[-12,-12,-14]	[12,12,14]	[1.6,0.64,0.88]
case 2	[-10,-35]	[-122,-80]	[-12,-12]	[12,12]	[1.6,1.6]
Adamson et al. (2013)	[-18,10,38]	[-102,-56,-76]	[-12,-12,-14]	[12,12,14]	[0.1,0.04,0.11]

velocity is by a factor of ~ 10 greater than inferred from photospheric observations. This results in faster generation of currents and other signatures associated with the magnetic field configuration. This is justified because the resulting evolution is virtually identical as long as the photospheric velocity perturbation is small compared to the corresponding Alfvén speed such that the Alfvénic perturbations remain linear.

An important feature of the field extrapolation is that total magnetic flux decreases as a function of z, since the scale height decreases with increasing mode number. This dependence determines the scale size to which open flux maps at the photosphere. With no average field in the z direction, the net flux penetrating the top boundary is zero, but we can superpose a vertical component of the field in order to model a region of the sun where the net open flux is nonzero. Superposing an average field changes the photospheric footpoint area of open flux on the photosphere, which changes the scale size of structure on open flux. We restrict our investigation to open flux that is representative of the solar corona, where on the large scale the net open flux must be zero but in local regions may be slightly imbalanced.

An initial condition with $< 5\%$ net flux as a fraction of the total photospheric flux is required. As a result, all the magnetic flux penetrating the top boundary maps to $< 10\%$ of the photospheric area. The last column of Table 2.2 gives the side length of a square containing the total area of open flux on the photosphere as the average z component of the magnetic field is varied. Given the observed upper limit for granule diameters of 1800 km (*Schwarzschild*, 1959), the table indicates that just a few granules corresponds well to a typical length scale for the open flux footpoint on the photosphere.

Table 2.2: Footpoint area at the photosphere as the percentage of net open flux is varied. The percentage net open flux is calculated as a fraction of the total photospheric flux. The bold value of net open flux is used for simulations presented in this paper. The last column gives a size for the footpoint of open flux at the photosphere if it were all contained in a single square.

total photosphere flux ($\times 10^4\ B_0 \cdot L_0^2$)	superposed B_z	net open flux	photosphere area	square footpoint size (Mm)
3.37	-0.21	-5.5%	1.6%	5.9
3.38	-0.09	-2.4%	0.8%	4.2
3.39	**-0.03**	**-0.8%**	**1.2%**	**5.1**
3.40	0	0%	1.6%	5.9
3.42	0.16	3.9%	5.7%	11.2
3.43	0.19	4.8%	7.1%	12.5

The bold value in Table 2.2 gives characteristics of the open flux footpoint for cases 1 and 2. Although values in this table are dependent on the Fourier coefficients used to

construct the field, the trend in photospheric open flux area is similar for any inputs to the extrapolation procedure.

The state of the plasma chosen as an initial condition mimics the corona and chromospheric transition region. Pressure is initialized as constant throughout, however, the density has a z dependence of

$$\rho(z) = \frac{\rho_{chr}}{2}(1 - \tanh(2(z - z_0))) + \rho_{cor}$$

where the subscripts *chr* and *cor* are for chromosphere and corona, respectively. Here $n_{cor} = 0.072$ and $n_{chr} = 10$ in normalized units giving physical number densities $n_{cor} = 1.44 \times 10^{14}$ m^{-3} and $n_{chr} = 2.0 \times 10^{16}$ m^{-3}. This accounts for a reasonably realistic large change of Alfvén speed in the solar transition region. The width of this transition at $z_0 = 1.5$ is $\sim 2L_0$. Via the single fluid ideal gas law $p = 2nk_BT$, the temperature must increase by $\sim$2 orders of magnitude through the transition region to maintain pressure balance. The plasma is qualitatively similar to conditions on the sun with a dense, cold chromospheric plasma underlying a hot, rarefied coronal plasma. The transition region plays an important role as it is naturally the location where large gradients develop. The strong density change and the large magnetic field gradients close to the photosphere motivate the specific vertical grid stretching, which maintains high resolution through the transition region.

The choice of boundary conditions for the $x - z$ and $y - z$ planes reflects the symmetry properties of the set of MHD equations consistent with the chosen magnetic field extrapolation. These boundary conditions, described in *Otto et al.* (2007), employ a mirror symmetry across the lines drawn vertically at the locations ($[0, L_x/2]$, $[0, L_y/2]$, $[L_x/2, L_y]$, $[L_x, L_y/2]$), where L_x, L_y are the horizontal dimensions of the simulation. The mirror symmetry means for any $d < L_x/2$ and $e < L_y/2$ the point at $[L_x/2 + d, e]$ will have field quantities reversed in the y direction but equal in the x direction compared to the point at $[L_x/2 - d, -e]$. Equivalently, for $d < L_y/2$ and $e < L_x/2$, x direction components are reversed for a point at $[e, L_y/2 + d]$ compared to at $[-e, L_y/2 - d]$, while the y direction is preserved.

At the top and bottom boundaries, we employ a Neumann boundary condition so there is no gradient normal to the system boundary $\frac{\partial f}{\partial n} = 0$ for the quantities $f = [\rho, h, u_x, u_y]$. The u_z component of velocity at the bottom boundary is set to zero and is a Neumann boundary at the top. At the top boundary, horizontal components of the magnetic field are calculated as a Neumann boundary and at the bottom boundary they satisfy the force-free condition $\nabla \times \mathbf{B} = \alpha \mathbf{B}$. The B_z component of magnetic field at the top and bottom boundaries is chosen so that the divergence free condition $\nabla \cdot \mathbf{B} = 0$ is satisfied.

The simulation volume and associated scale size can be further visualized with the help of Figure 6.3 of *Priest* (1984), where the supergranular convection cells are larger than any individual polarity concentration.

2.3 Alfvén Waves and Magnetic Topology

Photospheric motions acting on the magnetic field continuously launch shear Alfvén waves into the corona. Any localized wavetrain is bound by field-aligned currents given by the curl of the perturbation magnetic field. Across a strong magnetic gradient or strong shear of the photospheric velocity, an Alfvén wave drives significant field-aligned currents. Along with the field-aligned current, a constant amplitude Alfvén wave also carries a closing current perpendicular to the magnetic field at its leading edge in the form of a polarization current.

In addition to local inhomogeneities in the magnetic field and in the photospheric convection, Alfvén waves are expected to generate strong field-aligned currents at or close to separatrix surfaces. *Priest and Pontin* (2009) have proposed the generation of a field-aligned current associated with magnetic null points and the corresponding spine and fan topology. For specific magnetic field geometries and velocity boundary conditions, it has been demonstrated that a strong current can be generated close to the null point and along the separatrix surface (*Galsgaard et al.*, 1997; *Pontin et al.*, 2007). Similarly, studies of wave propagation (*McLaughlin et al.*, 2011) indicate that magnetic nulls and topological boundaries are preferential locations for heating and current sheet formation.

Linear Alfvén waves propagate along magnetic field lines. Since the mapping of the magnetic field is discontinuous at separatrix surfaces, it has to be expected that Alfvénic perturbations of the magnetic field are different across a separatrix surface and in the vicinity of a spine because they originate from very different regions on the sun. Therefore topological elements such as separatrix surfaces and spines should be natural locations of strong field-aligned currents. While quasi-separatrix layers do not have a discontinuous mapping, the magnetic field line connectivity changes strongly, such that similar current sheets can be expected (*Démoulin et al.*, 1996a). Indeed, current accumulation at QSLs has been demonstrated in MHD simulations (*Aulanier, G. et al.*, 2005; *Effenberger et al.*, 2011; *De Moortel, I. and Galsgaard, K.*, 2006) and observations (*Janvier et al.*, 2014).

Figure 2.3 illustrates the magnetic field connectivity of the fan and spine for a typical coronal null point. Panel (a) shows many field lines which map near a spine having both ends on the photosphere. Field lines approaching the null from near the fan plane will either map in the vicinity of the spine to the yellow region or in the opposing direction to the blue region. This different origin is used for the color of each field line. In general blue and yellow regions

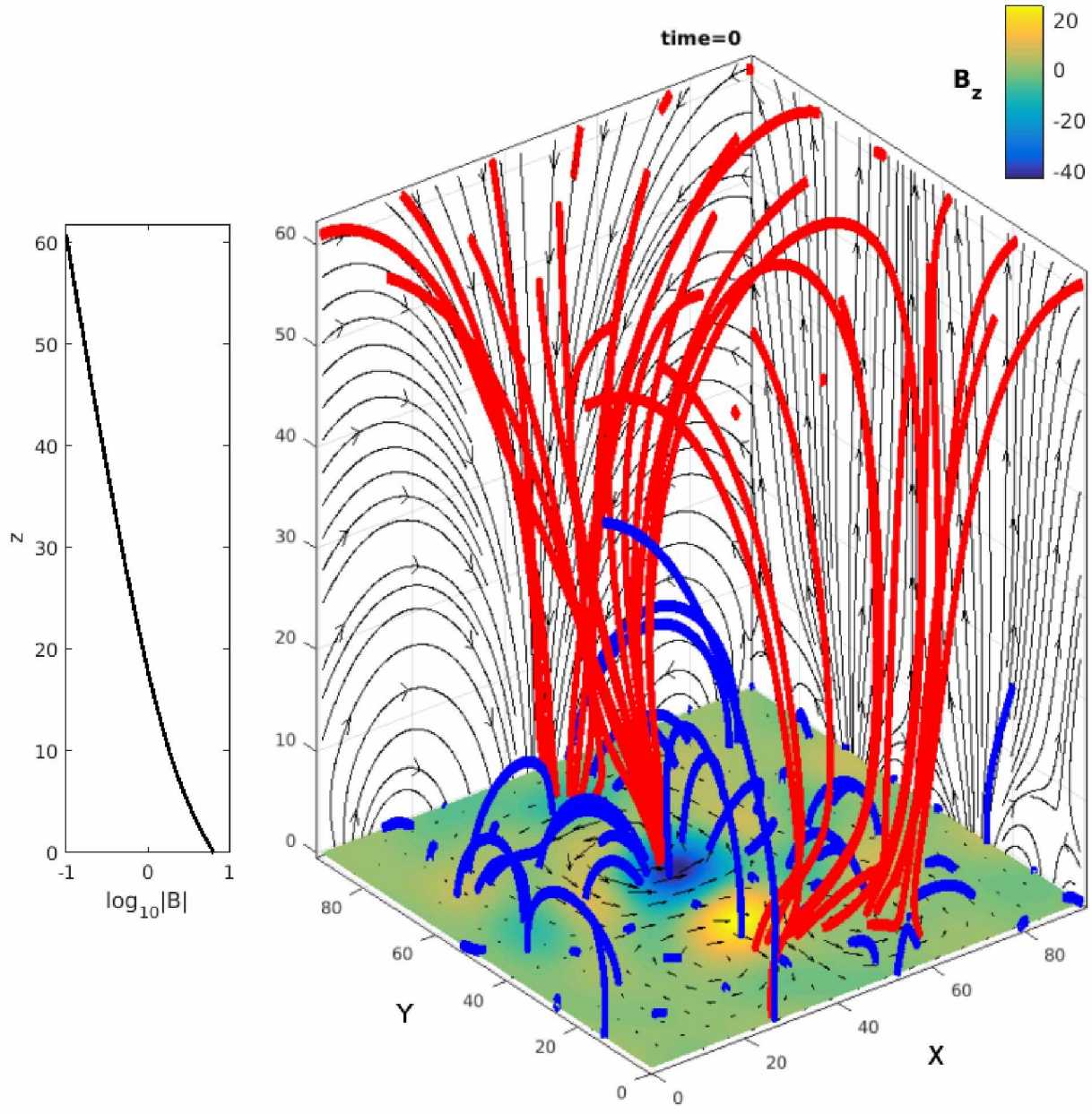

Figure 2.2: Blue field lines are integrated from the bottom boundary and red are integrated from the top. The colormap gives B_z at the photosphere, and flow vectors on the photospheric surface represent the convective motion (case 1). Streamlines on the vertical boundary planes are a magnetic field projection. The dependence of field strength averaged over a horizontal plane at a given height in the simulation appears to the left.

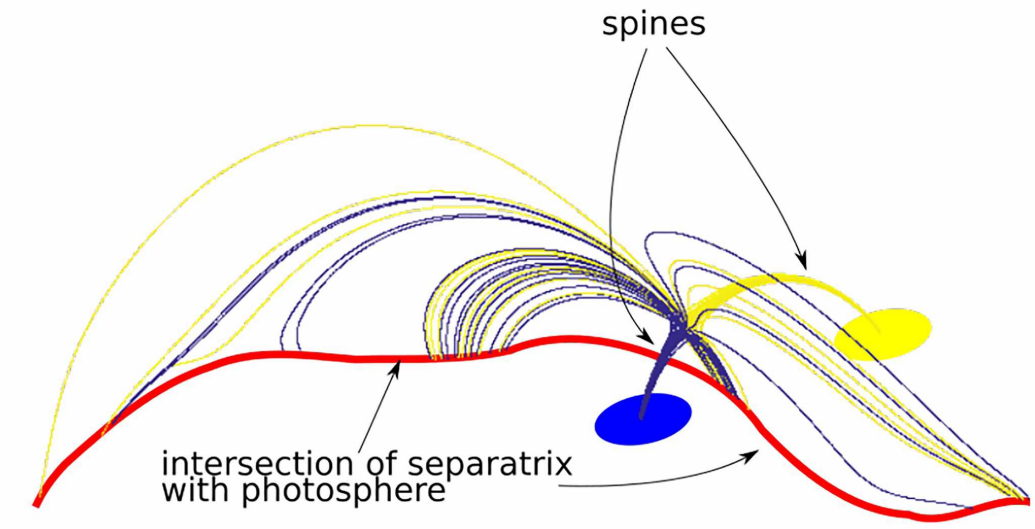

(a)

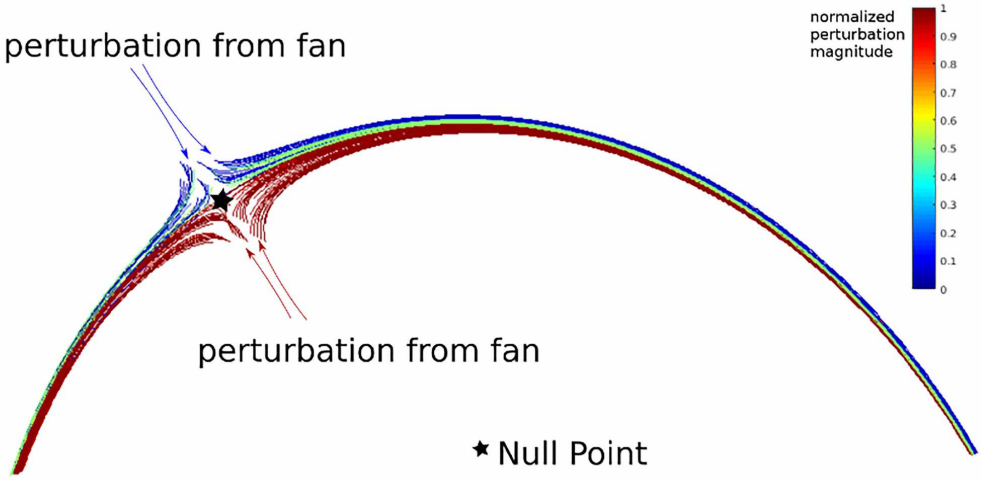

(b)

Figure 2.3: In (a) the color gives spine footpoint location for a set of field lines which map near the separatrix layer. The red curve marks the intersection of the separatrix with the photosphere. In (b) the color of a set of field lines near the spine is given by the velocity perturbation at each corresponding fan footpoint with a colorbar normalized to the highest value.

have different magnetic field values and velocity perturbations. In Panel (b), a number of field lines surrounding the spine are shown with the fan topology hidden. The color gives the magnitude of the velocity perturbation that is driven from the location where the fan field lines connect to the photosphere. This shows a mixture of different perturbations converging to a region surrounding the spine.

Panel (a) shows that field lines which neighbor one another in the fan plane may connect along different directions to opposite spine locations. The initial magnetic field is, however, smooth and continuous, so changes in the configuration are important for the existence of a magnetic topological imprint. Generally, photospheric motion and magnetic field are different in the two spine locations such that different amplitude and polarization Alfvén waves are being carried into the same neighborhood at the fan plane. Panel (b) shows that the perturbation is discontinuous between neighboring field lines mapping near the spine due to the complicated mapping of separatrix field lines. From Figure 2.3, we conclude that the fan plane and spine of null points in the corona will be highly conducive to the formation of discontinuities. These arguments apply particularly when Alfvén waves bounce repeatedly along magnetic field lines, since different origins and bounce times contribute to different magnetic and velocity perturbations.

2.4 Field Line Integrated Boundaries

For 1001×1001 initial coordinates we first integrate from a footpoint at the photosphere to a terminating footpoint at either the photosphere or the top boundary of the simulation. It will be shown how this procedure provides a means to identify where separatrices exist in the field. To determine open magnetic flux properties, magnetic field line content is also integrated from the top boundary along all the open flux in the system.

The integration procedure provides a non-local description of the magnetic field throughout the whole simulation volume. Bundles of flux which share the same characteristics are easily distinguishable when separated by a discontinuity. Where strong gradients appear in field line integrated quantities it is likely that a boundary surface is present. The picture that emerges from the field line integration has many different regions of flux separated by boundaries mostly coincident with the topological boundaries in the field.

The strength of individual perturbations and therefore also the gradients depend on a number of parameters. Clearly the magnitude of the photospheric velocity and magnetic field have an influence. Velocity and magnetic field determine the magnetic perturbation and Poynting flux. The length of a field line must also have an influence as well as the manner in which the strength of the magnetic field changes in traversing from one footpoint

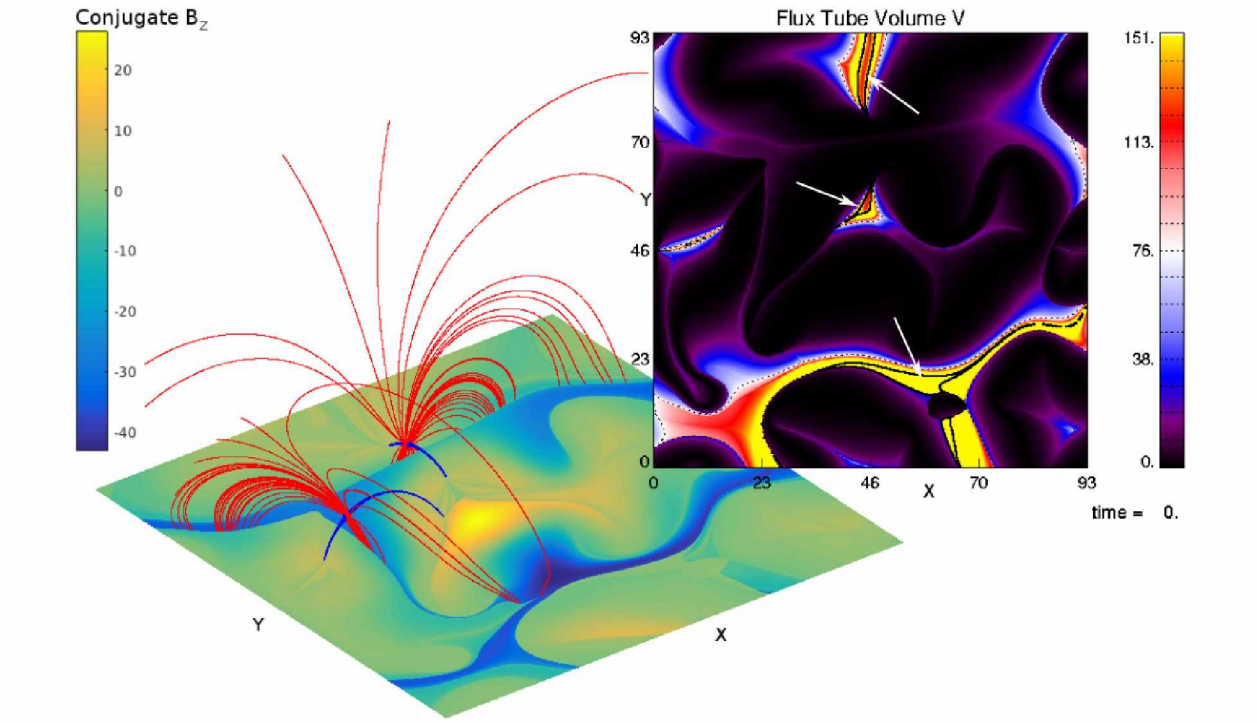

Figure 2.4: The colormap on the photosphere shows the vertical magnetic field value at the conjugate footpoint. A discontinuous change of the conjugate magnetic field indicates a change of magnetic connection or topology. Some of the magnetic topology is given by the red colored field lines which characterize the fan plane of two distinct nulls. The color of these field lines is changed to blue when they converge towards the spine. The flux tube volume (FTV), shown in the inset, has thin features which map to magnetic topological features, i.e. regions where the connectivity varies. In the inset above and other figures below, the solid contours outline open flux (highlighted by white arrows in this figure) and the dashed contours correspond to the middle value for the colorbar.

of a field line to the other. Waves that travel along field lines which pass very close to a null point steepen significantly in magnetic perturbation. These parameters determine the properties of the respective field-integrated quantities and therefore the magnitude of gradients across separatrix surfaces.

2.4.1 Integration from Photosphere

A field line integration beginning from the photospheric boundary represents mostly closed flux. The highly dynamic nature of the solar magnetic environment can produce and rearrange structure over many temporal and spatial scales, connecting the structure on closed field to that on open field. For example, the rising of field due to the input of Poynting flux, the emergence of flux from beneath the photosphere, and magnetic reconnection between open and closed field, all play a role in sourcing the magnetic field and plasma that is

accelerated to become the supersonic SW.

For the identification of topological features in the simulation magnetic field, the flux tube volume (FTV) is computed from the integral $\int \frac{ds}{|B|}$ along a field line. The use of FTV to identify topology can be compared and contrasted with other methods such as the so-called squashing factor (*Titov et al.*, 2002) or the N-norm (*Démoulin et al.*, 1996b). The different methods used to find topological features show quantitatively and sometimes qualitatively different results. To best avoid this ambiguity, we use a combination of integral and non-local quantities supplemented by actual null point identification rather than to depend on a single metric. For the sake of brevity, we omit here the flux tube mass, flux tube entropy, field line length, integrated magnetic energy, and conjugate footpoint coordinates. These quantites, among others, each can provide a diagnostic of some portion of the topology in the field.

Figure 2.4 shows a carefully selected set of field lines from the simulation which are the spine and fan of two null points. The inset of Figure 2.4 shows the integration of FTV for the initial conditions. The colorplot on the photosphere surface of Figure 2.4 is the vertical field value B_z at the conjugate footpoint. Note that a discontinuous change of the vertical magnetic field at the conjugate magnetic footpoint is a strong indicator for a topological boundary because B_z is continuous and smooth in the simulation.

From the definition of flux tube volume, a field line with infinite FTV maps to a null point where $|B| = 0$. A field line with large FTV either maps to the vicinity of a null point or reaches a high altitude in the simulation. A field line near the spine or fan of a null point has large FTV because it will approach the null where the field magnitude is going to zero. The same can be expected for any field lines where the connectivity strongly diverges since this is associated with small magnetic field strength. Field lines which map to large heights above the photosphere have a large FTV because of the decrease in magnetic flux with height in the extrapolation. The FTV (Figure 2.4 inset) is therefore suited to identify separatrix surfaces, but in addition identifies the boundary between open and closed flux.

In Figure 2.4, the inset colormap of FTV shows a thin web of features which agree with the mapping of red separatrix field lines intersecting the photosphere. The width of some of these surfaces is so thin that they are not all resolved with the chosen grid for field line integration. This is not surprising, as any finite resolution is insufficient to capture a discontinuous topological boundary. A comparison with the conjugate footpoint polarity, shown in Figure 2.4 as the photospheric surface, demonstrates that the separatrix/photosphere intersection curves coincide with strong gradients in the conjugate footpoint polarity. This confirms that the FTV can indeed identify topological boundaries. The comparison of conjugate footpoint B_z with FTV helps to render apparent the difference between high altitude loops (open flux enclosed by the black contour in FTV) and magnetic topological features in the FTV.

Figure 2.5 is the integrated FTV and field-aligned current after photospheric motions have acted on the field. The effect on the topology of the field is demonstrated by comparing Figure 2.5(a) with the FTV given at the beginning of the simulation in Figure 2.4. The footpoint motion shifts and distorts separatrix boundaries, but the velocity perturbation is continuous so this alone can not alter the topology.

Magnetic reconnection can have an effect on the topology, and a measure of the reconnection rate in three dimensions is the integrated parallel electric field $E_{||}$ (*Hesse and Schindler*, 1988; *Schindler et al.*, 1988). Since $E_{||}$ is proportional to the field-aligned current density through $\mathbf{E} = \frac{1}{\eta}\mathbf{J}$, the integrated field-aligned current, shown in Figure 2.5(b), is a measure of where reconnection can operate. Concentrations of current paint the topological features which can be identified in Figure 2.5(a). The width of a typical current concentration is of the order 10 grid cells, which is 1-2 Mm for the given normalization but can be significantly smaller at some boundaries. Reconnection acts on the boundaries between regions of flux, but the evolution indicates that separatrices remain almost entirely intact.

The pattern of integrated current directed perpendicular to the local field, shown in Figure 2.6(a), is also dependent on the topology. Concentrations of integrated perpendicular current occur along similar sets of field lines to those of the integrated parallel current and often where the polarity of the field-aligned current changes. A distinction is that the perpendicular currents tend to appear in thinner features along separatrix surfaces than the width of the parallel current gradients. The width of integrated perpendicular currents is frequently fewer than five integrations cells, around half a Mm. Sometimes the signature is so thin that the chosen resolution for the integration grid is insufficient to fully resolve the integrated perpendicular current.

In Figure 2.6(b), the integration labels footpoints by the difference in maximum and minimum pressure found along a field line. Pressure variation along a field line indicates that the system deviates from an exact equilibrium where pressure must be constant along magnetic field lines. This quantity exhibits discontinuous jumps at some of the topological features, so that plasma which is being driven away from equilibrium stays separated from unperturbed plasma. The notable feature of this quantity is that although strong gradients characterize the separatrix boundaries, these gradients are broader than the corresponding widths for current layers.

Further, the kinetic energy of the plasma is integrated to determine its relation to the topology. Figures 2.6(c) and 2.6(d) show the initial and final distribution of integrated kinetic energy, respectively. Since the velocity perturbation for this case is constant in time, it is important to be able to determine which portions of Figure 2.6(d) evolved as a consequence of the dynamics rather than being a signature of the prescribed energy source. In Figure

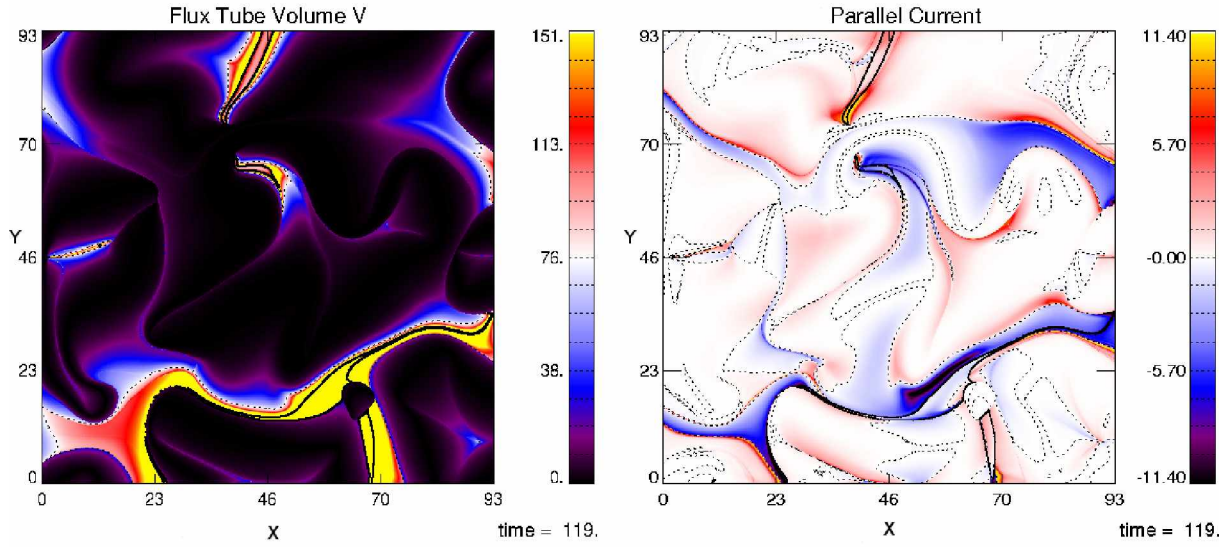

(a) (b)

Figure 2.5: FTV (a) and integral field-aligned current (b) 119 Alfvén times (∼20 minutes) after photospheric convection (case 1) has been switched on. The integration along field lines is started from the bottom (photospheric) boundary. The initial configuration of the FTV shown in Figure 2.4 evolves to panel (a) of this figure.

2.6(d), kinetic energy is apt to develop on field lines near the separatrix surfaces. In addition, a number of separatrix boundaries have large integrated kinetic energy on one side and small integrated kinetic energy on the opposing side, with a tendency for the gradients to be broader than the width of the current layers. This would suggest the topological boundaries are acting as physical boundaries to the plasma.

Note that although the field-aligned pressure gradients and integrated kinetic energy demonstrate a deviation from an exact equilibrium, the resulting changes in the overall configuration are slow. Simulations with the same magnetic field but smaller amplitude photospheric convection demonstrate the same evolution only correspondingly slower, which is consistent with a so-called quasi-static evolution, i.e., an evolution of a sequence of equilibrium configurations.

2.4.2 Integration on Open Flux

Small mode numbers in the magnetic field extrapolation are responsible for flux in the system which reaches a large altitude. Some of this flux pierces the top boundary of the simulation, and we define it as open. This is in the spirit of the Potential Field Source Surface (PFSS) model developed by *Schatten et al.* (1969) and *Altschuler and Newkirk* (1969). To support

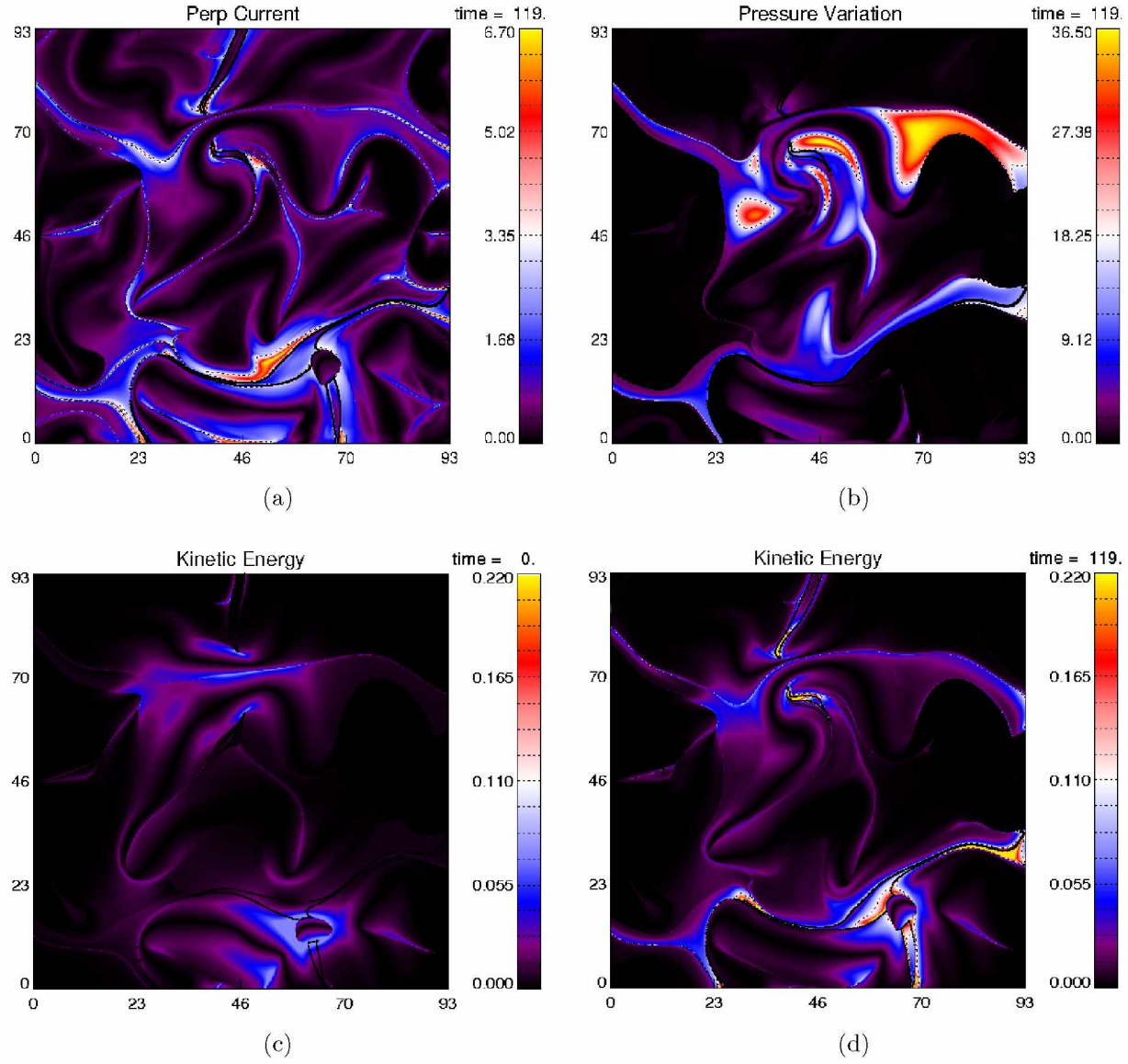

Figure 2.6: Field line integrated current perpendicular to the magnetic field (a), maximum thermal pressure difference along the magnetic field line (b), and field line integrated kinetic energy (c) and (d). Integration is started from the photosphere and all plots show the respective quantities at t = 119 Alfvén times, except for (c) which shows the kinetic energy when photospheric convection (case 1) is turned on at t = 0.

the conclusions of this paper, simulations were performed in which the height of the simulation volume was either increased or decreased by 50%, which causes very little change to the photospheric footpoint area of open flux. These small changes are expected since the simulation box is always large enough that unbalanced field dominates at the top. This is the main difference between our model and the PFSS model, which gives a structure of open flux that is dependent on the simulation height and has a purely radial field at the top boundary. The results of driving the field for the different sized numerical boxes, not shown here, were in qualitative agreement with the results given below.

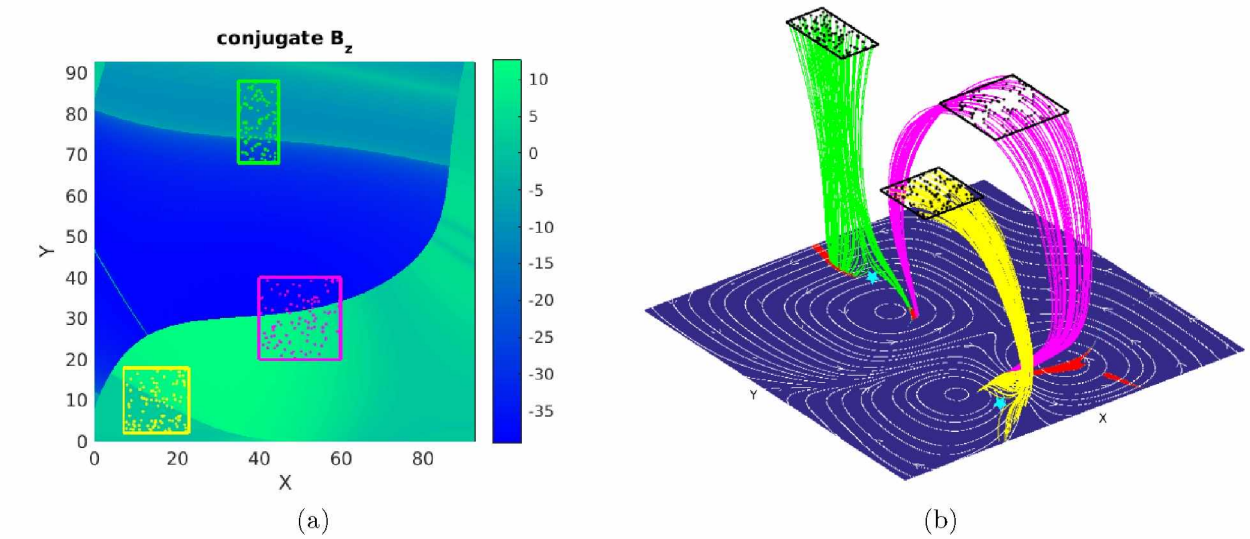

(a) (b)

Figure 2.7: In panel (a), the colormap shows conjugate footpoint B_z at t = 0 for field lines penetrating the top boundary. The boxes with colored dots represent starting points at the top plane for field lines shown in panel (b), which are color coded according to the dots in panel (a). All shown field lines terminate in the red regions representing photospheric open flux. The green and yellow field lines are intersected by a separatrix surface, as can be seen by the diverging connectivity near the photosphere surface which happens in the vicinity of the cyan stars. These stars label the approximate location of a null point. The magenta field lines highlight a different feature that is not indicative of a separatrix and will not be expected to be associated with a large current density once the field is evolved. The streamlines in panel (b) give the direction of convection at the photosphere but not the magnitude.

Integrating from the top boundary means that each conjugate footpoint lies on the photosphere. Since the total flux decreases with height, the area of open flux on a given horizontal plane expands with altitude, and becomes volume filling at the top of the corona. The number of field lines traced from the top boundary is the same as the number traced from the bottom boundary, so we have higher resolution in terms of field lines per unit magnetic flux in this section compared to the previous. As quantified in Table 2.2, structure on open flux

is indicative of granular scales on the photospheric surface.

In order to determine the location of topology on open field, Figure 2.7 shows the conjugate footpoint B_z in panel (a) alongside a set of colored field lines in panel (b). The discontinuities in panel (a) separate field lines which map to different parts of the photosphere, but they are not all necessarily separatrix surfaces. Some examples of separatrices intersect the regions of green and yellow points. From panel (b), the mapping of the green and yellow field lines approaches the cyan stars, which are locations for null points, so indeed these large gradients in panel (a) are separatrices. Other features in the conjugate B_z are a consequence of the finite height of the simulation box which clips the top of some looping structures, as shown by the magenta field lines. Note that the actual open flux regions on the photosphere surface are the small and thin red colored regions in panel (b).

After neutral motions shift the photospheric footpoints, the distribution of integrated currents developing on open field lines is shown in Figures 2.8 (a) and (b). The steep gradient that exists in each panel of Figure 2.8 near $y \sim 80$ is associated with field lines that were identified as belonging to a separatrix in Figures 2.4 and 2.7. The behavior of current concentrations near separatrix surfaces is similar to what was observed when the integration began at the photosphere. Further, the integrated kinetic energy and pressure variation along field lines through the top boundary is given in Figures 2.8(c) and 2.8(d). The pressure variation shows discontinuities in agreement with the topology from Figure 2.7(a). The integrated kinetic energy shown in Figure 2.8(d) has discontinuities and strong gradients also in agreement with the topology. Along open flux, the integrated kinetic energy is of interest due to the observation by *Borovsky* (2008) that large angle changes in the magnetic field are associated with large changes in the plasma velocity.

Integration from the top boundary shows a number of distinct regions which exist as a result of the connection to underlying field. As the field evolves separatrices remain as boundaries to open flux bundles which map to parts of the photospheric surface with different characteristics. The existence of structure on open flux is dependent only on the topology of the field in the corona, while the specifics are influenced by the details of the photospheric motions and the resulting magnetic reconnection. The connection between photospheric conditions and open flux will be discussed in section 5.

2.4.3 Additional Initial Conditions

The statements in the previous two sections apply to many generic coronal magnetic field configurations and patterns of photospheric velocity. This is illustrated in Figure 2.9, where we keep the same magnetic field configuration, but the velocity perturbation is different, namely that given by case 2 of Table 2.1. The photosphere velocity is overplotted on the

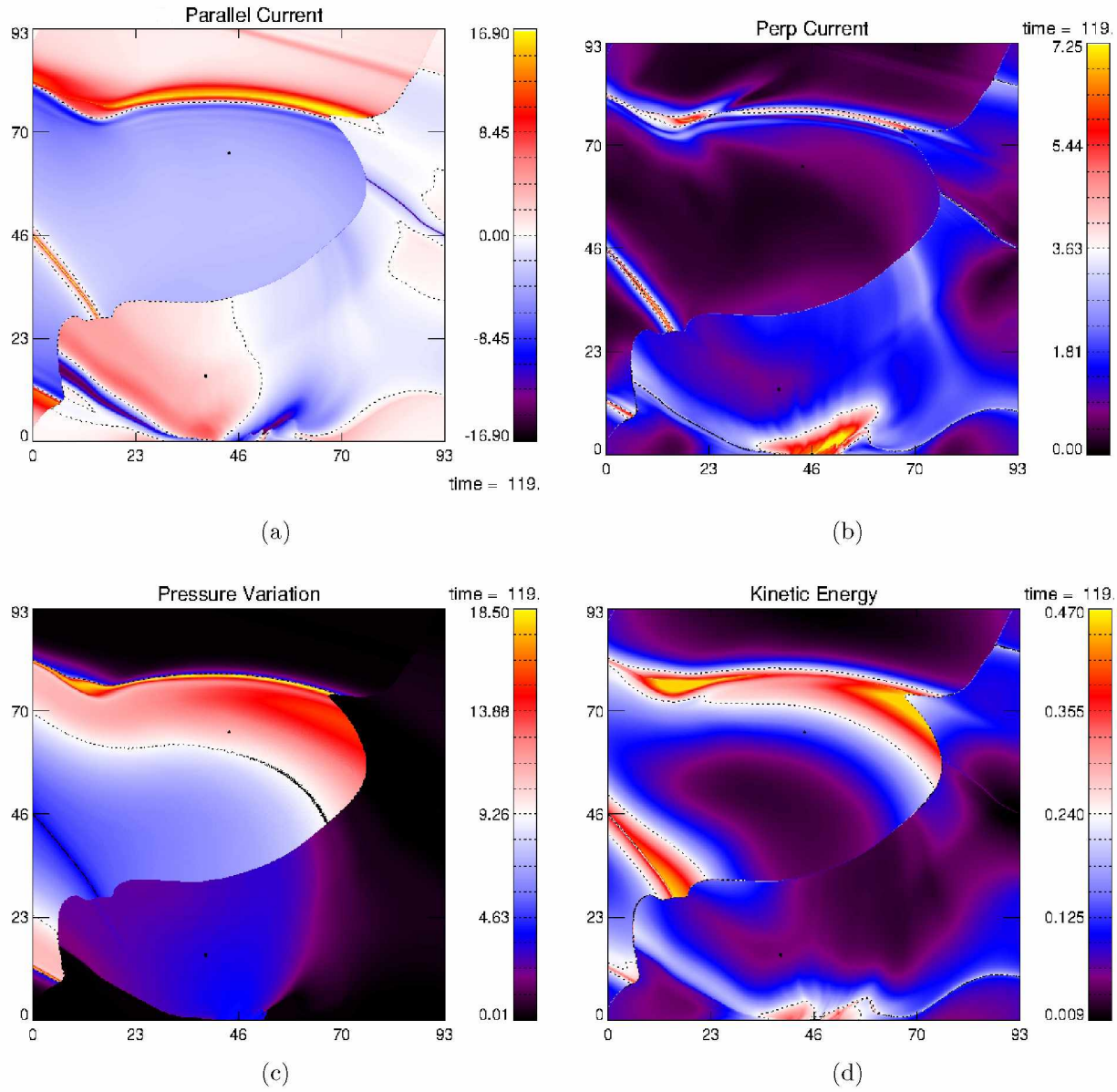

Figure 2.8: Field line integrated parallel (a) and perpendicular (b) current density, maximum pressure difference (c) along a field line, and field line integrated kinetic energy (d) for case 1 convection. All quantities have been integrated starting from the top boundary and are given for t = 119 Alfvén times.

integrated field-aligned current map in panel (a), and in panel (b) the photospheric velocity is projected along field lines to the top surface where the color gives integrated field-aligned current. These figures are to be compared with Figures 2.5(b) and 2.8(a). The thin current concentrations found in this and every other case tested indicate that changes in the initial conditions generate qualitatively the same results as found in Sections 4.1 and 4.2. This is in agreement with results by *Aulanier, G. et al.* (2005) for a magnetic field configuration with no null points, who also found that thin current layers form regardless of the specifics of the driving.

The specific pattern of footpoint motion will act perpendicular to the separatrix at some locations and parallel to it at others. It is expected that the details of the perturbation determine where the current is most concentrated and the resulting magnetic reconnection. The quasi-static evolution depends strongly on the integral path and non-local effects of Alfvén waves originating from all over the surface. A fully self consistent simulation for a simplified configuration is necessary to elucidate the details of current build-up in the vicinity of a separatrix layer.

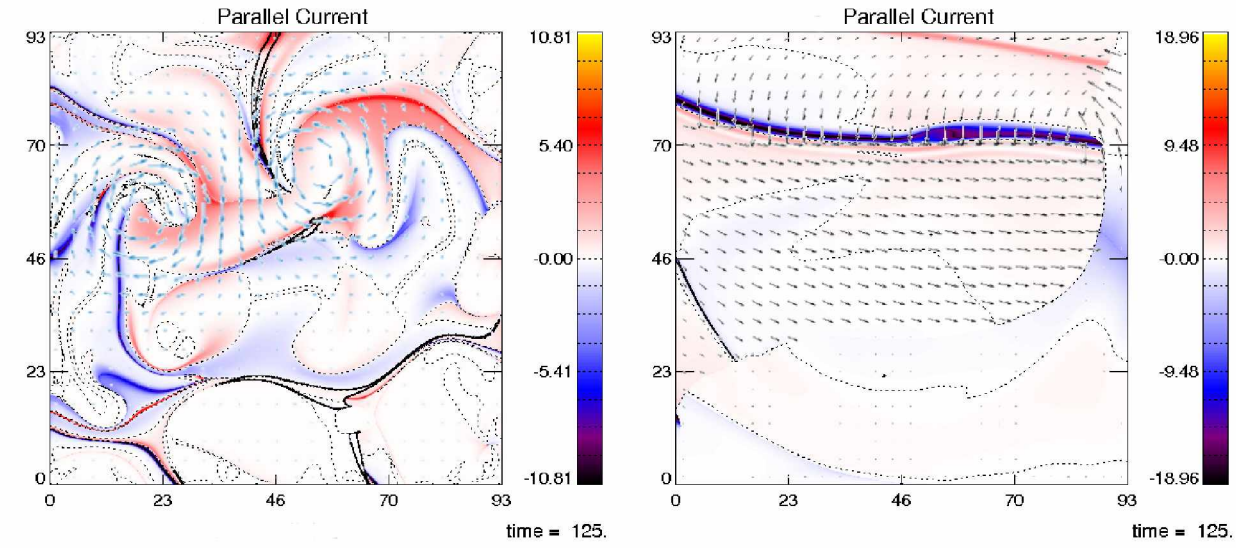

(a) (b)

Figure 2.9: Panel (a) presents field-aligned current integrated from the bottom boundary (in color) and photospheric convection velocity with arrows as characterized by case 2 of Table 2.1. Panel (b) presents field-aligned current integrated from the top boundary with arrows showing the photospheric convection velocity mapped to this boundary. These results for the photospheric convection are shown at t = 125 Alfvén times, i.e., for a state of the magnetic field evolution that is similar to the one shown in Figures 2.6 and 2.8.

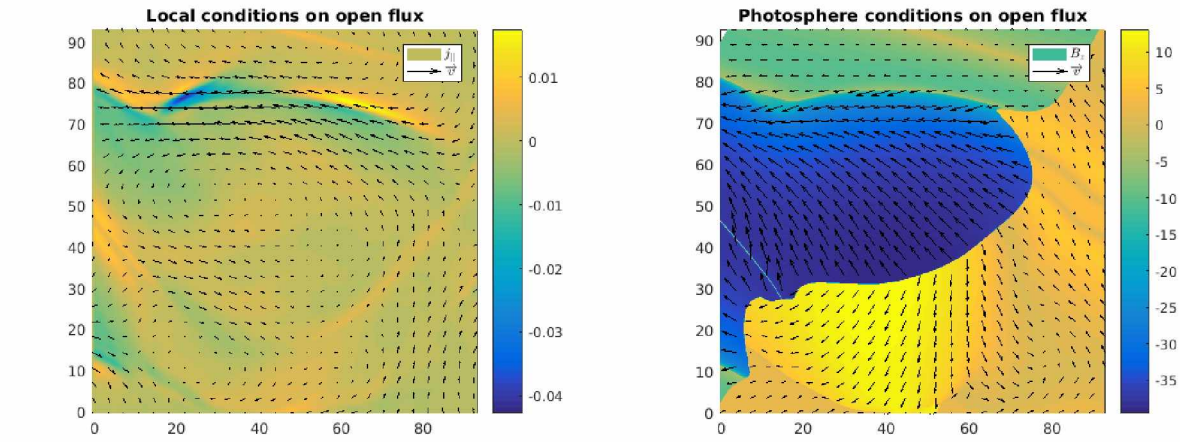

(a) (b)

Figure 2.10: Panel (a) presents the local field-aligned current density (color) and velocity components (arrows) for a horizontal slice just below the top boundary, showing several thin current layers concurrent with the field lines having large integrated parallel current from Figure 2.8. Panel (b) shows the photospheric B_z (color) and case 1 convection velocity (arrows) mapped along the magnetic field to the same horizontal slice as panel (a). A strong non-uniformity of parameters at the photosphere is indicative for large current density in panel (a), but not always.

2.5 Local Boundary Signatures and Potential Implications of Boundary Reconnection

Here we consider how strong gradients in the integral quantities are manifest in-situ. That is, in section 4 we integrated along field lines to determine where boundaries exist non-locally, while here properties of the plasma are examined locally. Strong gradients forming locally are found coincident with field lines that define topological features in the field, and therefore also a strong gradient in the integral properties. This is so because properties of the plasma at any height are connected with photospheric conditions that determine the perturbation.

In Figure 2.10, we compare conditions on the photosphere to the plasma at a plane just below the top boundary of the simulation (where the field line integration was started in section 4.2). The panel 2.10(a) (compare with Figure 2.8(a)) shows that the current density develops a number of strong gradients which agree with the location of field lines belonging to topological features. It may well be that these current layers become MHD discontinuities, however the nature of boundaries we find in-situ requires a detailed and more extensive study beyond the scope of this paper. In comparing with the field line integrated currents, the location of gradients is similar for some instances and not so for others. This is a consequence of the comparison between an in-situ and an integral property because

integrated signatures capture non-local structure.

Panel 2.10(b) gives the magnitude of the plasma velocity and B_z at the photospheric footpoints of field lines threading the top boundary, showing clearly the connection to different source regions. Nonuniformity at the photosphere and topological features defining the magnetic connection are responsible for the evolution of field line integrated quantities. The similarity in the location of gradients amongst the in-situ and field-line integrated pictures suggests a common origin. It is expected, though not a necessary condition, that larger integrated and local field-aligned currents would be associated with a large change of the tangential velocity at the photospheric surface. In comparison with Figures 2.8(c) and (d), Figure 2.10(b) also suggests that smaller photospheric velocity leads to smaller field-aligned pressure difference and small field integrated kinetic energy. This is not surprising, as the mapping alone does not define the physics and a deformation of the field is needed to build currents. This demonstrates the importance of the presence of strong photospheric convection in combination with the magnetic topological boundaries.

If flux tubes observed at Earth are attached to the sun, an important question is whether magnetic topological boundary structure present in the corona can be frozen into the solar wind flow. The alternative would be that the physics of flux tubes interacting in the solar wind flow is responsible for boundary structure observed at 1 AU. Whatever the case may be, magnetic reconnection acts wherever parallel electric fields break the frozen in condition and can work to reorganize some of the topology. Figure 2.11 shows the magnetic field line integrated parallel electric field for the bottom plane in panel (a) and the integrated parallel electric field along open flux in panel (b). This indicates that reconnection acts on both the open and closed portion of the field in the simulation. Large parallel electric fields occur where particle drift speeds are largest. This requires a combination of large current density and high resistivity, which is found at heights in the simulation near the transition region. Since it represents a relatively small portion of the flux, it may be the case that reconnection can significantly alter the open flux. This would change the connection of in-situ observed magnetic field and plasma to different regions at the photosphere and imply that in-situ boundaries are not fixed to a field line with a fixed connection to the sun. In other words, magnetic topological boundary signatures may not be frozen in as would be expected for tangential discontinuities, although it is not yet clear whether this is the case or not.

There are a number of outstanding questions concerning the role of reconnection in reorganizing the topology of the field and the signatures that it may leave on open flux. For instance, can reconnection between open and closed field alter the connection of a coronal flux tube to the photosphere? What is the exact nature of the reconnection occurring in thin

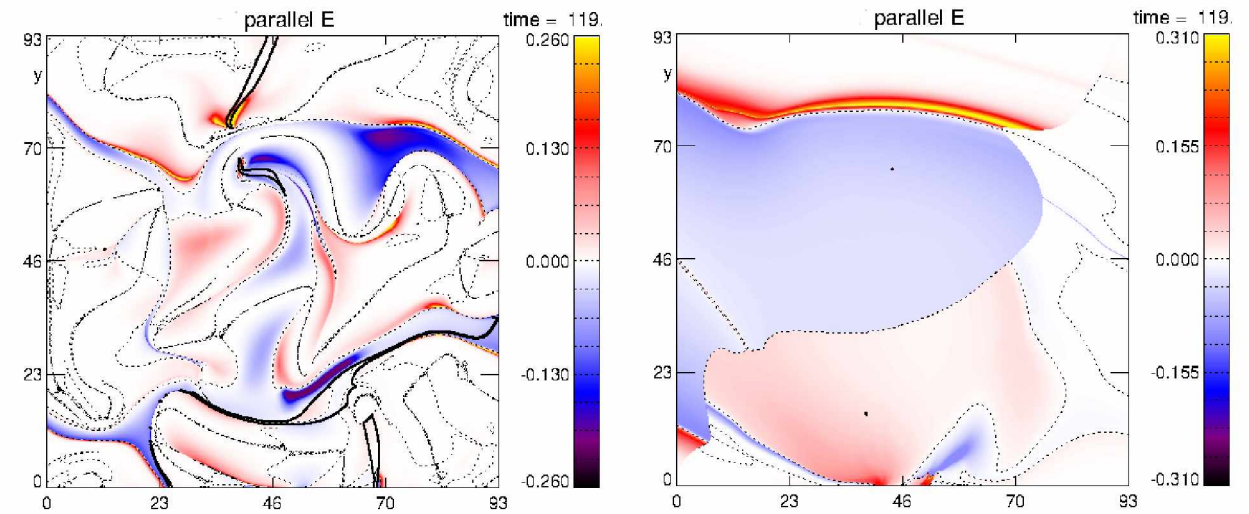

(a) (b)

Figure 2.11: For the case 1 convection pattern at t = 119 Alfvén times, the magnetic field integrated parallel electric field given by Ohm's law, $\int \eta j_{||}$, is shown as a measure of magnetic reconnection. Panel (a) is integrated from the bottom plane (photosphere surface) and panel (b) is integrated from the top plane (open flux).

layers? How are flux bundles filamented and does reconnection favor some scale? Will each bundle of open flux on the sun contain topological boundaries undergoing reconnection?

Lastly, are the reconnection effects small or do they play a role in characterizing physical properties of the boundaries on open flux? While reconnection does not destroy topological features it alters the nature of the boundary between two regions of different topology. Without reconnection this is likely a tangential discontinuity while with reconnection it should be a rotational discontinuity. Reconnection implies that an in-situ identified boundary is an open boundary in the sense that it is changing location relative to the plasmas on the two sides of the boundary. Thus reconnection should have several physical implications for plasma and magnetic field boundaries due to the presence of parallel electric fields.

2.6 Conclusions

Our results apply to a wide range of initial conditions in the simulation, corresponding to a spectrum of physically accessible states in the corona. Simulations are performed for a variety of magnetic field configurations and profiles of photospheric footpoint motion. The conclusions drawn here are also insensitive to the net open flux present in the system. In

addition, we varied the dimensions of the bounding box and the grid resolution to confirm that the conclusions are robust.

We summarize the results as follows:

1. **When Poynting flux is input to the system, large changes in integral properties of the magnetic field are a consequence of the magnetic topology associated with null points in the field.**

The connectivity in the solar magnetic carpet will bring different polarization and amplitude Alfvén waves into the same vicinity at a separatrix layer. Where the magnetic field mapping diverges, Alfvén wave propagation and reflection becomes discontinuous such that associated local magnetic field perturbations at a separatrix originate from very different locations in the photosphere. The photosphere surface is a nonuniform source and reflective boundary for Alfvén waves in accordance with the convection pattern and specific magnetic configuration.

Note that for the specific case in section 4, we have actually identified the topology for only a few features by locating the null and tracing field lines in Figures 2.4 and 2.7(b). For the cases where we have not shown a specific null point topology by tracing field lines, a thin feature in the FTV or discontinuity in conjugate B_z (such as the known example at $y \sim 80$ in Figure 2.7(a)) is a strong indicator for a topological feature. It is clear that any field line integrated quantity succeeds only partly in locating intense currents not only because of potential shortcomings of the method but as we have demonstrated, topology (including quasi-separatrix layers) is only a necessary condition for intense currents to develop. According to our result these currents also require a sufficient difference of the photospheric velocity at conjugate footpoints across the separatrix layer.

Although topological boundaries are usually associated with the presence of a tangential discontinuity where Alfvénic communication through the boundary is prohibited, Figure 2.11 indicates that reconnection can occur, in which case these boundaries become rotational discontinuities where both flow and magnetic field can be present in the direction normal to the surface.

2. **In-situ current layers are found coincident with field lines belonging to magnetic topological boundaries.**

Plasma at any height is connected with photospheric conditions that determine the magnetic perturbation. At a height in the simulation where most of the flux is open, the connection to different parts of the photosphere means points near topological boundaries will be characterized by a large change in photospheric conditions (i.e. driving velocity and direction, polarity, field strength). In particular, large changes in the photospheric velocity are responsible for large integrated as well as local current layers.

Diverging field line connectivity means changes in the system, which depend on conditions at both ends of a given field line, will be more drastic in the vicinity of a separatrix layer compared to a field line whose neighbors all connect similarly. Plasma separated from one region of connectivity can evolve quite independently of another when the boundary is a topological feature, as opposed to two plasmas in the same flux tube which simply experience a different forcing. The integrated kinetic energy and field-aligned pressure variation of the simulation suggest this, as large gradients are characteristic across a topological boundary for these quantities. Furthermore, the presence of not just large but also broad gradients in these quantities (compared to the width of the current layers) implies the plasma properties either side of a separatrix boundary may evolve to resemble the solar wind spaghetti picture given by *Borovsky* (2008).

3. **The continuum of "flux tube" sizes inferred by *Borovsky* (2008) may be indicative of the distribution of null points and quasi-separatrix layers in the coronal magnetic field.**

In the specific case we present, for the small fraction of total magnetic flux which reaches the top boundary, integrating along field lines shows two large regions and a number of smaller sized regions with a common magnetic topology. The footprints of open flux sources on the photosphere have scales sizes of a few Mm and tend to have elongated shapes with maximum width of about 1 to a few Mm and length of order 10 Mm. This contrasts with the development of turbulence in the solar wind since no characteristic length scales would be expected.

Flux emerging through the photosphere will preserve but shift around the overlying magnetic topology, and reconnection can alter the connection of flux while preserving the total magnetic flux present. Figure 2.11 indicates that these magnetic topological boundaries are the site of continuous reconnection close to the photosphere which reorganizes some of the magnetic field. This does not necessarily change the average footprint size for open flux because magnetic flux may just be exchanged between neighboring topologically defined regions. In addition, if the total number of null points does not change significantly over a typical solar area, the typical size and properties of separatrix boundaries does not change through reconnection. These null points would be expected to define the number of photospheric flux tubes.

There are a wide range of relevant time and spatial scales which are connected in this problem. The time scale over which magnetic topological features will persist must be related to the emergence and cancellation of flux which recycles the coronal field on a time scale of $\sim 1-2$ hours (*Close et al.*, 2005) for the smaller scales of the magnetic carpet. Since the recycling happens many times within the travel time of the solar wind, it is difficult to

envision that the magnetic connection of the rather small foot print sizes of open magnetic flux remain unchanged. Tracing the connection of a flux tube from the Earth all the way to the sun may contain a history of conditions at the solar surface, however, beyond the Alfvénic point, a flux tube is no longer connected to the sun and evolves independently of the solar conditions en route to 1 AU.

The supergranular turnover timescale, which has been observationally determined to be 1.5 days (*Roudier, T. et al.*, 2014), is shorter than the travel time of the solar wind to 1 AU. The convective motions combined with any ongoing reconnection processes determine where currents are distributed along the magnetic topological boundaries. The short $\sim$10 minute lifetime of granules (*Bahng and Schwarzschild*, 1961) would supposedly influence very small scale structures not resolved in this study.

Chapter 3

Magnetic Reconnection of Solar Flux Tubes and Coronal Reconnection Signatures in the Solar Wind at 1 AU

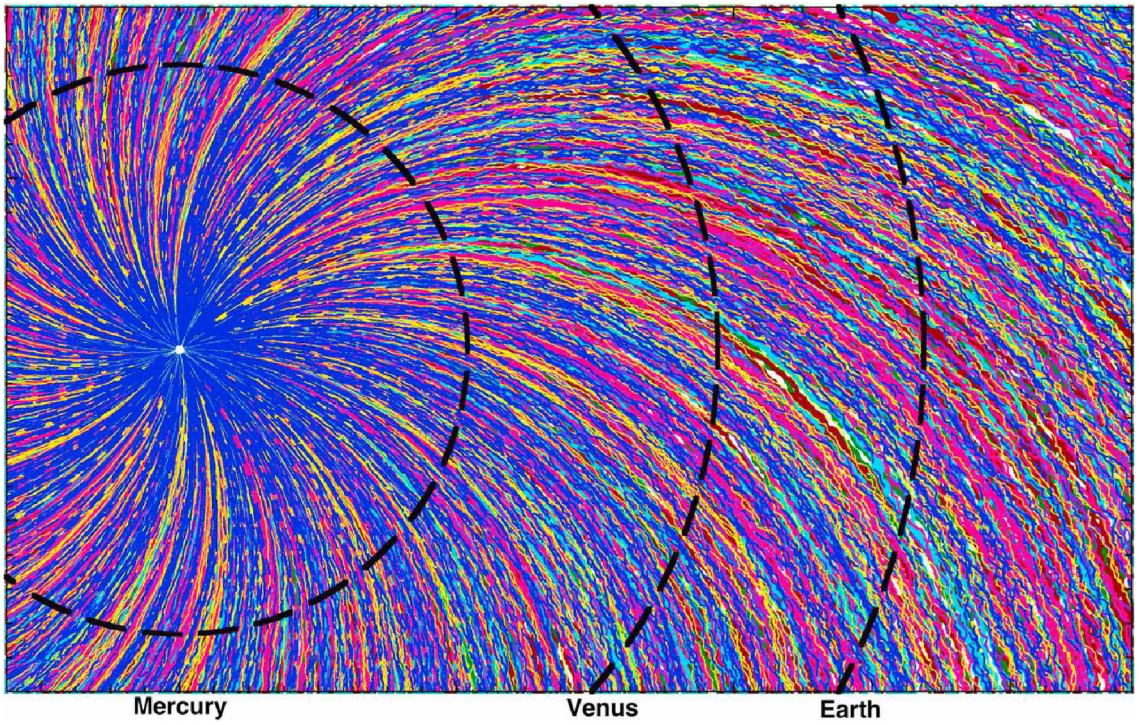

Figure 3.1: Does the connection of a flux tube observed at Earth reach all the way back to the surface of the sun? How far past Earth does it connect? *Reproduced from Borovsky* (2010).

Abstract[1]

The origin of interplanetary magnetic field that is frozen-in to the solar wind plasma flow is clearly magnetic flux from the sun's corona. However, the filamented structure of magnetic fields observed in the solar wind cannot be accounted for quite so simply. Given the 2 days or more for solar wind to travel from the sun to 1 AU, some argue that many current sheets are present due to turbulence and other in-transit effects in the dynamic plasma outflow. Alternatively, it is postulated that a "flux tube texture" of the solar wind exists as fossil structure of the corona. In this paper we examine the possible influence of magnetic reconnection occurring close to the sun or in the solar wind on the character of current sheets observed by MMS at 1 AU. Photospheric convection is used to perturb a magnetic carpet-like configuration which has well-segmented open flux tubes defined by topological elements of the magnetic field. Flux tube boundaries in the model are defined by magnetic sepratrix surfaces which are a preferential location for strong currents and magnetic reconnection. Reconnection is associated with signatures in the magnetic field and plasma that may advect with the solar wind all the way to 1 AU. Aided by three dimensional coronal modeling and two-dimensional simulation examples of reconnection layers, we examine properties of current sheets observed by MMS and how these solar wind boundaries may relate to reconnection operating earlier in the solar wind or corona.

3.1 Introduction

The survey of magnetic fields and interplanetary plasma at 1 AU given by *Borovsky* (2008) suggests that the solar wind contains many boundaries whose separation maps to a scale size of $\sim 1-50$ Mm on the solar surface. These preferred length scales are counter to arguments which invoke turbulence to explain solar wind structure. If successive solar wind boundaries mark the crossing into and out of "flux tubes," one would like to know if a flux tube can be traced all the way from Earth to the sun (*McCracken and Ness*, 1966; *Crooker et al.*, 2002; *Owens et al.*, 2011). In this way, it might possible to sound the conditions on the solar surface using spacecraft measurements near Earth.

The solar wind flux tube picture given by *Borovsky* (2008) argues that structure in the corona is seeded into the solar wind and expands into the heliosphere. *Borovsky* (2006) also notes that there is little mixing of the plasmas on either side of these boundaries. For the purpose of this paper, we will use the term magnetic flux tube synonymous with a magnetic flux region that has the same topological connection to the sun. While the magnetic field

[1]Manuscript coauthor: A. Otto

is recycled in just a few hours for small scales in the magnetic carpet (*Close et al.*, 2005), magnetic topological features would be expected to persist over such time periods even in the presence of significant ideal perturbations. Magnetic separatrix layers are ubiquitous in the highly structured magnetic carpet at the base of the corona (*Longcope and Parnell*, 2009).

A topologically defined flux tube structure of the appropriate scale in the coronal magnetic field and plasma has been examined using three-dimensional magnetohydrodynamic (MHD) simulations by *Burkholder et al.* (2018). The quasi-static evolution of a force free magnetic field extrapolation was driven by photospheric convection and many strong gradients in magnetic field line integrated and in-situ plasma properties were found. These gradients mostly coincide with separatrix boundaries such that topological boundaries become physical boundaries. Photospheric properties and inhomogeneous perturbations determine the plasma properties in the flux tubes and the discontinuous mapping between neighboring flux tubes paints the top of the corona in a manner somewhat like Figure 1 of *Borovsky* (2008).

The separatrix and quasi-separatrix layers associated with magnetic null points are preferential locations for the development of intense electric current (*Démoulin et al.*, 1996b; *Parnell et al.*, 2010; *Pontin et al.*, 2004, 2005, 2007; *Priest and Démoulin*, 1995; *Priest and Pontin*, 2009). In the solar magnetic carpet the origin of these currents is the diverging connectivity of field lines across a magnetic separatrix or quasi-separatrix layer along with the different photospheric convection in the disjunct flux regions (*Burkholder et al.*, 2018). Strong currents at a separatrix or quasi-separatrix boundary can drive magnetic reconnection which alters the connection of field lines either side of the boundary and changes the magnetic topology (*Santos et al.*, 2011). The open-open (slippage) (*Pontin et al.*, 2005; *Masson et al.*, 2012) and open-closed (interchange) (*Pontin and Wyper*, 2015) reconnection modes are of particular interest since they have consequences for the time-dependent connection of an open flux tube to the photosphere.

There are several mechanisms that can lead to the evolution of arbitrarily thin (singular) current layers and the onset of reconnection, while the magnetic field remains very close to an equilibrium up to this point. Equilibrium current sheets in a magnetotail-like configuration have been studied in the presence of boundary perturbations (*Schindler and Birn*, 1993). The perturbations drive the configuration to a critical point where the equilibrium ceases to exist. A singular (infinitely thin) current sheet forms at this point and magnetic reconnection cannot be avoided. The work by *Hsieh and Otto* (2014), also specifically catered to the magnetotail, argues that diverging flows can deplete flux in the near-Earth magnetotail leading to a very thin current sheet.

Parker (1972), using a uniform magnetic field, suggested that evolving currents can become singular. In solar magnetic field simulations conducted by *Burkholder et al.* (2018),

photospheric motion generates magnetic field-aligned currents, which can become strong and thin current sheets. Thin current sheets in these solar simulations form due to magnetic topology and the nonlocal character of the perturbations. When these currents surpass a critical threshold, reconnection can set in such that the equilibrium is lost and the magnetic field undergoes a dynamic reconfiguration. However, until a singular current sheet appears (with the onset of reconnection), the configuration remains a force free equilibrium.

The concept of the reconnection layer has been studied in the literature for many years (see (*Sonnerup*, 1979)). Associated with magnetic reconnection are typical signatures that can be found at the boundary between outflow and inflow regions (*Yamada*, 2011). A theoretically expected signature of magnetic reconnection is the presence of switch-off shocks *Petschek* (1964) or rotational discontinuities (*Levy et al.*, 1964). One-dimensional (1D) analogs of the reconnection scenario have been studied (*Lin et al.*, 1992; *Lin and Lee*, 1993, 1995; *Biernat et al.*, 1989). They find the character of slow shocks and other discontinuities bounding the reconnection outflow depend on the specifics of the reconnection configuration. An important aspect of the reconnection layer is the changes in plasma properties which would be observed for a spacecraft passing though the outflow boundary.

Without reconnection operating on topological flux tube boundaries, these boundaries must be tangential discontinuities (*Longcope*, 2005), because there is no magnetic connection across such a boundary. Note however, that the inverse is not necessarily true. The presence of reconnection for some period of time does not imply the entire boundary is open, because the reconnection effects are limited in space and time depending on where and how long it operates, such that a significant part of the original boundary can still be a tangential discontinuity. Additionally, the finite travel time for Alfvén waves to set up the current must play a role in where and how long reconnection operates.

A small component of magnetic field normal (B_n) to the separatrix is one characteristic of reconnection acting on a flux tube boundary but also these boundaries should contain Alfvénic layers which satisfy the Walén relation. This relation is a result of the tangential stress balance for a plasma moving across a layer with $B_n \neq 0$ (*Sonnerup et al.*, 1987; *Sonnerup et al.*, 1995). Another characteristic of the reconnection layer which is important for a low β plasma such as the corona is nonadiabatic heating caused by slow shocks bounding the outflow region (*Ma and Otto*, 2014). If these signatures remain intact under the influence of solar wind dynamics they may be the origin of the "flux tube" structure of the solar wind observed at Earth. We will use two-dimensional examples of the boundary of reconnection layers to better understand and illustrate expected signatures of these boundaries.

To determine if solar wind current sheets near Earth might be reconnection outflow boundaries, we classify current sheets observed by the Magnetospheric Multiscale (MMS) spacecraft

at 1 AU using the Flux Gate Magnetometer (FGM) (*Torbert et al.*, 2016) and Fast Plasma Investigation (FPI) (*Pollock et al.*, 2016) instruments. Previous studies have shown the difficulty in determining the exact properties of each boundary (*Smith*, 1973; *Knetter et al.*, 2003, 2004; *Neugebauer and Giacalone*, 2010). The high cadence and high quality data provided by MMS could provide the most accurate analysis yet, however the MMS particle instruments are optimized for typical distributions of the magnetosheath and magnetotail. This can be corrected by using a Fourier space filtering (*Bandyopadhyay et al.*, 2018). Instrumental errors likely still dominate the uncertainty where the FPI instrument is used but fortunately a statistical analysis can be made using a large sample of events.

The events in section 6 occur in non-ejecta solar wind plasma. Non-ejecta plasma comes from three regions of the solar wind: (1) coronal holes, (2) streamer stalks, and (3) either the edges of coronal holes or coronal-hole open flux tubes reconnecting with high magnetic arches in the streamer belt. Streamer stalk plasma does not have strong current sheets. Plasma (3) tends to have weakly Alfvénic current sheets with Δv_A larger than Δv. Coronal-hole plasma (the classic fast wind) has Alfvénic current sheets. The topology of the open flux tubes in the coronal holes is fairly well understood: they are trapped in down-flow lanes at the edges of supergranules and are not random flux tubes in the magnetic carpet (*Gabriel*, 1976; *Tu et al.*, 2005; *Wilhelm et al.*, 2011; *Yang et al.*, 2013).

The goal of this paper is to examine the role that magnetic separatrices in the solar corona can play in sourcing boundaries between distinct plasmas and magnetic fields in the solar wind. In section 2, we describe the three-dimensional (3D) MHD simulation model of the magnetic carpet and open solar flux tubes. In section 3, the reconnection effects are illustrated qualitatively at separatrix boundaries to understand the time-dependent connection of magnetic field lines near topological features. Section 4 shows some aspects of reconnection layers in the 3D model. In section 5, an expected signature for remote observation of reconnection is developed using a two-dimensional (2D) MHD simulation. Section 6 begins with simulation results of reconnection outflow boundaries for different values of plasma β, which is important since this parameter changes by 2 orders of magnitude or more from the corona to 1 AU (*Iwai et al.*, 2014; *Mullan and Smith*, 2006). Then a statistical analysis of MMS data is performed to determine whether plasma and magnetic field properties at solar wind current sheets are consistent with a reconnection outflow boundary. A conclusion section is included to discuss and summarize the findings.

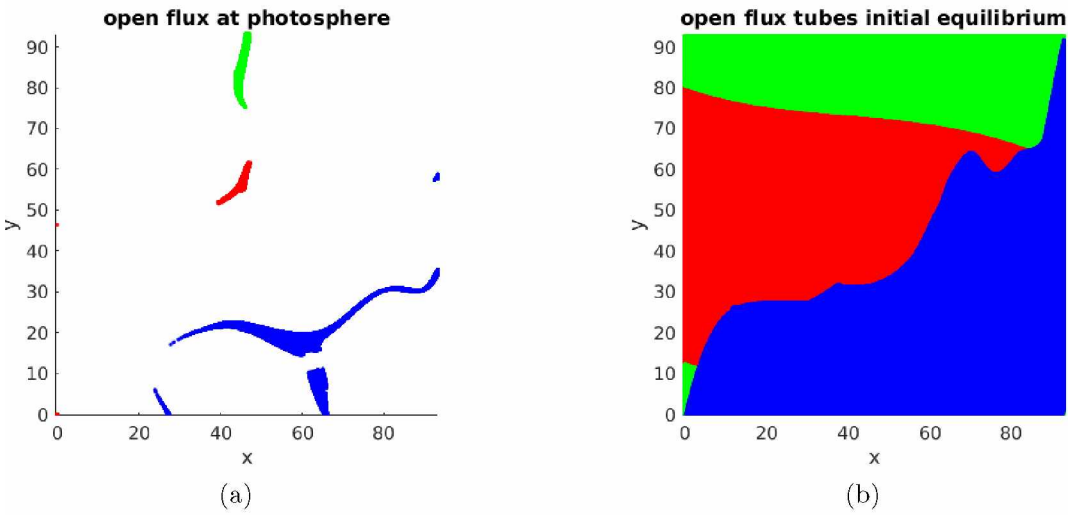

(a)

(b)

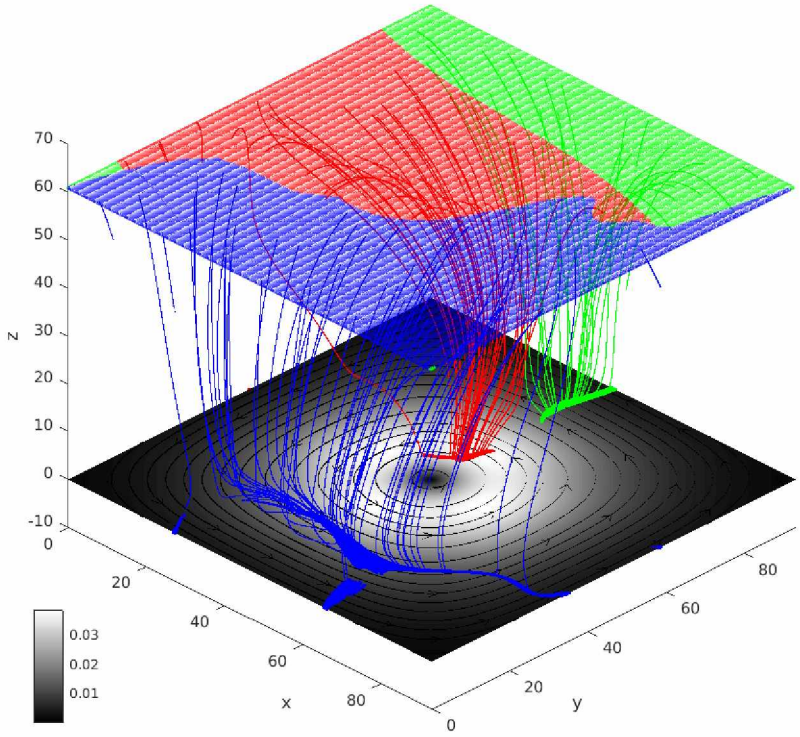

(c)

Figure 3.2: A model of the flux tube structure in the solar magnetic carpet. On the bottom boundary (a), colors give the photospheric area for the different flux tubes of open magnetic field. Discrete points are the result of the finite integration resolution beginning from the top boundary. At the top boundary (b), open flux tubes fill the volume and the colors are defined by their footpoints at the photosphere. In (c), magnetic field lines map the photosphere perturbations (greyscale colormap for magnitude and streamlines for direction) onto open flux.

3.2 Simulation model

The numerical model is a first order approximation of the structure of the solar magnetic carpet near the photosphere surface and low in the corona. The initial magnetic field configuration is a linear force free extrapolation (*Otto et al.*, 2007) of a SOHO line of sight magnetogram as in *Adamson et al.* (2013) and *Burkholder et al.* (2018). The background plasma has no variation with height in thermal pressure but an artificial transition layer in the density and temperature given by Figure 2 of *Adamson et al.* (2013). The initial magnetic field configuration described in *Burkholder et al.* (2018) (see Figure 1 in *Burkholder et al.* (2018)) is perturbed by the horizontal convection of neutrals in the photosphere. The specific flow pattern is given by

$$\mathbf{u}_0(x,y,t) = \nabla \times \left[\frac{1}{\cosh(\frac{y-x}{12})\cosh(\frac{x+y-92.8}{12})}\right]\hat{\mathbf{z}}$$

which is a single divergence free vortex of the supergranular scale in the chosen normalization.

The system evolves according to the normalized resistive MHD equations:

$$\frac{\partial \rho}{\partial t} = -\nabla \cdot \rho\mathbf{u}$$

$$\frac{\partial \rho\mathbf{u}}{\partial t} = -\nabla \cdot \rho\mathbf{u}\mathbf{u} - \nabla h^\gamma + \mathbf{j} \times \mathbf{B} - \nu\rho(\mathbf{u} - \mathbf{u_0})$$

$$\frac{\partial h}{\partial t} = -\nabla \cdot (h\mathbf{u}) + \frac{(\gamma-1)}{\gamma h^{\gamma-1}}\eta\mathbf{j}^2$$

$$\frac{\partial \mathbf{B}}{\partial t} = \nabla \times (\mathbf{u} \times \mathbf{B} - \eta\mathbf{j}),$$

as given by *Adamson et al.* (2013). The variable ρ is the mass density, $\mathbf{u}$ is the plasma velocity, $h = (p/2)^{1/\gamma}$ where p is the thermal pressure, $\mathbf{j}$ is the electric current density, $\mathbf{B}$ is the magnetic field vector, and η is the resistivity. The value of ν couples the neutral convection pattern to the plasma for only a few grid cells above the photosphere. The polytropic index is set to $\gamma = \frac{5}{3}$.

The quasi-static time dependence of the configuration is calculated with a finite difference approximation on a $253 \times 253 \times 153$ Cartesian grid encompassing a volume $92.8L_0 \times 92.8L_0 \times 61.8L_0$. Mirror symmetric boundary conditions are used at the x and y boundaries to satisfy the symmetry of the MHD equations (*Otto et al.*, 2007). These boundary conditions allow the simulation to save resources by carrying out the integrations for only a quarter of a doubly periodic domain. The current-dependent resistivity model is described in *Adamson et al.* (2013). Other specific aspects of the numerics, normalization, grid, boundary conditions, and initial conditions for the model are given in *Burkholder et al.* (2018).

In this investigation, we will qualitatively examine the evolving connection of open flux in the simulation and the signatures that are found at the boundaries between flux tubes. As described in *Burkholder et al.* (2018), open flux in this model accounts for only a small percentage of the photospheric area, but the area of open flux permeating a given horizontal plane expands to fill the volume moving towards the top boundary. This gives a structure of open flux at the photosphere and high in the corona corresponding to Panels (a) and (b) of Figure 3.2.

Panel (a) is the bottom boundary of the simulation with the photospheric footpoints of all the open flux in color. The different colors for the individual concentrations of open flux are representative of a different location on the photosphere. The discrete points in this picture are a result of integrating a grid of field lines starting at the top boundary. In Panel (b), the top boundary of the simulation is segmented into well-defined flux tubes, with the colors corresponding to the mapping of open flux from Panel (a). It is important to note that even though parts of the blue flux tube appear separated from one another on the photosphere, this is only due to the finite resolution of the integration. Given sufficient resolution, the blue sliver at $x \sim 25,\ y \sim 0$ is connected to the corresponding blue region at $y \sim 20$, so they are defined as the same flux tube topologically, but may be considered to be separated by a quasi-separatrix layer.

The connection of Panel 1 to Panel 2 is given in Panel 3, where colored field lines give a fully 3D view of the flux tube structure on open field. The green and red regions of open flux map to localized footpoints on the photosphere, whereas the blue region of open flux maps to a thin sliver extending across a large portion of the photosphere surface. The grayscale color of the photosphere gives the magnitude of the photospheric convection that drives the simulation, with streamlines giving the direction of forcing.

3.3 Reconnection in the Solar Magnetic Carpet

Flux tube boundaries in this model are defined topologically by the magnetic separatrix surfaces associated with null points in the magnetic field. Magnetic reconnection has been studied extensively in the solar corona (*Aulanier, G. et al.*, 2005; *De Moortel, I. and Galsgaard, K.*, 2006; *Pontin et al.*, 2013) and it has a number of important implications. With magnetic reconnection acting on the boundary between flux tubes, the exchange of flux from one flux tube to its neighbor means the boundary is moving with respect to the plasma. In addition, magnetic reconnection leaves a telltale signature where it acts which might be evidence for these flux tube boundaries that can be observed in the solar wind.

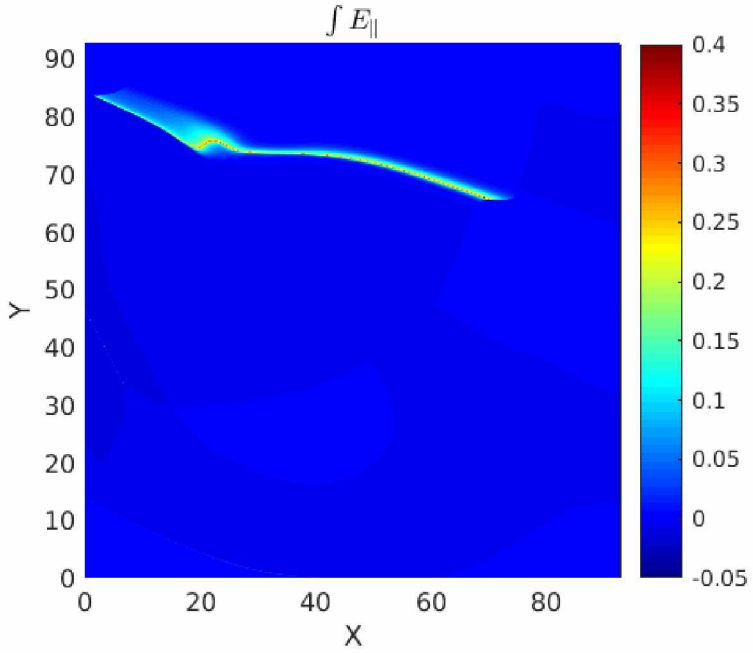

Figure 3.3: Integrated magnetic field-aligned electric field $\int E_{||}$ on open flux at $t = 180\ t_A$. The layer of large $\int E_{||}$ at y$\sim$ 80 shows magnetic reconnection occurring between the red and green flux tubes as given in Figure 3.2.

Burkholder et al. (2018) integrated the electric field parallel to the local magnetic field direction ($E_{||}$) and found the most intense concentrations at the boundaries between flux tubes. The presence of $E_{||}$ breaks the frozen-in condition and is required for magnetic reconnection (*Hesse and Schindler*, 1988). By integrating along 1001×1001 open field lines, Figure 3.3 presents the field line integrated $E_{||}$ at the top boundary for the simulation results in this paper. The feature at $y \sim 80$ dominates by an order of magnitude over any other regions of integral $E_{||}$. This provides an image of where magnetic reconnection is operating after driving the simulation for $t = 180$ Alfvén times (t_A).

After the evolution, the shapes of open flux tubes as given at the initial condition in Figure 3.2(b) are changed. This is due to reconnection but also because the ideal evolution of the system in regions of $\eta = 0$ convects magnetic field lines. With this in mind, it is clear that the layer of large integral $E_{||}$ in Figure 3.3 is the boundary between green and red flux tubes (Figure 3.2). Other very thin enhancements of integral $E_{||}$ exist but they are far smaller in magnitude.

As another way to probe the effects of magnetic reconnection one can use the frozen-in condition. By tracing the ideal evolution of the magnetic field, this can be compared with the actual connection of the field between the top (open flux) and photospheric boundaries. For this purpose we trace the convective displacement of magnetic foot points at the top and

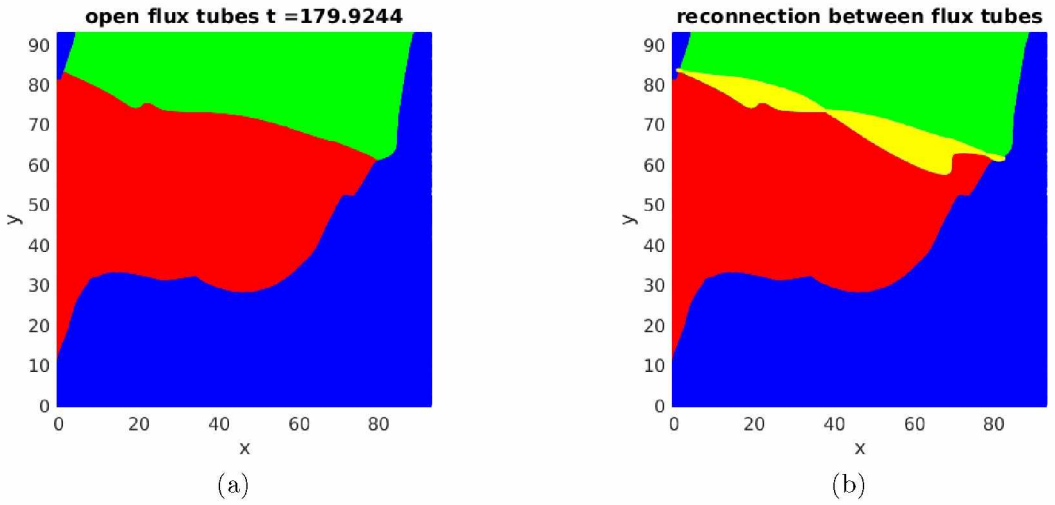

Figure 3.4: Flux tube structure of open magnetic field at $t = 180\ t_A$. The yellow highlighted regions in Panel (b) give the area of reconnected flux at $t = 180\ t_A$.

the bottom boundaries. In an ideal evolution two conjugate traced footpoints of an open field line should remain connected by a field line at all times during the evolution. This is the case within a very small numerical inaccuracy for most of the traced foot points. However, in the vicinity of flux surfaces with a large integral parallel electric field this connection is broken and the photospheric connection of a fluid element at the top boundary changes.

The changing connection of open flux tubes as a result of magnetic reconnection is visualized in Figure 3.4. Recall Panel (b) of Figure 3.2, which gives the open flux tube structure at the beginning of the simulation, with colors representing the connection to a different region of the photosphere. Panel (a) of Figure 3.4 is the shape of the flux tubes after magnetic reconnection and plasma motions have acted on the boundaries between flux tubes for $t = 180\ t_A$. Panel (b) is an exact replica of (a) except for the yellow highlighting. These highlighted regions represent open reconnected flux, i.e., field lines which have changed their connection to a different source region at the photosphere. Magnetic flux is being coherently exchanged across the separatrix such that a fluid element originally connected in the green flux tube is now connected in the red, and vice versa.

There is no reconnection occurring between the blue and red or blue and green flux tubes. This is expected since there is no separatrix boundary and no current layer that exists on these field lines. These flux tube boundaries are formed only due to the finite height of the simulation volume. Quantitatively, $\sim 3\%$ of the open flux is reconnected at $t = 180\ t_A$. It is important to note that the maximum current density and parallel electric field are not saturated at this point in the simulation. At $t = 300\ t_A$ the percentage of reconnected open

flux is $\sim 5\%$ and the reconnection rate is saturated. Local reconnection signatures in the 3D simulation and the reconnection rate will be discussed further in Section 5.

To illustrate the exchange of flux across a separatrix boundary, Figure 3.5 shows a number of open magnetic field lines mapping near the boundary between red and green flux tubes. Both panels show a view looking down from the top boundary of the simulation. The transparent grey surface represents fluid elements threaded by a magnetic field line in the yellow highlighted portion from Figure 3.4(c). The mapping of field lines threading these fluid elements at the beginning of the simulation, given in Figure 3.5(a), shows the red field lines map to a location on the photosphere $y \sim 60$ while the green field lines map to $y \sim 75$ at $t = 0$. Under an ideal MHD evolution, the magnetic footpoint threading a fluid element would be convected to the same colored slivers (red or green) on the photosphere. The actual evolution for the magnetic connection of the fluid elements is given by Panel (b), where the connection to the photosphere has swapped for green and red magnetic field lines at $t = 180$ t_A. The black slivers on the photosphere show where the fluid elements on open flux are connected in comparison to the ideal evolution (green and red slivers). Fluid elements whose connection at the photosphere was initially in the green flux tube are now attached to the photosphere where the red flux tube is defined, and vice versa for fluid elements originally in the red flux tube.

For a fluid element originally (at time $t = 0$) belonging to the green flux tube, the plasma properties are perturbed due to the forcing at the green footpoint on the photosphere. When the connection changes so that it is connected to the red photospheric footpoint, this implies a change of the perturbation due to the inhomogeneity of photospheric forcing. The time integrated result of the changing perturbation to a fluid element on open flux will be an effective mixing. The evolution of plasma properties in different flux tubes is illustrated in the next section, which, although represent open boundaries due to the reconnection, show how the perturbations to a reconnected field line would change after its connection to the photosphere changes. Although this would appear inconsistent with *Borovsky* (2006) who finds little mixing at flux tube boundaries, reconnection signatures propagate at the Alfvén speed superposed on the solar wind velocity so mixing may be difficult to observe after the transit to 1 AU. The definition of mixing depends on what properties are being examined. Electrons, energetic particles, and waves all propagate at different speeds so mixing properties driven by reconnection in the corona may be impossible to determine from an observation at 1 AU.

The specific case in Figure 3.5 is an example of "slippage" between magnetic field lines. The green and red flux tubes are both of the same polarity (sign of B_z), so it must be that B_x and/or B_y have anti-parallel components. By examining the integrated parallel electric

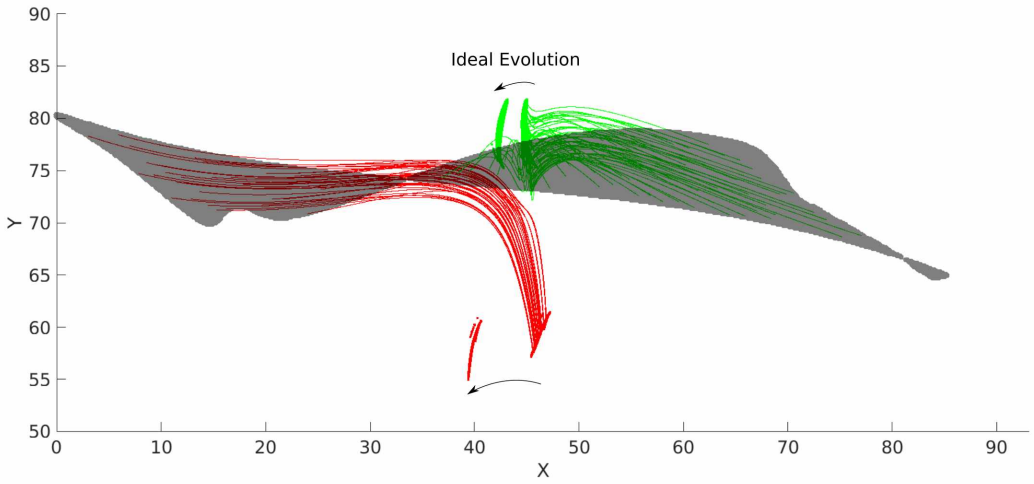

(a) t = 0

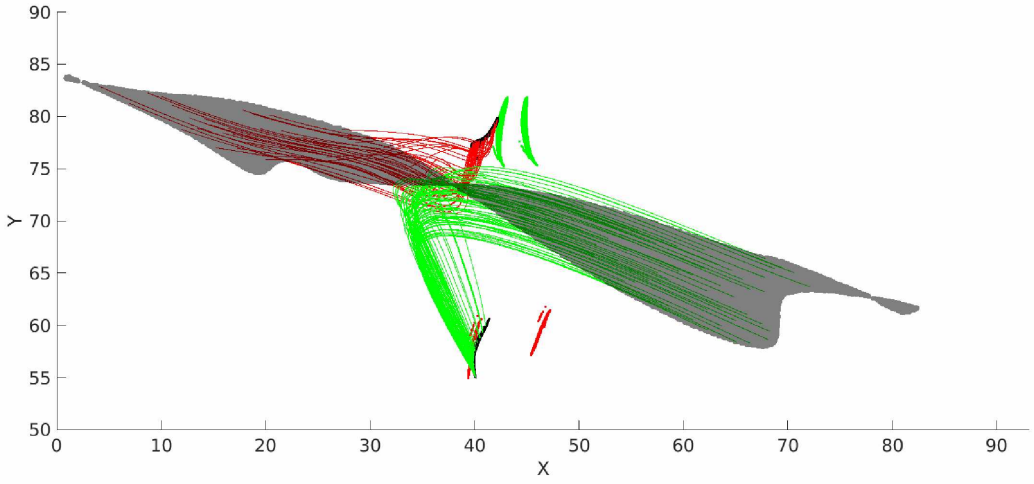

(b) t = 180

Figure 3.5: Reconnection between red and green flux tubes. Panel (a) shows the connection of open field for the initial condition, with the slivers of color on the photosphere indicating the initial footpoints for open flux and the corresponding location after an ideal evolution. In Panel (b), photospheric convection has acted on the field and all of the same field lines are traced as given in Panel (a). The black slivers in (b) indicate where the footpoints for open flux lie given the non-ideal evolution.

field on closed flux (not shown), it is clear that other modes of reconnection take place in this model of the solar magnetic field, i.e. closed-closed and open-closed "interchange" reconnection. Regardless of which mode of reconnection is acting, there are a number of tracers for a reconnection layer that can be identified in the simulation and also in spacecraft data.

3.4 Properties of Flux Tube Boundaries

Many strong and thin current layers develop in the model solar magnetic field where magnetic reconnection can take place. These occur at magnetic separatrices and quasi-separatrix layers where the magnetic field line connectivity diverges. Topologically disconnected flux tubes are connected to the photosphere at different locations where the convective motions are different. This causes different perturbations to the different flux tubes, such that the evolution of plasma and magnetic field is different for neighboring flux tubes.

An example of this is shown in Figure 3.6. A one-dimensional cut has been taken through the 3D simulation in a direction that is locally normal to a current layer which develops near the separatrix boundary of a magnetic null point. The x-axes give the coordinates of the 3D profile projected onto the simulation x-axis. The left panel of Figure 3.6(a) shows at the initial condition (t_i) the potential magnetic field has only gentle gradients and a fairly constant profile of the plasma β. Note while β is smaller than 1, it is overestimated compared to typical conditions in the corona where $\beta < 1$. The right panel of Figure 3.6(a) shows the magnetic field projected into boundary normal coordinates (determined by the current layer at $t = 119$), which has a minimum in the normal component B_n at $x \sim 65.5$, indicating approximately the location of the separatrix boundary. The colors purple and orange indicate whether the x-coordinate is to the left or right of this minimum, respectively. At the initial condition the profiles for thermal pressure, density, velocity, and specific entropy $S = p/n^\gamma = T/n^{\gamma-1}$ (*Birn et al.*, 2006, 2009) are flat, indicating the separatrix layer is only a topological boundary at $t = 0$.

After the convective motions have acted for $t = 119\ t_A$, the different flux tubes have been perturbed such that they each harbor a different plasma, as shown in Figure 3.6(b). The magnetic field profile shows a strong rotation which is indicative of a current layer developing on or near the separatrix boundary, as expected. The B_y component rotates from 1.5 to a value slightly less than zero, while the other components stay relatively constant in comparison. When projected into variance coordinates (right-handed coordinate system defined by the maximum, intermediate, and minimum variance directions) the maximum variance component shows a highly asymmetric anti-parallel component of magnetic field at

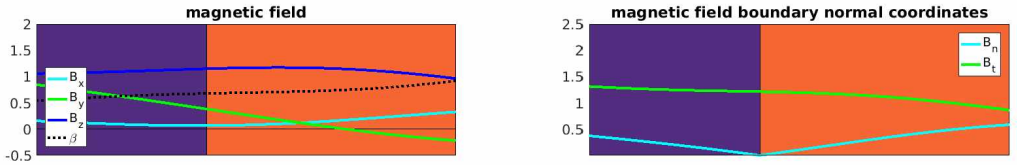

(a) $t = 0$

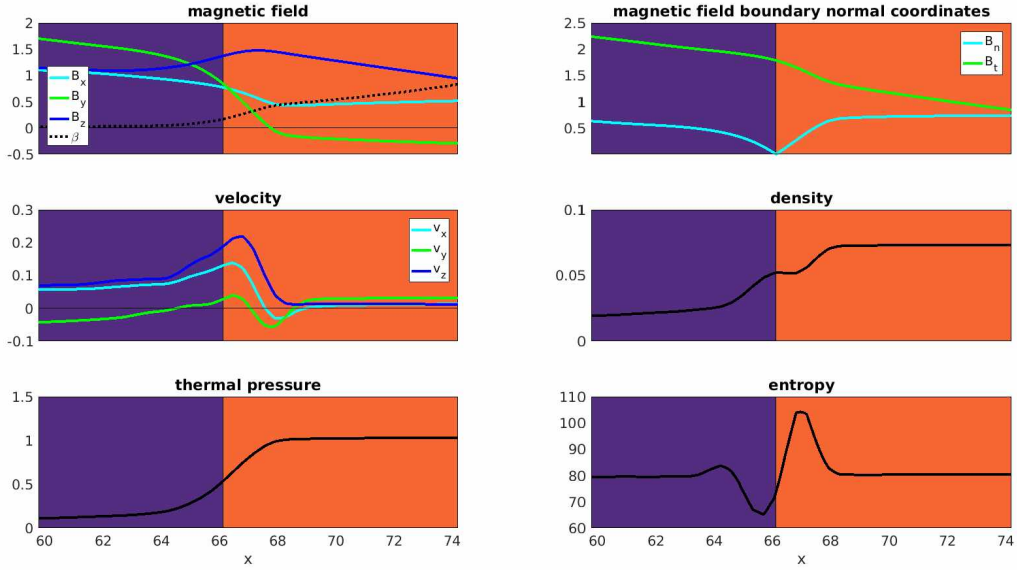

(b) $t = 119$

Figure 3.6: One-dimensional cut at the initial condition (a) and t = 119 t_A (b) through a magnetic separatrix layer. The boundary normal coordinates are determined from the magnetic field at t = 119 t_A. The purple and orange colors represent either side of the separatrix boundary.

this boundary (not shown). This indicates that magnetic reconnection is possible, while the other panels show that if magnetic reconnection is taking place at this boundary it is in its infancy.

The profile of velocity shows jetting plasma whose peak does not coincide exactly with the separatrix boundary but lies more in the orange flux tube. Away from the separatrix, the velocity in the orange flux tube is close to zero while nonzero values are found in the purple flux tube. This plasma motion is responsible for field-aligned transport such that the density has been decreased in the purple flux tube from its initial value, while the density in the orange flux tube has remained relatively constant except for near the separatrix. The density exactly on the separatrix lies between the perturbed densities of orange and purple flux tubes. This may be the beginning stage of compression associated with a reconnection outflow. The thermal pressure profile shows the perturbed temperature in the purple flux tube has decreased significantly from its initial value, which is also the cause for the very small value of β that now exists in the purple flux tube. Finally, the specific entropy shows both a peak and a valley near the separatrix boundary. The peak may be indicative of nonadiabatic heating in the reconnection outflow, while the valley must be material transported into the vicinity of the chosen profile.

The different plasma properties in the different flux tubes suggest that reconnection layers on the sun are unlikely to be symmetric. Magnetically disconnected flux tubes can not easily smooth out gradients across a flux tube boundary. This property holds until magnetic reconnection has produced a component of magnetic field that threads the boundary and mixing can take place. The asymmetries of the reconnection configuration have consequences for the structure of the outflow, which is important since the outflow boundaries of reconnection on the sun may be observable at 1 AU.

Figure 3.7 shows a 1D cut through a separatrix layer near a different reconnection site in the 3D simulation at $t = 119\ t_A$. The asymptotic values of the plasma properties in the different flux tubes are similar such that the signatures of reconnection are more clear in this example compared to Figure 3.6. The magnetic field from the top left panel has an anti-parallel component B_x of magnetic field which switches sign near $x \sim 62$. When rotated into a variance coordinate system in the top right panel, anti-parallel magnetic fields occur near $x \sim 59.5$ and $x \sim 62$. This coordinate system also shows that the guide field is important at this reconnection site. Two closely separated peaks in the current density suggest the reconnection layer is early in its development. The local $E_{||}$ also has two peaks and asymptotic values of zero moving away from the separatrix. The velocity profile possibly shows jetting plasma in the outflow, although the peaks are not as localized as one would expect. Density and thermal pressure are enhanced in the outflow. Finally, the peaks in

specific entropy are indicative of nonadiabatic heating. The larger ($x \sim 63$) peak of entropy coincides with the larger peaks in the current density and $E_{||}$, and similarly the smaller peak ($x \sim 59$) in entropy coincides with the smaller of the two peaks in current density and $E_{||}$.

The jetting plasma, localized peaks in $E_{||}$, density enhancement, and nonadiabatic heating are strong indicators that magnetic reconnection is occurring near the profile presented in Figure 3.7. In addition, given that the shear flow is a small fraction of the Alfvén velocity, the classical reconnection layer can be expected (*Ma et al.*, 2016) given a sufficient time for the reconnection to evolve. Using the scaling derived in *Cassak and Shay* (2007), the reconnection rate for the given anti-parallel magnetic fields and density is $E \sim 0.1$. The maximum value of $E_{||} = 0.003$ from Figure 3.7 indicates that the reconnection rate is not yet saturated. At $t = 300\ t_A$ the maximum $E_{||} = 0.04$ at this boundary, indicating the reconnection rate is nearly saturated, as expected for driven reconnection.

In the compressible regime for a symmetric configuration the boundary of the outflow is a slow shock such that the expected signature of p and n would be an increase for an observer moving from the inflow to outflow regions (*Petschek*, 1964). This is in agreement with the profile in Figure 3.7. In the outflow region, plasma is heated which can be strongly nonadiabatic for very small plasma beta in the inflow region. One source of nonadiabatic heating is the slow shocks that bound the outflow region in the Petschek reconnection model (*Ma and Otto*, 2014). In ideal MHD the specific entropy is a conserved quantity but local dissipation can provide nonadiabatic heating. For large β nonadiabatic heating is negligible and occurs primarily adiabatically due to compression.

Figure 3.7 shows aspects of the expected changes that would occur for a spacecraft passing through the outflow boundary, but the large computing demands of a 3D grid means reconnection layers in the 3D simulations are inadequately resolved. On simulation spatial scales reconnection is still developing such that the classical layers associated with steady state reconnection are poorly evolved. In order to better understand and characterize the observable signature of reconnection layers, we use a high resolution 2D MHD simulation.

3.5 Observable Signatures of Very Remote Reconnection

The results from the prior section illustrate that reconnection can be expected at strong field-aligned current layers separating flux tubes with different topology and in the 3D simulation it is developing toward fast reconnection rates. Once fast reconnection has been established, it is expected to have plasma jetting away from the parallel electric field region where the

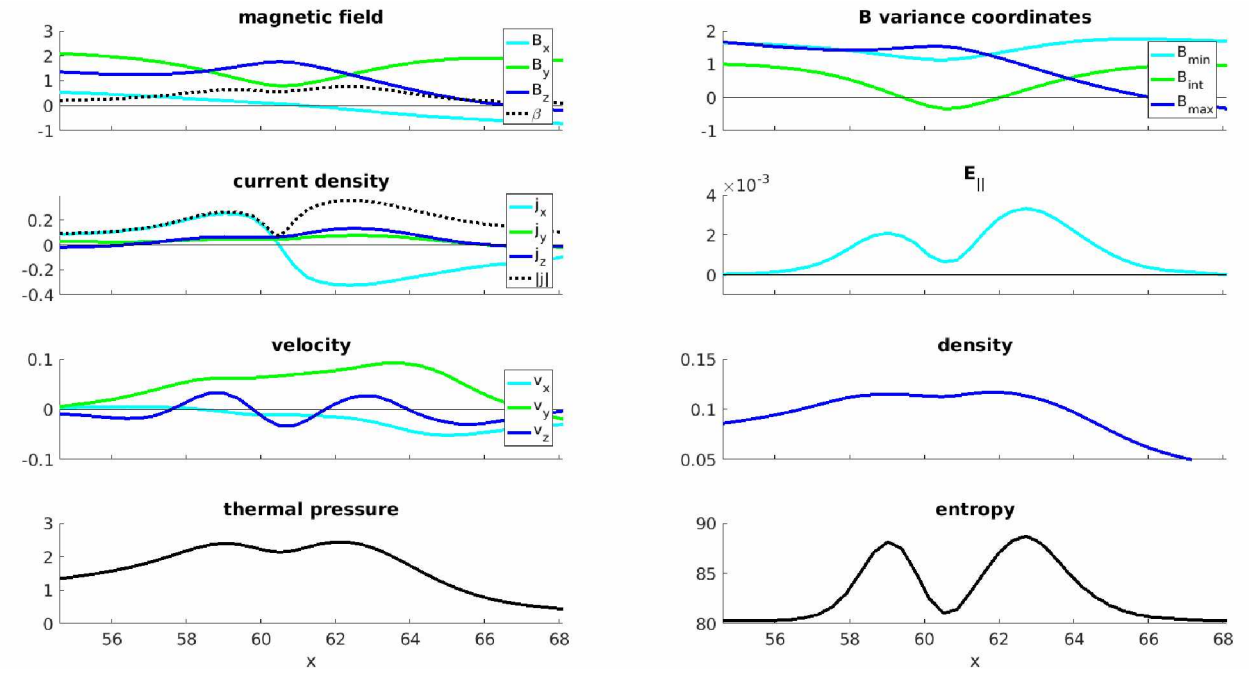

Figure 3.7: Magnetic reconnection developing in the 3D simulation.

frozen-in condition is broken. In order to examine the nature of solar wind current sheets we need to establish properties that we expect to observe as a result of remote reconnection.

For a symmetric configuration without guide field the large scale (MHD) structure is that of *Petschek* (1964) reconnection, where two slow shocks separate the inflow region from the fast jetting outflow region. In a more general case, as illustrated in the 2D simulation example from Figure 3.8, the inflow regions are not symmetric, i.e., the magnetic field magnitude, density, and pressure are not symmetric, and there is a so-called guide field pointing into the (in 2D) invariant direction parallel to the current and perpendicular to the antiparallel magnetic field components. In general, there is also convection tangential to the current layer present in the inflow regions.

There have been extensive studies (*Lin et al.*, 1992; *Lin and Lee*, 1993, 1995; *Biernat et al.*, 1989) on so-called steady state reconnection. The situation represents a Riemann problem, i.e., matching two regions with different magnetic field and plasma properties by a set of MHD waves and discontinuities. Typical properties of these reconnection layers are changes of density, entropy, magnetic field orientation, and velocity across the different MHD discontinuities and shocks. Specifically, large changes of the plasma velocity often satisfy the Walén relation (*Walén*, 1944). This applies to rotational discontinuities and intermediate shocks, but also to strong slow shocks (particularly switch-off slow shocks).

The dominant boundaries of the plasma jet evolve on the ion inertial scale when the inertial scale is larger than the ion gyro-scale ($\beta < 1$), or on the ion gyro-scale when this

is the larger scale ($\beta > 1$). In either case the corresponding changes in velocity and Alfvén speed satisfy approximately the Walén relation (*Walén*, 1944; *Sonnerup et al.*, 1987):

$$\Delta \mathbf{v} = \pm \Delta \mathbf{v_A} \tag{3.1}$$

where $v_{A_j} = B_j \sqrt{\mu_0 \rho}$ for the j^{th} component. A test for the Walén relation must look for point by point correlations between $\Delta \mathbf{v_A}$ and $\Delta \mathbf{v}$ for all three components. In this paper, we use the following methodology. At the i^{th} data point (in either spatial or temporal domain), for each velocity component j, the 4 differences ($[v_{ij} - v_{(i-1)j}]$, $[v_{ij} - v_{(i+1)j}]$, $[v_{ij} - v_{(i-2)j}]$, $[v_{ij} - v_{(i+2)j}]$,) are taken. These 12 changes are then plotted against the corresponding changes in the components of $\mathbf{v_A}$ and a line through the origin is fit to the resulting scatter plot. When the slope m of this line fulfills $1 - \epsilon < m < 1 + \epsilon$ for some small value of ϵ, and the statistical $R^2 > 0.9$, the 5 point interval satisfies the Walén relation. The test then steps to the $(i+1)^{th}$ data point and performs the test again to find layers of arbitrary length that satisfy the relation.

We have applied this method to the 3D solar simulation result in Figure 6. However, it is difficult to identify regions which satisfy the Walén relation, even with a large $\epsilon = 0.3$. This is because early in the simulation the reconnection layers have not fully developed, while later on many photospheric perturbations have propagated into the vicinity of a separatrix. It is also complicated by the superposition of reflected waves from the top and bottom boundaries and additionally the resolution along such a cut is very low. There are < 50 grid points spanning such a 3D cut so a higher resolution and simplified configuration would be necessary to resolve the Alfvénic layers in these simulations.

Figure 3.8 shows a typical result for 2D reconnection with an asymmetry in the magnitude of the antiparallel magnetic field magnitude, thermal pressure, and density. Note that the configuration is mirror symmetric across the plane $y = 0$. The initial configuration has $B_2 = \sqrt{2} B_1$ (where 1 and 2 represent the different sides of the magnetic shear boundary and 1 corresponds to the region $x < 0$) and guide field such that the total rotation of the magnetic field is 120 degrees. Pressure is determined by total pressure balance where the plasma β in the $x < 0$ inflow region is chosen to be 1. In addition we also conducted runs for $\beta = 0.1, 4$, and 10. Density is chosen such that the specific entropy $S = 1$. Note that these choices imply a lower density and thermal pressure on the larger magnetic field side 2 as illustrated in Figure 3.8. Shear flows can also have an effect but this is not considered here, because it would further complicate the situation and the shear flow between flux tubes illustrated in Figure 3.6 is a very small fraction of the local Alfvén velocity.

The 2D MHD simulation solves the same normalized resistive MHD equations for the continuity, momentum, and magnetic field as given in section 2, but the energy equation is

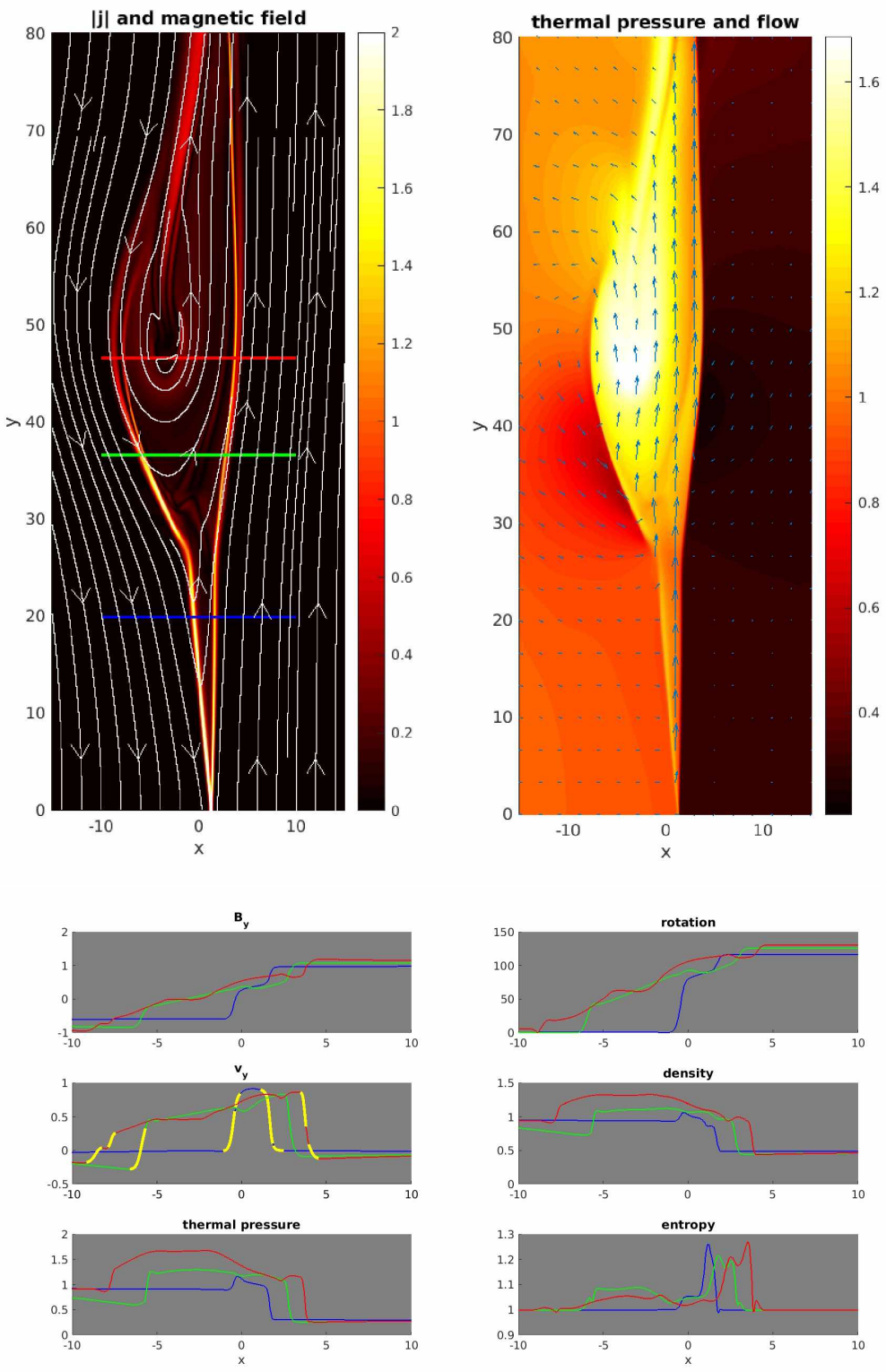

Figure 3.8: Asymmetric 2D magnetic reconnection layer. The three colored lines (blue, green, red) in the top left panel cut through the outflow jet and bulge region. The six panels below give plasma and magnetic field properties as taken along these lines. Yellow highlighting on top of the velocity profiles satisfy the Walén relation.

given by total energy conservation. This is necessary to capture the entropy change across a shock that is especially important in a low β plasma. The simulation encompasses a volume of $15\ell_0 \times 80\ell_0$ in x and y and is resolved with 750×1200 uniformly spaced grid points. A full description of the 2D MHD reconnection simulation and its specifics can be found in *Ma and Otto* (2014). The simulations presented here will be used to guide our analysis of solar wind current sheets observed by the MMS spacecraft.

The two color maps show the magnitude of current density with magnetic field lines (top left) and thermal pressure with velocity arrows (top right). The line plots underneath the color plots show magnetic field, velocity and plasma properties for three cuts through the simulation. It is important to note the aspects that are different or have been ignored in the study of in-situ reconnection signatures for instance at the dayside magnetopause (*Paschmann et al.*, 1979). Traditionally, the argument of Alfvénic boundaries has been applied to the steady state outflow region between $y = 0$ and $y \sim 27$. However, an interesting feature of the reconnection outflow visible in Figure 3.8 is the bulge that forms where the jet interacts with ambient plasma. The colormap of current density shows that the outflow jet and and regions of the bulge are bounded by a thin layer of electric current. The thermal pressure colormap shows a larger value in the outflow and bulge than the surroundings, so it is clear that the magnetic field strength must be weaker in the outflow in order to maintain total pressure balance.

Two example profiles (red and green lines) cut through the bulge in the top left panel of Figure 3.8 and another (blue) through the outflow jet. The profiles for magnetic field and plasma properties along these three lines (with corresponding colors) are shown below the colormaps. The yellow highlighting on the 1D profiles of v_y shows where the Walén relation is satisfied at the outflow boundaries of the 2D simulation results, using a value of $\epsilon = 0.1$. Only the y component for the magnetic field, velocity, and $\mathbf{v_A}$ are shown but the test for the Walén relation still takes into account all components. These results indicate that a spacecraft does not need to encounter the steady jet in order to observe layers which satisfy the Walén relation. In principle this was expected since several studies have illustrated that flux transfer event (FTE) signatures are often Alfvénic and they can be caused by the bulge moving past (*Lockwood and Hapgood*, 1998).

Because of the much smaller scale size, magnetopause observations of reconnection almost always go through the entire boundary layer. However, the extent of the steady outflow and bulge regions for the type of large scale and remote reconnection considered here are so large that except for rare circumstances, we cannot expect to encounter or identify the matching boundary of any reconnection exhaust in the solar wind. This is a limitation of the MMS data set because the burst mode observations are a few minutes at most. If reconnection has

operated for 1 day the total distance of the leading edge is $\sim 10^7$ km distant and typical sizes for the width are 10^5 to 10^6 km. Therefore we need to consider or are restricted to properties of only one side of the boundaries shown in Figure 3.8. The particular disadvantage is that we do not have any measure of both sides of the inflow region, particularly the total rotation of the magnetic field. Even though the example shows that the Walén relation may hold at both boundaries, it is expected to apply only to one of the boundaries in cases of strong asymmetries or may be rather difficult to identify for both boundaries. For instance, at the magnetopause it is always the strong rotation of the magnetic field that is being identified as Alfvénic (*Paschmann et al.*, 1979) while the inner edge of the low latitude boundary layer has not been demosntrated to be Alfvénic.

The top right panel of 1D profiles in Figure 3.8 gives the rotation of the magnetic field as compared to the boundary value at $x = -15$. The rotation at the edge of the outflow jet can be ~ 40 degrees or ~ 80 degrees depending which side is crossed. The rotation is larger for the edge of the outflow which requires a larger acceleration, i.e. the side with smaller magnetic field, larger density, or shear flow opposing the reconnection flow (*La Belle-Hamer et al.*, 1994). When passing through the boundary of the bulge in different regions, the rotation is always < 60 degrees and often ~ 40 degrees or less. Note that the angle in consideration is only that which occurs in the vicinity of one side of the reconnection outflow boundary and that the example in Figure 3.8 uses a relatively large total magnetic shear of 120 degrees. These angles depend on the magnitude of the guide field and asymmetries of the reconnection layer. Figure 3.8 also indicates that increases in density and thermal pressure would be observed for a spacecraft moving from inflow to outflow, regardless of which edge of the jet or bulge is crossed. The profiles of specific entropy quantify nonadiabatic heating for this case where $\beta = 1$, showing a slight entropy enhancement in the outflow and bulge. More significant nonadiabatic heating is present for cases where $\beta << 1$. For instance, the largest peaks in the entropy for this example are 20% above the background, while a symmetric case with $\beta = 0.1$ has entropy in the outflow that is twice the background. Cases with $\beta = 4$ and 10 show only a few % change in plasma density and entropy.

Note that a high plasma β makes reconnection more unlikely (diamagnetic drift stabilization (*Swisdak et al.*, 2003)) but this applies only to its origin at the "X" line. This may be indicative that reconnection signatures observed at 1 AU may have been caused by reconnection with a site that was originally much closer to the sun or actually in the solar corona where the plasma β is expected to be $<< 1$. When the reconnection boundaries are swept outward, plasma β increases (generally $\beta \geq 1$ at 1 AU, see Figure 3.11(c)) which does not change the presence of that boundary but will change local plasma properties and its

character. For low plasma β the outflow boundary is characterized by ion inertial (Hall) physics and for larger plasma β ion gyroviscous effects dominate.

In addition to the specific changes in plasma properties that have been discussed and the Walén relation, another identifiable signature for a reconnection layer is a small value of B_n (*Sonnerup*, 1979; *Mozer and Retinò*, 2007). Ideally, this is a measure of the reconnection rate and a normalized value $B_n \sim 0.1$ has been found in studies of magnetopause reconnection (*Mozer and Retinò*, 2007). Since we can not find the magnitude of the antiparallel components with only one edge of the outflow region, the normalization is taken as $B_n/|B|$, where $|B|$ is from the side observed with larger magnetic field magnitude. With large guide fields (small magnetic shear angles) it is expected that this normalization underestimates the true reconnection rate because $|B|$ could easily be much larger than the true antiparallel field component. A small B_n is also subject to large uncertainty caused by small errors in the boundary normal. Therefore B_n may not only be a poor measure of the reconnection rate but may not be suitable to distinguish rotational discontinuities from tangential discontinuities.

3.6 Current Sheets in the Solar Wind

During its many brief excursions into the solar wind, MMS finds a large number of current sheets separating distinct plasmas and magnetic fields, similar to the solar wind structure reported by Advanced Composition Explorer (ACE) (*Borovsky*, 2008). A long standing question regarding such current sheets is their classification as tangential discontinuities or rotational discontinuities (see *Neugebauer and Giacalone* (2010)). It is possible that reconnection operating at separatrices in the corona and underlying magnetic carpet can produce signatures of magnetic reconnection that would be observable as boundary structure in the solar wind. If there is no signature of reconnection then the current sheets could be tangential discontinuities or the structure of Alfvénic turbulence.

3.6.1 The Journey to 1 AU

A consistent signature to support the observation of remote reconnection must consider the transit time from the sun to 1 AU. An important property of this transit is the change in plasma β that results as the thermal pressure and magnetic field strength both decrease with heliocentric distance. The solar corona has values of $\beta \sim 10^{-3}$ or smaller (*Iwai et al.*, 2014) while the solar wind at 1 AU has a distribution peaked at $\beta = 1$ (*Mullan and Smith*, 2006). To gain qualitative insight into how the discontinuities at the edge of the outflow and bulge might be modified during this transit, we compare the 2D reconnection simulation for a $\beta = 4$, $\beta = 1$, and $\beta = 0.1$ plasma in Figure 3.9.

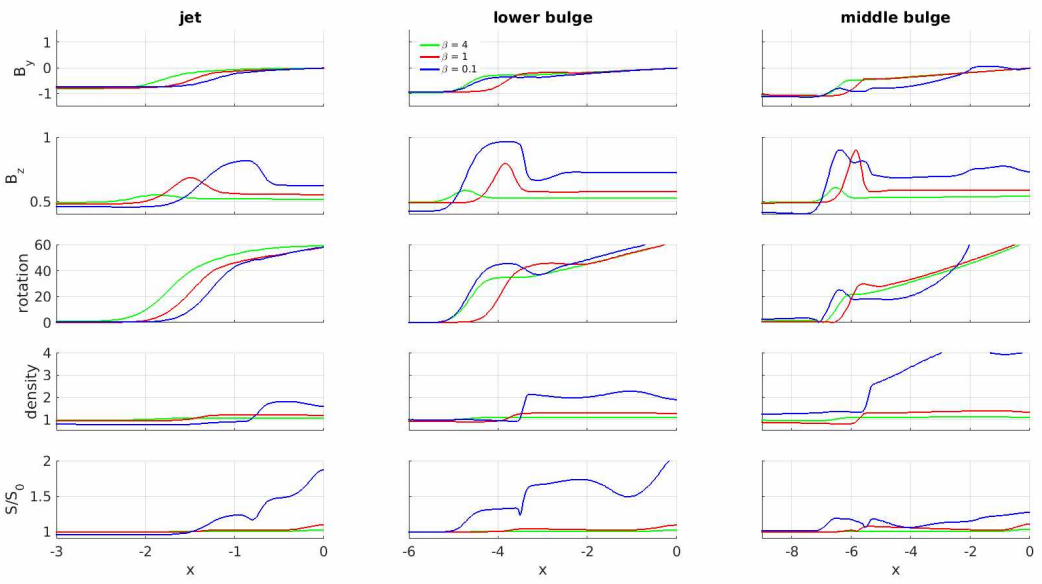

Figure 3.9: Magnetic field, density, and specific entropy changes at the outflow jet and bulge boundaries for different values of β.

The one-dimensional profiles in Figure 3.9 are cuts through a 2D simulation similar to Figure 3.8, but for a symmetric reconnection configuration. Three simulation results with nonzero guide field and different values of β are given by green ($\beta = 4$), red ($\beta = 1$), and blue ($\beta = 0.1$) lines. Only one side of the outflow/bulge is shown due to the symmetry. The three columns correspond to cuts through the outflow jet (left), lower portion of the bulge (middle), and thickest portion of the bulge (right), similar to the locations of the three colored profiles in the top left panel of Figure 3.8. The first and second rows give B_y and the out-of-plane component B_z, respectively, while the third row shows the rotation of the magnetic field with respect to the boundary value at $x = -15$. The fourth and fifth rows give the density and specific entropy normalized to the background value. As before, all of these boundaries satisfy the conditions for a slow or intermediate shock.

There are a number of important aspects to note in Figure 3.9. From the top row, it is clear that the anti-parallel component B_y changes more at the middle bulge for $\beta \geq 1$ plasma compared to the $\beta = 0.1$ plasma. The second row shows that the out-of-plane component B_z has a larger enhancement for smaller value of β. At the jet and lower bulge boundaries the B_z enhancement can be significantly larger for $\beta = 0.1$ compared to the $\beta \geq 1$ cases, but in the middle bulge the magnitude of the B_z enhancements for $\beta = 0.1$ and $\beta = 1$ are similar. In addition to a larger magnitude of B_z bounding the jet and bulge for $\beta = 0.1$ the enhancement is also wider for all three boundaries shown. Note, these would not be observable effects in this study, since the magnitude of antiparallel components can not be

determined.

A measurable quantity is given in the third row, which shows the rotation in the magnetic field as compared to the boundary value at $x = -15$. The rotation at the edge of the outflow jet appears very similar for the three different values of β. For the boundaries of the bulge, the $\beta = 4$ case has the smallest rotation, while they are similar for the $\beta = 0.1$ and $\beta = 1$ cases. By comparing rows 2 and 4, it is clear that the enhancement in B_z occurs over a wider region than the density enhancement for the $\beta = 0.1$ case, while these regions overlap essentially everywhere for the $\beta = 4$ case. For the $\beta = 0.1$ plasma there is a slow shock and a rotational discontinuity, while these are overlapping for $\beta \geq 1$. The density enhancement is only a few % for the $\beta = 4$ case while it can double for $\beta = 0.1$. From the final row, little to no nonadiabatic heating occurs for $\beta \geq 1$, as expected, but the $\beta = 0.1$ case can have significant entropy enhancement. The profiles cutting through the jet and lower bulge region show two distinct peaks, the first which occurs in the region where the density has yet to increase, while a second enhancement occurs where the density is enhanced. At the widest part of the bulge, the nonadiabatic heating is essentially zero. We remind the reader that for these simulation results, the changes discussed occur only in the vicinity of the current layer bounding the jet and bulge. This is in the spirit of the MMS data analysis, where only one side of the outflow is likely to be encountered.

These results suggest that the shear angle across a reconnection outflow boundary can decrease as it propagates from a region of $\beta < 1$ to $\beta > 1$, an effect that is particularly noticeable at the edges of the bulge. Shear angles of $\sim 20 - 45$ degrees can occur at the bulge boundary and $\sim 45 - 60$ degrees for the outflow jet although the total asymptotic field rotation is 120 degrees. Given the likelihood that the general configuration is asymmetric, it is important to note these angles are larger than the corresponding rotation on the other edge of the outflow or bulge (see Figure 3.8). In addition, these results apply for a given value of the guide field, which in reality can vary from small to large compared to the antiparallel components.

There is an additional effect of the propagation from the sun to 1 AU which will work against the decreasing shear angle caused by the increasing plasma β. Given an isotropically expanding field-aligned current layer, the decrease of magnetic field strength with heliocentric distance means the magnetic shear will increase across a current layer advecting outwards from the sun. This is in agreement with the argument by *Borovsky* (2010) which considered a passive mapping of flux tube misalignments at the top of the corona.

In summary, signatures of one boundary of the reconnection outflow are only expected to show the following properties: It is not possible to distinguish between bulge and steady state outflow. $\Delta|B|$ is small unless the asymptotic field is strongly antiparallel. The local

rotation of the magnetic field is typically smaller than half of the total shear angle of the asymptotic field, unless there is significant asymmetry and the encounter is at the steady fast outflow jet boundary. $Bn/|B|$ is small and reaches the value of about 0.1 only for largely antiparallel asymptotic field (shear ¿120 degrees). Plasma density and entropy changes are small (few %) for plasma $\beta > 1$. More than 50% of the boundaries should show Alfvénic character with a value of close to 100% for symmetric inflow regions and approaching 50% for strongly asymmetric reconnection.

3.6.2 Data Set

The MMS spacecraft constellation is primarily intended to study the magnetopause boundary and dynamical magnetotail processes in the terrestrial magnetosphere. In spite of this, it is a valuable observatory for the solar wind flow since its orbit crosses the magnetopause and bow shock many times. We will utilize a pair of instruments on board MMS to probe solar wind current sheets. Namely, the Flux-Gate Magnetometer (FGM) gives vector magnetic fields and the Fast Plasma Investigation (FPI) allows the determination of vector plasma flows, number density, and thermal pressure.

The data set consists of 278 MMS burst mode intervals. The list of dates for these intervals is given in the supplemental material. For each interval we use the Level-2 FGM and FPI data from all spacecraft reporting during that time. The observing times for these intervals are between 20 seconds and 4 minutes. Each burst mode observing interval is labeled as containing a "solar wind current sheet" by the MMS Science Data Center mission events list (https://lasp.colorado.edu/mms/sdc/public/about/events/#/). An example solar wind current sheet is given in Figure 3.10 in GSE coordinates. The feature that defines the current sheet is a jump (rotation) in one or more components of the magnetic field. The example magnetic field trace given in the top panel shows a large jump in the B_z component coincident with small changes in the B_x and B_y components. For this event plasma $\beta = 2$ which is a typical value for many of the current sheets in this data set.

While most of the chosen burst mode intervals contain a single current sheet event which is easily identifiable, we have identified 381 current sheet crossing events so that a few of the intervals have more than 1 event. For the sake of reproducibility, the following describes a semi-automated search algorithm applied to the magnetic field time series. The algorithm begins with a small window length, taking averages of each magnetic field component over this length either side of each point in the time series. The difference between the averages is added up for increasing window lengths and this gives a function which peaks where the time series has large rotations in the magnetic field. Two additional criterion are applied for event selection. First, each current sheet must have a magnetic field jump $\sqrt{\Delta B_x^2 + \Delta B_y^2 + \Delta B_z^2} >$

1 nT. Second, a hand identification test eliminates events which are not isolated from other structures in the time series.

Figure 3.11(a) shows the location in GSE coordinates for each event projected into the $x - y$ plane. The dashed lines give reference locations for Earth's magnetopause boundary with subsolar distances of 7, 10, and 13 R_{earth}. For these events the measured bulk velocity is always $v > 300$ km/s, providing confidence that each event is in the unshocked solar wind. It is not certain whether any of the events are effected by foreshock perturbations but the requirement of isolated events is an attempt to alleviate such contamination. All observations were taken between January 2017 and April 2018, occurring near a solar minimum where solar wind structure would be expected to be at its least variable. This is not a comprehensive list of solar wind current sheets observed in this time interval, so the number included in this study is not indicative of their abundance.

The group of current sheet crossings has the distribution of magnetic shear angles as given in Figure 3.11(b). More than 3/4 of the events rotate the magnetic field by 60 degrees or less. This is consistent with the simulation results from Sections 5 and 6.1 for a reconnection outflow with nonzero guide field. There are also 30 events with a rotation of > 90 degrees. Such a rotation must result from the increase of magnetic shear that occurs on a field-aligned current layer in the solar wind as mentioned at the end of last section, indicating this effect may can be more prominent than the increase of plasma β. The distribution of magnetic shear angles has a flat distribution from 10-50 degrees, which is different from the distribution in Figure 2 of *Borovsky* (2008). This is likely because we have required current sheet events to be isolated whereas *Borovsky* (2008) performs a statistical analysis for each 128 second interval of ACE data.

Another characteristic of these solar wind current sheets is the plasma β as given in Figure 3.11(c). Note that the thermal pressure used to calculate β is modified to enforce total pressure balance as detailed in section 6.4. A large number of the events have $\beta > 1$. It is important to note that FPI pressures comes with greater uncertainty than the velocity, as found by *Bandyopadhyay et al.* (2018) who compared the plasma β to Wind spacecraft observations. They found a factor ~ 3 difference which would still indicate that most of our events have $\beta > 1$, however also the β here is calculated using both electron and ion pressures, which is not the case for most other studies where only the proton β is used. Reconnection can be suppressed by diamagnetic drift stabilization for large values of β but only if the reconnection site is in a high β region which may not be the case if it occurred near the sun.

Using a continuity equation for the radial solar wind flow along with the assumption of a constant specific entropy, a scaling $\sqrt{\beta} \propto r^{1/3}/v_r^{\gamma/2}$ can be derived for the plasma β as a

function of radial distance from the sun. Mapping the average value $\beta \sim 5$ from 1 AU back to 1 R_{sun} gives $\beta \sim 0.1$, as can be expected in some regions of the solar corona (*Iwai et al.*, 2014). Note that the constant entropy assumption ignores nonadiabatic heating so that the actual mapping can be $\beta < 0.1$. Since solar wind statistics indicate the distribution for plasma β is peaked at $\beta = 1$ (*Mullan and Smith*, 2006), it is also interesting that the average value for β at these events is ~ 5, which may indicate that nonadiabatic heating is occurring preferentially at these boundaries compared to the background solar wind, consistent with the reconnection picture for their origin. Because the ratio of ion gyroradius r_{gi} to ion inertial length λ_i is equal to $r_{gi}/\lambda_i = \sqrt{\beta}$, ion gyroviscous effect dominate over Hall physics for most of these boundaries.

3.6.3 Data Processing and Analysis Methods

Using this data set, we will classify solar wind current sheets according to changes in the average properties either side of the magnetic field rotation, and also by testing the Walén relation as given in Equation 3.1. We will also test the magnitude of magnetic field normal to the boundary (B_n) which can be an indicator of whether the boundary is open such that reconnection has acted or separates plasma with a tangential discontinuity. For the purposes of this investivation, we require the magnetic field, thermal pressure, number density, and plasma velocity.

The three components of magnetic field in GSE coordinates come from the FGM instrument which has a measurement frequency of 128 s^{-1}. For a given event we take all available spacecraft and interpolate the magnetic field measurements to the center of the configuration. The very small relative distance between the spacecraft means that this interpolation is an effective smoothing over a few 10s of km. One can see how close the spacecraft are in the top panel of Figure 3.10. The magnetic field trace is given from all four of the spacecraft for this time interval showing that they overlap remarkably well.

For the plasma velocity, we use the ion moments calculated from the FPI energy spectrograms. The measurement frequency for the ion moments is ~ 7 s^{-1}. A considerable portion of the uncertainty in this data analysis is due to the fact that the FPI instrument is optimized for magnetospheric particle populations. This causes large amplitude oscillations in the ion moments which occur as discrete spikes in frequency space. This instrumental effect, described in section 4 of the MMS FPI Data Users Guide, is removed using an adapted version of the method by *Bandyopadhyay et al.* (2018) which applies a Hampel filter to the Fourier transformed data. This filter is applied to the ion velocity and then a low pass filter produces the final time series. The Hampel filtering used here preserves the low frequency components of the spectrum since they correspond to the structure of current sheet crossings.

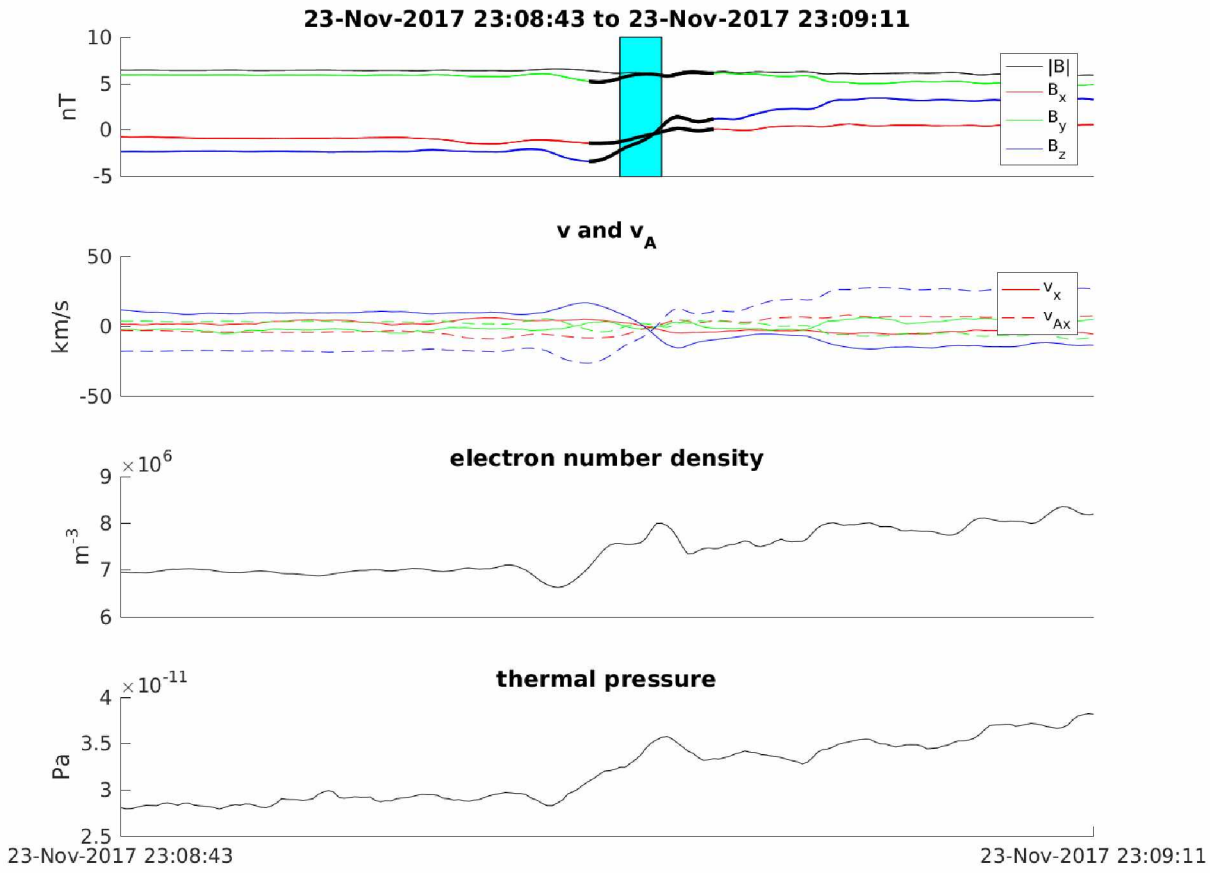

Figure 3.10: Magnetic field (top), ion velocity $\mathbf{v}$ and Alfvén velocity $\mathbf{v}_A = \frac{\mathbf{B}}{\sqrt{\mu_0 \rho}}$ (top-middle), electron number density (bottom-middle), and scalar thermal pressure (bottom) for ~ 30 seconds solar wind observations by MMS. The interval traced in thick black in the top panel is identified as a current sheet crossing. The cyan highlighting gives the interval that satisfies the Walén relation for $\epsilon = 0.2$. The mean value has been subtracted from the plasma velocity and the colors for the velocities correspond to the same component as the legend given in the top plot.

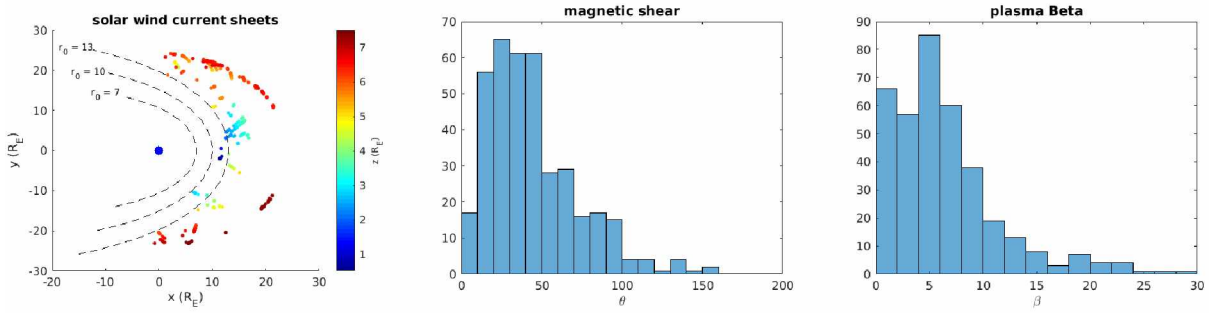

Figure 3.11: Location of events in GSE coordinates around Earth's magnetopause (a). Histogram of magnetic shear angle across the current layers (b). Histogram for average β at each current sheet (c).

For the plasma density, we use the electron moments under the assumption of quasi-neutrality. The measured electron number density n_e does not suffer from large amplitude fluctuations as the ion number density does. The electrons in the solar wind are more isotropic than the ions and therefore FPI can give a more reliable measurement. The MMS FPI Data Users Guide recommends to not use the electron density data if Quality Flag bit 7 is 1; all chosen intervals fulfill this requirement. These moments have a time resolution of ~ 33 s^{-1} and a low pass filter is applied to smooth the time series but there is no application of the Hampel filter.

The scalar thermal pressure is a sum of electron and ion scalar pressures $p = p_e + p_i$. The p_i is treated with a Hampel filter and low pass filter while p_e only requires the low pass filter. With an uncertainty of 5%, 226 out of the total 381 events satisfy total pressure balance (thermal + magnetic) using a finite average over the data observed immediately before and after the current sheet crossing. Given the standard deviation of the thermal pressure averaging, a larger fraction 293 out of the 381 events are consistent with a total pressure balanced structure. This aspect of the data analysis deserves careful attention, and will be discussed in relation to Figure 3.15. Non-pressure balanced structures must be waves or transient perturbations to the plasma, which are not the focus of this study.

Ion velocity, p_i, p_e, and n_e are interpolated to the center of the MMS configuration using the measurements from all available spacecraft. Additionally, all data are interpolated to the same time stamps as the ion moments, since these observations have the lowest measurement frequency. In the second panel of Figure 3.10, the three solid lines give components of velocity in GSE coordinates having been processed with the filters and interpolated between spacecraft. The last two panels show the variations in number density and scalar thermal pressure for this time interval also after the filtering and interpolation between spacecraft.

In Figure 3.10, the portion of the magnetic field time series highlighted in black defines one of the many current sheets selected for this study. The first part of the following section will analyze intervals such as these and determine a sub-interval over which the Walén relation is satisfied using the test described in Section 4. In Figure 3.10, this subinterval is highlighted in cyan. The example in Figure 3.10 also has increases in both number density and thermal pressure (and decrease in $|B|$) across the current sheet which is consistent with the expected signature crossing a reconnection outflow boundary as described in Section 5. To calculate the changes in these quantities across the current sheets we take average values from either side of the transition.

The calculation of the boundary normal direction is important in order to determine B_n and also to approximate the appropriate scale length for these current sheets. The minimum variance direction is calculated using a single spacecraft and this direction is compared with the result of the multi-spacecraft timing method (*Paschmann and Schwartz*, 2000). A quality control factor for the minimum variance direction is the ratio of intermediate to minimum eigenvalues of the variance matrix. To assure an accurate boundary normal, the direction is accepted only if the eigenvalue ratio is $\lambda_1/\lambda_2 > 5$ and agrees with the multi-spacecraft timing method to within 45 degrees. For better statistics we also take the ratio $\lambda_1/\lambda_2 > 10$ alone as a sufficient condition (*Neugebauer*, 2006). The value for B_n that is found at suspected reconnection outflows can not be greater than implied by the appropriately scaled Petschek rate, but the effect of in-transit evolution on this property is uncertain. If reconnection outflow jets propagate into a region with very different plasma conditions, this assumption for B_n may be violated.

3.6.4 Results

The Walén relation test as applied to the 2D simulations in Section 5 used data separated in the spatial domain. The MMS data in this section gives a time series with a time separation of 150 ms between measurements. The minimum number of data points used to satisfy the Walén relation is 5 which gives a minimum resolvable layer width of 240 km for a 400 km/s solar wind velocity. Additionally, we choose $\epsilon = 0.2$ as the threshold for these tests relaxing the requirements compared to $\epsilon = 0.1$ used for the simulations. It is important to note that the test for an interval satisfying the Walén relation often finds more than one set of disconnected data points within the layer with slope ~ 1. When this is the case we choose whichever interval has a larger rotation in the magnetic field. The mass density used to calculate the Alfvén velocity includes the alpha-particle contribution of the solar wind.

Figure 3.12 gives the result of the Walén relation analysis on the set of current sheet crossings. This shows 184 current sheet crossing events which contain a layer satisfying

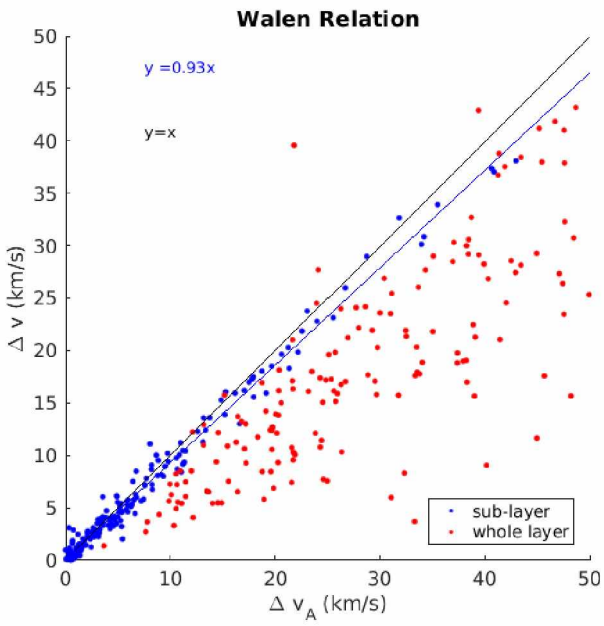

Figure 3.12: Solar wind current sheets containing a layer that satisfies the Walén relation. Blue points give Δv_A and Δv across the layer satisfying the Walén relation for the maximally varying component. The same component of Δv_A and corresponding Δv across each current sheet is given in red.

the Walén relation. The blue points give the changes in velocity Δv and Alfvén velocity Δv_A across only the subinterval of the current sheet which satisfies the Walén relation. The red points give Δv and Δv_A across the whole current sheet event. These points only give the maximum variance component of the corresponding quantities. However, the test as described in Section 4 assures that the Walén relation is satisfied for all components. As expected, the red points do not give a slope near unity since only some portion of the current sheet will satisfy the Walén relation. The blue points for the Alfvénic layers fit well to a line through the origin with slope 0.93. A slope of ~ 0.9 would be expected for slow shocks while a slope of 1 would correspond to switch-off or intermediate shocks. A few of the blue points lie far from $y = x$ which can occur when the maximum variance component is not so dominant and the intermediate and/or minimum components satisfy the Walén relation accurately. This may also be demonstrating a known source of error, since the instrumental uncertainty for solar wind FPI moments is largest in the x and y components and smallest for the z component (see MMS FPI Data Users Guide section 4).

Figure 3.13 shows some histogrammed properties for a subset of these 184 current sheet events with a layer satisfying the Walén relation. The boundary normal direction can be obtained for 74/184 of these events using the requirements for an acceptable normal mentioned above. Using the measured solar wind velocity, time for MMS to traverse the layer,

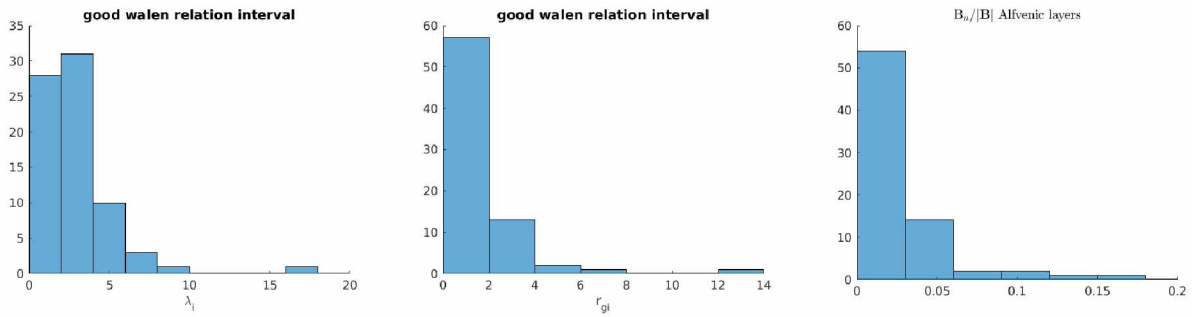

(a) (b) (c)

Figure 3.13: Width of the layer within the current sheet that satisfies the Walén relation in units of ion inertial lengths λ_i (a) and ion gyroradii r_{gi} (b). Normalized value of B_n for current sheets with layer that satisfies the Walén relation (c). Only cases with acceptable boundary normal are given.

and boundary normal direction, a width can be calculated. Panel (a) shows the widths of the observed Alfvénic layers in units of the ion inertial length λ_i, while Panel (b) is in units of the ion gyroradius r_{gi}. Almost half of these layers are thinner than 1 r_{gi}. These widths suggest ion kinetic physics is more important than the ion inertial scale for the specific structure within a layer satisfying the Walén relation ($\beta > 1$). For the outflow boundary thin current sheets are expected because they represent (intermediate or slow) shocks. These would always develop on the scale where dissipation or two fluid effects modulate the boundary, i.e, on the ion inertial or gyro-scale, whichever is larger.

Panel (c) of Figure 3.13 gives the normalized magnitude of B_n for the subset of 74 events satisfying the Walén relation. The magnitude has been normalized to the strength of the magnetic field on the the side of the current sheet with larger magnetic pressure. Using a threshold of $B_n/|B| < 0.2$, all events in this subset are consistent with a reconnection outflow boundary. Again we note that this choice of normalization tends to underestimate the actual reconnection rate because the guide field is included in $|B|$. Very small values of $B_n/|B|$ could be tangential discontinuities since the uncertainty in the boundary normal direction means a value $B_n = 0$ is unlikely to be found. However, a tangential discontinuity structure is unlikely to satisfy the Walén relation. Given the fraction 184/381, an estimate for the percentage of current sheets that are the boundary of a reconnection jet is 48%.

Signatures of magnetic reconnection discussed in Sections 5 and 6.1 indicate thermal pressure and density will both increase when traversing the edge of an outflow region, while the magnetic field strength decreases. Figure 3.14 provides an estimate for the percentage of current sheets that are outflow boundaries using the fractional changes in these quantities. Only events consistent with a total pressure balanced structure are included, so that anti-

correlated changes of thermal pressure and magnetic field strength are implied for the subset of 346 events in Figure 3.14. The changes in number density are given so that they are always positive and correspondingly the changes in $|B|$ are calculated by subtracting the value from the side with larger density from that on the side with smaller density.

The colors in Figure 3.14 indicate whether Δn and $\Delta|B|$ changed in a manner consistent with (green) or not consistent with (red) MMS traversing the edge of a reconnection outflow. Note that the quantities on both axes have been normalized to the background, so that the values given are fractional changes. The black points indicate events which have large enough error bars (calculated from the standard deviation of the averaging interval) such that the test is inconclusive, which applies to many events with relatively small Δn or $\Delta|B|$. The fraction of consistent points is 170/346 events while only 14/346 are inconsistent, with the remaining 162 events being inconclusive. Furthermore, 87/170 consistent events pass the test for the Walén relation. Given that all events satisfying the Walén relation have $B_n/|B| < 0.2$, the fraction ([# good Walén relation]/[unambiguous changes]) = 87/184 = 47% gives an estimate for the percentage of current sheets which are consistent with the structure of outflow boundaries based on three separate metrics. Note that for large plasma β changes in Δn and $\Delta|B|$ are expected to be very small and comparable to the standard deviation, such that a large fraction of inconclusive events is to be expected for large plasma β reconnection boundaries.

A current sheet which has anti-correlated Δn and $\Delta|B|$ but does not satisfy the Walén relation can not be ruled out as a reconnection outflow boundary, given that only one edge of the outflow will satisfy the Walén relation for a sufficiently asymmetric configuration. Current sheets satisfying the Walén relation but not having anti-correlated Δn and $\Delta|B|$ are likely Alfvénic fluctuations associated with turbulence (*Gosling et al.*, 2011).

As mentioned earlier, the requirement of total pressure balance is used to filter for potentially erroneous thermal pressure measurements caused by the FPI instrument. A lack of total pressure balance may be the result of inaccurate thermal pressure measurement, but could also be artificial due to taking too long of a window to find the average quantities either side of the current sheet. Changes in the specific entropy, which will be quantified in Figure 3.15, require an accurate measure of the thermal pressure. Events which are in total pressure balance with an uncertainty of 5% are left unmodified, while we can attempt to correct the instrumental deficiencies for those events which do not meet this criteria.

The corrected thermal pressures are obtained as follows. First, only events where the sign of changes in magnetic pressure and thermal pressure are consistent with a total pressure balanced structure can be modified. If the data indicates that magnetic pressure and thermal pressure both increase across a current sheet, no attempt is made to correct the thermal

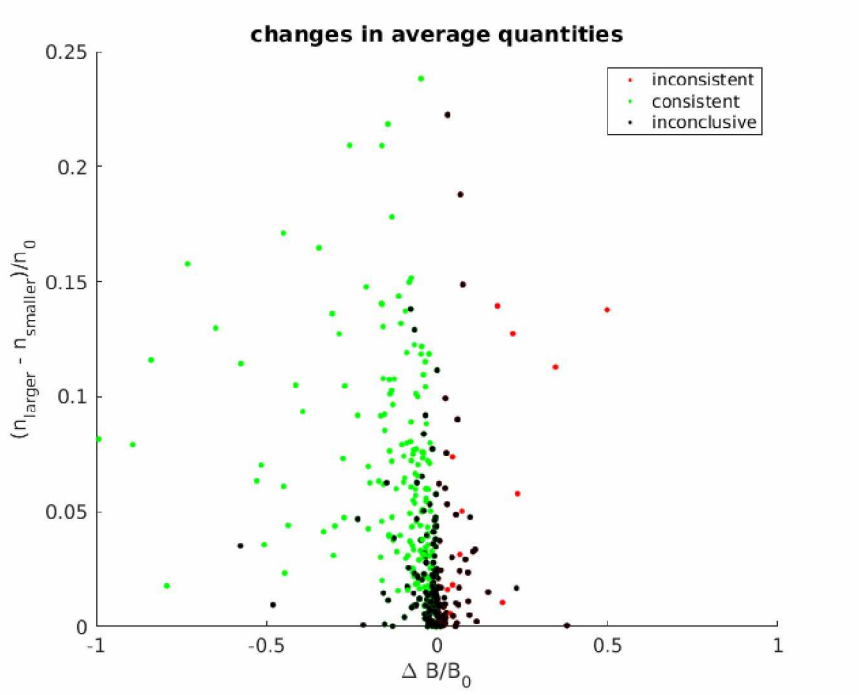

(a)

Figure 3.14: Fractional changes in number density and magnetic field strength across solar wind current sheets. The colors indicate whether Δn and $\Delta|B|$ are consistent (green) or not consistent (red) with the reconnection picture. Black points have error bars which render the analysis inconclusive.

pressure and these events are not included in this portion of the analysis. Such non-pressure balanced structure must be transient waves or due to instrumental uncertainty. For events where pressure balance can be obtained, the lack of total pressure balance is quantified by the inequality

$$p_1 + \frac{B_1^2}{2\mu_0} \neq p_2 + \frac{B_2^2}{2\mu_0}$$

so we solve for a constant c such that

$$(1+c)p_1 + \frac{B_1^2}{2\mu_0} = (1+c)p_2 + \frac{B_2^2}{2\mu_0}$$

where $B_{1,2}^2/2\mu_0(p_{1,2})$ is the magnetic(thermal) pressure on sides $1, 2$ of the current sheet.

Figure 3.15 quantifies the fractional changes in number density and specific entropy observed at these current sheets as a function of plasma β. For the 346 events where total pressure balance can be satisfied, Panel (a) shows the fractional change in number density $\Delta n/n_0$ plotted against β at each current sheet crossing. Panel (b) gives fractional changes in specific entropy $\Delta S/S_0$ plotted against β at each current sheet crossing. The red trend

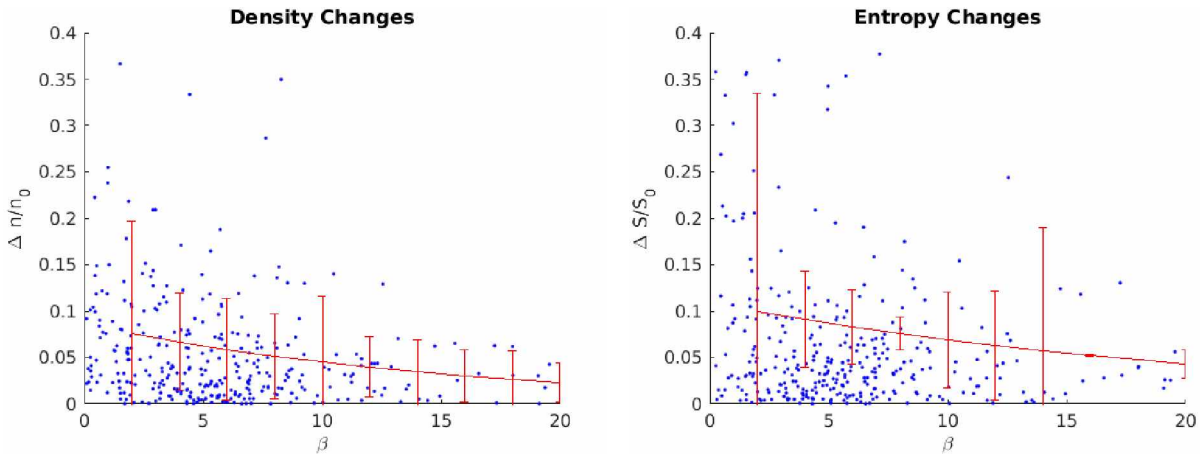

Figure 3.15: Value of β vs. fractional change in number density (a) and specific entropy (b) across current sheet events. The red line is a fit to the mean of bins of width 2 along the β axis and the error bars are given by the standard deviation in each bin.

lines are a fit to the mean of the data for a bin width of 2 along the β axis and the error bars give the standard deviation for each bin. This shows that larger changes in number density and entropy are more likely to occur for a smaller value of β, which is consistent with the reconnection picture for the origin of at least some of these boundaries. Since $\beta > 1$ for most of these events, it is not surprising that large changes in the specific entropy are rare. The simulation results in Figure 3.8 for $\beta = 1$ have a fractional entropy change of 5-20% and this decreases rapidly for larger β.

To summarize results of the MMS data analysis, 48% of all current sheets satisfy the Walén relation. Most events of this subset, which have a sufficiently reliable boundary normal, represent thin (ion gyro scale) boundaries with small B_n consistent with a reconnection outflow boundary. From all boundaries which have reliable changes of Δn and $\Delta|B|$, 170 events have changes consistent with a reconnection layer boundary and only 14 are inconsistent. A large number of inconclusive events either based on the reliability of B_n or changes of Δn vs $\Delta|B|$ are expected because of large relative errors associated with the determination of an accurate normal or with the rather small changes in plasma density and pressure. The overall change of Δn and ΔS is consistent with the expected decrease of these properties with increasing plasma β. Current sheets that do not satisfy the relatively strict conditions for the Walén relation cannot be ruled out as reconnection layer boundaries because (1) not all such boundaries satisfy the Walén relation, and (2) ion kinetics, ion inertial effects, plasma anisotropy, and other plasma physics can cause slopes in the Walén relation test outside the values accepted in our analysis.

3.7 Conclusions

The 3D simulation results from Section 3 apply to a model for the coronal magnetic field which neglects a few important physical aspects. The emergence and cancellation of flux is not accounted for and this can reorganize the topology of the magnetic carpet (*Archontis*, 2008). Null points in the corona are not necessarily a permanent feature (*Priest et al.*, 1996; *Murphy et al.*, 2015) and therefore separatrix boundaries change as the topology changes. In addition, the flow pattern has been simplified from the more realistic profile used for the simulations in *Burkholder et al.* (2018). The main contribution of including smaller scale convection is to introduce Alfvén waves into the system that carry perpendicular or field-aligned currents. However, the simulations by *Burkholder et al.* (2018) also demonstrated that while these currents are present, their magnitude is very small compared to the current along topological boundaries. Furthermore these currents are transient and changing as Alfvén wave sources change.

Regarding magnetic reconnection between flux tubes in the solar magnetic carpet, and the observable signatures of reconnection in the solar wind:

Magnetic reconnection acts on the boundaries between flux tubes since these boundaries are defined by a magnetic separatrix layer that is the preferred location for intense electric current. Open flux tubes in the corona are changing their connection at these boundaries but reconnection acts only in a thin layer. The obvious consequence of magnetic reconnection is that mixing occurs at these boundaries. At ∼500 minutes of physical time ($t = 300\ t_A$) in the simulation (with the chosen normalization and given the photospheric convection has been sped up by a factor ~ 10) only $\sim 5\%$ of the open flux has changed its connection to the photosphere. Note, also, that the reconnection rate increases throughout the simulation but is nearly saturated by $t = 300\ t_A$. Since separatrix surfaces can intersect to produce complex topology in the magnetic carpet, it is possible that multiple reconnections play a role in determining the perturbations to a fluid element. The reconnection layers that develop in the 3D simulation are in general asymmetric due to the independent evolution of plasmas in flux tubes of different magnetic topology.

Since the turnover time for granular scale structure is shorter than the travel time of the solar wind to 1 AU, it would be difficult to envision that such a re-organization of the magnetic carpet can occur without invoking reconnection. However, such reconnection signatures are limited in their spatial extent because of the finite propagation velocity from the diffusion region and on the length of the diffusion region along the current sheet. They also depend on the duration that a reconnection process operates. Therefore, only some fraction of the original tangential discontinuity bounding a flux tube may actually show in-situ signatures of

the reconnection layer. In addition, the young magnetic carpet formed from flux tubes rising up out of the photosphere will be advected against a long-lived open flux tube and reconnect with it to feed it plasma (*He et al.*, 2010; *Yang et al.*, 2013) and to launch Alfvénic signatures *Fisk et al.* (1999); *Tu et al.* (2005). Hence the turnover-time of the magnetic carpet may not be a measure of the lifetime of the more long-lived open flux tubes.

A high resolution 2D simulation is conducted and the expected signature for a spacecraft passing through the outflow boundary is defined. The Walén relation is satisfied for a portion of at least one side of the outflow jet. The annihilation of magnetic field converts magnetic energy into kinetic energy, such that the magnetic field is weaker in the outflow. For sufficiently symmetric reconnection the density in the outflow region is typically larger than in the inflow, and the thermal pressure in the outflow is enhanced above the background. The signature of nonadiabatic heating provided by slow shocks is sensitive to the asymmetries in the initial configuration, but significant changes would only occur for a $\beta < 1$ plasma.

The 2D reconnection simulations show that not only can these signatures be expected for a spacecraft passing through the edge of the outflow jet, but similar changes would occur passing through the edge of the bulge region which forms as the jet interacts with unperturbed plasma at its leading edge. It is interesting that not only the steady state region of the reconnection outflow satisfies conditions for discontinuities that adhere approximately to the Walén relation. A range of 2D simulations were conducted with varying asymmetries, not shown here, in which the conclusions drawn were all the same.

Flux tube boundaries in the solar wind would be expected to have plasma properties either side of the transition that change in a manner consistent with the outflow boundary or bulge region. If the reconnection layer originated on the sun then the signature will evolve as it travels with the solar wind to Earth. The 2D reconnection simulations for different values of β show the guide field enhancement, density increase, and thermal pressure increase are larger in magnitude for a smaller β, and also that a smaller rotation appears at the bulge boundary for a larger β. Large changes in entropy and density across the reconnection jet boundary are expected only where the plasma β is very small. Once the reconnection jet has been convected or propagated into a region with $\beta > 1$, fractional changes in density and entropy are expected to be small. In addition to the change in β, processes such as acceleration and heating of the solar wind as it leaves the sun, ongoing magnetic reconnection, expansion, and turbulence may be capable of modifying the expected changes in plasma properties across these boundaries if they originated on the sun.

An important property of the current layer bounding the reconnection outflow is a natural scale which, for small plasma β, is of the order of the ion inertial scale, or the ion gyro

scale for $\beta > 1$. In both cases, the Walén relation is still a reasonable approximation to identify reconnection layers as demonstrated by many in-situ observations at the magnetopause (*Paschmann et al.*, 1979; *Sonnerup et al.*, 1981), and by numerical studies of Hall MHD reconnection (*Ma and Otto*, 2013).

From the MMS data analysis of solar wind current sheets, we conclude:

Structure and properties of the solar wind observed at 1 AU has origins at the sun as well as due to the in-transit evolution of the magnetic field and plasma. The results of section 6.4 apply specifically to large amplitude current sheets in the solar wind. Many of these current sheets have different magnetic fields and plasma either side of the current layer, which is suggestive that the structure is sourced on the sun. The 3D simulations show reconnection occurring in the solar corona so the picture of many reconnection outflow boundaries in the solar wind is advanced. We determine what percentage of current sheets observed in the solar wind at 1 AU might be generated by reconnection outflows.

Out of a total 381 events, almost 50% of solar wind current sheets satisfy the Walén relation, which is consistent with the spacecraft crossing through the boundary between inflow and outflow regions (either jet or bulge) of a magnetic reconnection layer. It is remarkable, that the corresponding subset with a good boundary normal direction, show a small value of the normalized magnitude of B_n that is consistent with a reconnection layer boundary. Given that all Alfvénic boundaries where a good boundary normal can be found are consistent with a reconnection boundary, this implies that most of those where the boundary normal cannot be found are likely also consistent. This result is also consistent with the conclusions from *Neugebauer and Giacalone* (2010) that rotational discontinuities have typically rather small B_n. It is not certain whether Alfvénic turbulence can generate large B_n rotational discontinuities but we have demonstrated that small B_n is a typical property of reconnection layer boundaries particularly for small magnetic field rotation angles. The width of the observed portions of the current sheets satisfying the Walén relation and having a good normal direction (74 events) is below 4 ion gyro radii for 70 events, also expected for reconnection layer boundaries where dissipation and acceleration is required.

From 184 pressure balanced events with reliable density and magnetic field changes, 170 are consistent with changes expected for a reconnection layer boundary and only 14 are inconsistent. Inconclusive changes occur for 164 events because of the error associated in the standard deviation. However, for plasma $\beta > 1$ this is expected because the expected relative changes are only a few % at reconnection boundaries and difficult to measure unambiguously. Similarly, about 2/3 of all events have magnetic field rotation angles smaller than 50 degrees, also consistent with small magnetic field rotation for reconnection boundaries even if the asymptotic magnetic field has shear of more than 120 degrees.

Given that only one side of the outflow jet or bulge can be expected to satisfy the Walén relation for a sufficiently asymmetric reconnection layer, these results actually indicate that $> 50\%$ of current sheets in this study may be reconnection outflow boundaries. While we have 170 events with consistent $\Delta|B|$ and Δn, with only 14 inconsistent, the 164 inconclusive events are likely mostly consistent but have changes too small as expected for $\beta > 1$ reconnection. Larger changes in entropy and density are more likely to occur for events with smaller plasma β, which are plasma conditions closer to the sun or in the corona as compared to plasma conditions near 1 AU. More work is needed to understand whether such large changes generated by reconnection in a low β plasma can survive the journey to 1 AU. The distribution of rotation angles and general changes of n and S with increasing plasma β are consistent with reconnection layers although individual cases may not be.

Some of the inconsistent events are likely tangential discontinuities, particularly those with small B_n and very poor Walén relation. Tangential discontinuities should be identified based on plasma composition and energetic populations, however it would again be necessary to take into account changes caused by the changing plasma properties from the top of the corona to 1 AU. The reliability of the FPI measurements for velocity and thermal pressure brings into question whether all of the inconsistent cases truly lack the signatures of magnetic reconnection. In addition a proper determination of the anti-parallel magnetic field component is needed to better understand these events, which is possible for the small subset of events where both edges of the outflow boundary can be identified. We have identified a number of these events in our data set and these can be the subject of a future study.

It is important to note that any observation at 1 AU is a snapshot in time. Topology is a structural global property of the magnetic field that, although it may evolve, at any instant in time is a nonlocal property of the field connection. However, the actual evolution has a finite speed for the transport of information. A measurement at 1 AU determines characteristics of a boundary which may have had its origin 2 to 4 days ago in the solar corona and during that time has evolved through expansion, possibly reconnection, and other physical processes. This also implies that any specific connection of the magnetic field to the sun that had existed earlier in the evolution, may have changed. The local observation provides no information about events near a particular boundary that happened after a fluid parcel has started to emerge from the corona.

The absence of an Alfvénic boundary does not prove that reconnection may not operate on the boundary because only some fraction of a large tangential discontinuity current sheet is changed into an Alfvénic outflow structure. We have illustrated that for sufficient symmetry of the process both edges of an outflow boundary can be expected to be Alfvénic. However, it may well be that large asymmetries exist such that only the boundary with the larger

magnetic field rotation satisfies the Walén relation. In view of these aspects, it would seem that 50% is quite large for the fraction of current sheets studied which are consistent with the tested reconnection characteristics. This seems indicative that a large part of the original topological flux tube boundary has undergone reconnection. This estimate, however, does not provide the amount of magnetic flux from a flux tube that has undergone reconnection.

Similarly the presence of an Alfvénic signature does not imply that reconnection must have operated close to the corona. In this sense Section 6.4 provides no positive proof that reconnection operated close to the corona but the presence of reconnection signatures at solar wind current sheets is at least consistent with such a picture. However, the presence of reconnection layers in an environment with $\beta > 1$ and sometimes much greater than 1 seems indicative that the reconnection process started earlier and closer to the sun where the plasma $\beta < 1$. Otherwise, reconnection is less likely to operate because of the diamagnetic drift stabilization in an asymmetric configuration. An estimation of the entire width of the outflow region for events where both edges can be identified could give the age of the reconnection layers but, again, this is out of the scope of this paper. It is possible that reconnection could develop in the transit time on tangential discontinuities with strong current sheets.

The in-situ structure of the solar wind that is revealed by Parker Solar Probe will be vital to understanding this problem. The density and flow variations very close to the sun have been observed to be highly structured (*DeForest et al.*, 2018). These density variations would be expected to be associated with magnetic field changes and in the future these structures can be compared with the current sheets presented here. This will allow to begin to understand the in-transit evolution of the solar wind from the corona to 1 AU.

Chapter 4

Kelvin Helmholtz at Saturn

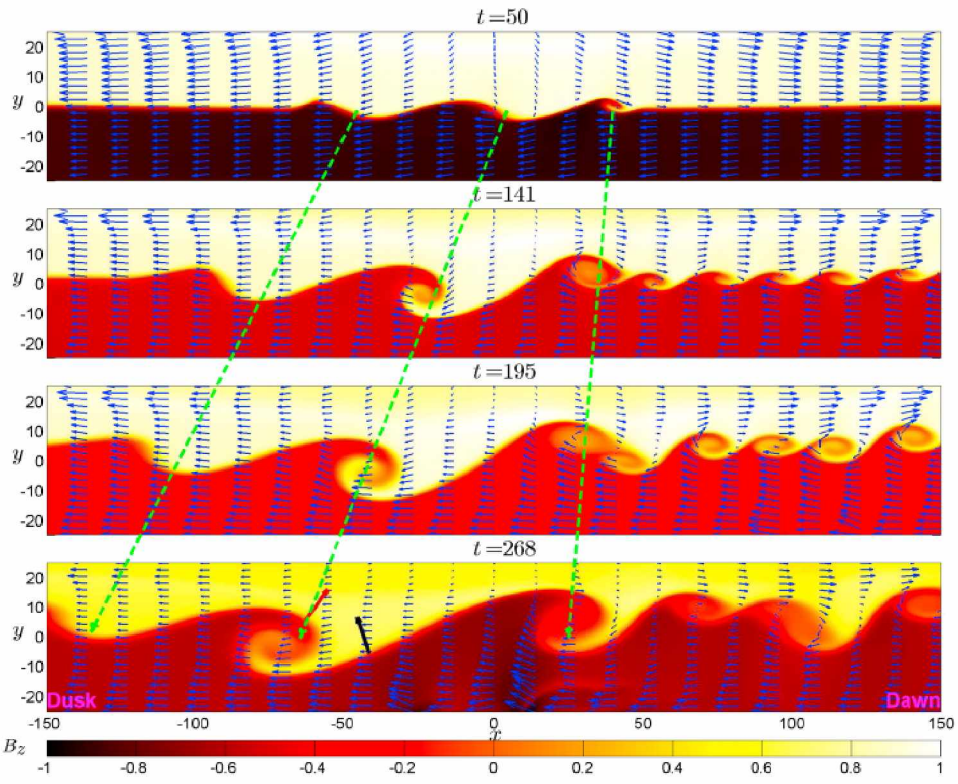

Figure 4.1: Two-dimensional MHD simulation of Saturn's magnetopause boundary showing asymmetric growth and propagation with respect to the subsolar point. *Reproduced from Ma et al.* (2015).

4.1 Local Time Asymmetry of Saturn's Magnetosheath Flows

Abstract[1]

Using gross averages of the azimuthal component of flow in Saturn's magnetosheath, we find that flows in the pre-noon sector reach a maximum value of roughly half that of the post-noon side. Corotational magnetodisc plasma creates a much larger flow shear with solar wind plasma pre-noon than post-noon. Maxwell stress tensor analysis shows that momentum can be transferred out of the magnetosphere along tangential field lines if a normal component to the boundary is present, i.e. field lines which pierce the magnetopause. A Kelvin-Helmholtz unstable flow gives rise to precisely this situation, as intermittent reconnection allows the magnetic field to thread the boundary. We interpret the Kelvin-Helmholtz instability acting along the magnetopause as a tangential drag, facilitating two way transport of momentum through the boundary. We use reduced magnetosheath flows in the dawn sector as evidence of the importance of this interaction in Saturn's magnetosphere.

4.1.1 Introduction

The interaction of the solar wind with Saturn's rapidly rotating magnetodisc has been studied extensively from the perspective of the physical processes occurring at the magnetopause boundary (*McAndrews et al.*, 2008; *Lai et al.*, 2012; *Delamere and Bagenal*, 2013; *Delamere et al.*, 2015b; *Delamere*, 2015; *Masters et al.*, 2014; *Fuselier et al.*, 2014). Emphasis has been placed on the influence of the solar wind on the magnetosphere. In this paper we consider the converse; namely, how does the magnetodisc interact with the magnetosheath at the solar wind-magnetosphere interface? Tangential drag at the magnetopause leads to the two way transport of momentum, suggesting that magnetosheath flows in the pre-noon sector could be significantly modified by sunward magnetospheric flows. The physical processes leading to tangential drag (often considered viscous-like (*Axford and Hines*, 1961; *Axford*, 1964; *Vasyliunas*, 2015)) include, for example, the sheared-flow driven Kelvin-Helmholtz (KH) instability and/or kinetic Alfvén waves (KAW) generated at the magnetopause boundary (*Johnson and Cheng*, 1997; *Wing et al.*, 2014). In this paper we focus our discussion on the KH instability, following the suggestion by *Delamere and Bagenal* (2010), as a means to quantify tangential drag at the magnetopause boundary. Using plasma properties (moments) derived from the Cassini Plasma Spectrometer (CAPS) data between 2004 to 2011 (*Young*

[1]Manuscript coauthors: P. A. Delamere, X. Ma, M. F. Thomsen, R. J. Wilson, F. Bagenal

et al., 2004), we show that the flow asymmetry is indeed present with roughly a factor of two difference between pre-noon and post-noon flows.

Desroche et al. (2013) conducted MHD simulations of solar wind flow past Saturn's polar flattened magnetosphere to understand the gross behavior of magnetosheath flows. The flattening is expected from the latitudinal confinement and radial expansion of magnetospheric plasma under the action of centrifugal stresses. Even for small flattening parameters, the equatorial tailward magnetosheath flows are reduced from those in the polar regions due to, essentially, dominant hydrodynamic flows over the poles. The asymptotic velocity found near the equatorial flanks is roughly 0.5 v_{sw}, while the polar value is roughly v_{sw}, where the subscript *sw* denotes a solar wind quantity. The interplanetary magnetic field (IMF) orientation near the magnetopause boundary is strongly influenced by the polar flattening. For an initially small angle between y and z IMF components (IMF clock angle) of $+5°$ ($-5°$), the field rotates northward (southward) into the z ($-z$) direction as it moves toward the flanks, leading to favorable conditions for the KH instability, minimizing magnetic tension in the sheared flow direction (*Chandrasekhar*, 1961).

The presence of KH waves at Saturn's dayside magnetopause boundary has been addressed in the literature (*Masters et al.*, 2009, 2012; *Delamere et al.*, 2011; *Wilson et al.*, 2012). In addition, *Ma et al.* (2015) demonstrated a local time asymmetry of KH waves using a two-dimensional MHD simulation with local time dependent flow shears. Vortices forming in the pre-noon and subsolar region were transported duskward by the corotating magnetospheric flow, forming well-defined and long-lived vortex structures. We postulate that this is the reason dusk side KH waves were more easily identified by *Masters et al.* (2012) and *Delamere et al.* (2011). The growth rate of the KH instability on the dawn side is very high and the simulations showed rapid diffusion into a boundary layer, making the identification of KH vortices difficult. Boundary normal analysis confirmed this model result with persistent boundary normal modulation by KH waves on the dusk side.

It has been demonstrated that reconnection and Kelvin-Helmholtz modes interact (*Fairfield et al.*, 2000; *Hasegawa et al.*, 2004; *Ma et al.*, 2014a,b). A condition for momentum transport at the magnetopause boundary is the presence of a normal magnetic field component, producing magnetic shear stresses. Intermittent reconnection associated with the KH instability can facilitate magnetic field line threading of the magnetopause boundary. *Delamere and Bagenal* (2010) proposed the KH instability at the giant magnetospheres, driving intermittent reconnection (vs. large scale reconnection), as a plausible source of tangential drag at the magnetopause boundary. This process is analogous to the viscous-like interaction described by *Axford and Hines* (1961). In this paper, we present evidence supporting the importance of a tangential drag at the magnetopause boundary, showing that reduced

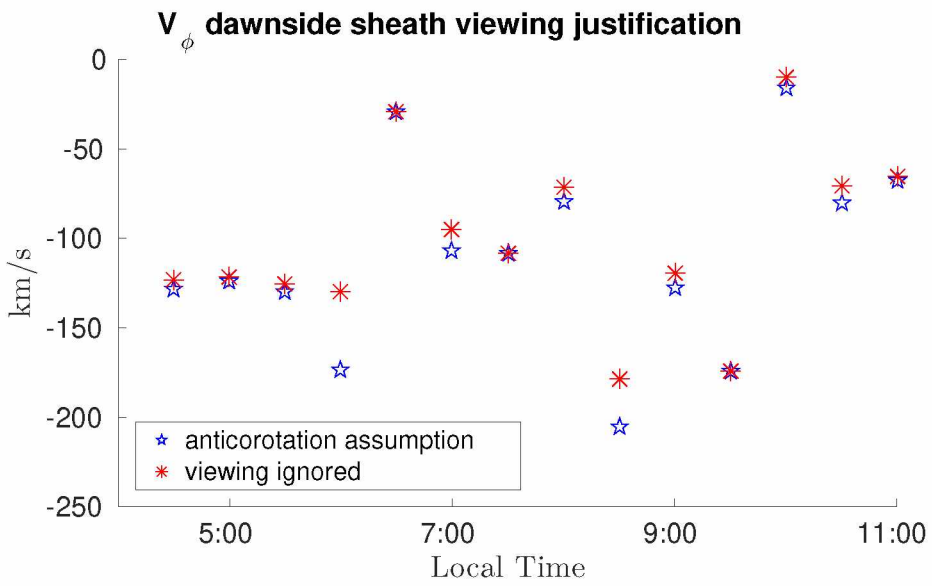

Figure 4.2: Comparison of dawnside V_ϕ averages in local time obtained by selecting "non-corotating" instrument viewing (blue) vs. the same calculation where the look direction is not considered(red). The average percentage difference across all bins is calculated as 10%

dawnside magnetosheath flows at Saturn are consistent with Maxwell stresses generated at the magnetopause boundary.

4.1.2 Data Analysis

The numerically integrated moments from CAPS (http://www.caps.lanl.gov/moments.html) through 2011 were used to calculate average flow properties in the magnetosheath (*Thomsen and Delapp*, 2005; *Thomsen et al.*, 2010). Adequate instrument look direction is critical for determining valid moments. For simplicity we defined the magnetosheath flow directions for the dawn and dusk sectors as $-\hat{\phi}$ and $+\hat{\phi}$, respectively, where $\hat{\phi}$ is the azimuthal direction. As suggested by (*Thomsen et al.*, 2010) we filter for points where the detector is looking into the flow, which means that in the prenoon magnetosheath we must be able to identify when the anticorotation direction is in the field of view (FOV). The CAPS moments data set available at the PDS which is used for this study, has a flag indicating when flows in the $+\hat{\phi}$ direction would be in the CAPS FOV. For measurements post-noon, we require that this flag is set. Since the instrument covers 2π steradian through actuation, we make the assumption that if it is not looking into the direction of corotational flow, then it is capturing anti-corotational flow, so for pre-noon locations we use only measurements for which the corotation flag is not set. A comparison of pre-noon averages obtained using this viewing filter and averages which ignore the look direction is shown in Figure 4.2. As expected, selecting the correct instrument

viewing always gives a set of larger values. In addition, using Saturn-centered instrument viewing (*Wilson et al.*, 2008), we also selected cases where the flow direction was fully within the instrument view and found little difference in the average V_ϕ compared to cases where the flow direction was at the edge of the instrument view, suggesting that sampling half of the distribution is sufficient for determining flow speed. These lenient restrictions are vital for obtaining meaningful statistics as the instrument is often pointed almost directly at the planet. This circumstance gives a dawn side data set which has a quarter of the data used to calculate relevant averages on the dusk side, and thus has half of the statistical significance quantified as standard error of the mean. In addition, data points were only selected for cases within $\pm 30°$ of latitude from the equator, and only for cases that satisfied requirements for instrument actuation and spacecraft rolling (*Thomsen et al.*, 2010).

Our expectation for a tangential drag is that the magnetosheath flows are affected by magnetospheric flows only in close proximity to the magnetopause boundary due to momentum transfer along the mostly tangential IMF field lines. Thus, we sorted our results based on time elapsed from a given boundary crossing (e.g., magnetopause and bow shock) as defined by *Delamere et al.* (2013, 2015a). The exact locations of the boundaries following a crossing are unknown; however, we note that the Cassini spacecraft traverses approximately half of the width of the magnetosheath in 1000 minutes (e.g., 6 R_S at 6 km s^{-1} (*Sergis et al.*, 2013)), assuming a static magnetospheric configuration.

Using all magnetosheath values on both inbound and outbound trajectories with valid instrument viewing which occur within 500 minutes of a magnetopause crossing, we calculated an average azimuthal flow velocity (V_ϕ) as a function of local time. Figure 4.3 shows the local time variation in V_ϕ for bins with a resolution of 30 minutes, which shows considerable asymmetry (in magnitude and variability) relative to the subsolar point at 12 LT. We are careful to interpret the dawnward shift of the stagnation point from local noon, which is also a feature found by *Pilkington et al.* (2015), since the choice of viewing at local noon is ambiguous and we have chosen to filter for positively directed azimuthal flow in this region. The blue shaded bars give an average of the prenoon or postnoon values, excluding those at [11:30, 12:00], and [12:00, 12:30] in lieu of ambiguous viewing. For the remainder of this paper we will use an estimate of 125 km s^{-1} for the dawn side and 200 km s^{-1} for the dusk side as representative values for the average V_ϕ.

The left half of Figure 4.4 shows the dependence on spacecraft time from the magnetopause boundary crossing of the average flows in the local time sectors 7:00-11:00 and 13:00-17:00. It is clear that the dawn side flow speed (red) is lower than the dusk side (blue) by $\sim$75-100 km s^{-1} and this deficit gradually lessens as Cassini's presumed distance to the magnetopause boundary increases. A calculation of distance from the boundary cannot be

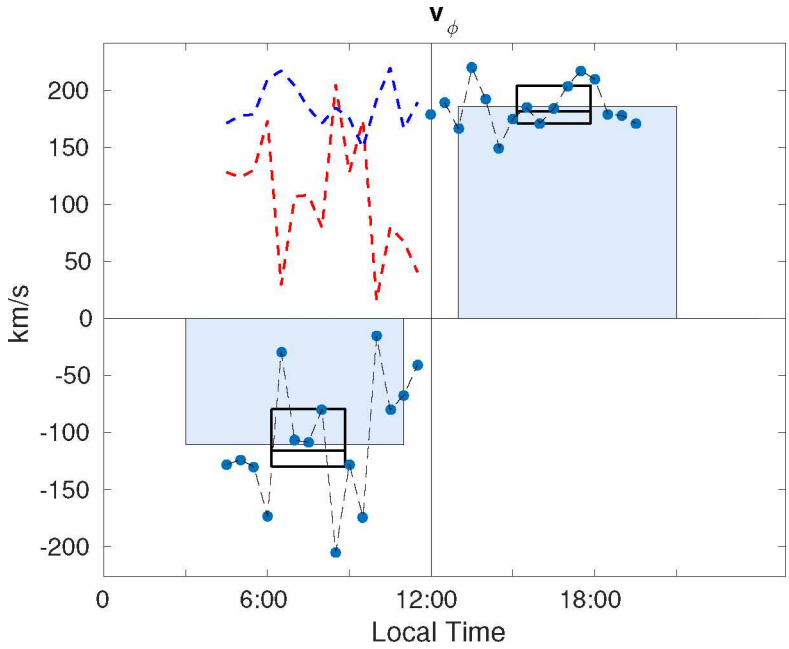

Figure 4.3: Saturn's average V_ϕ magnetosheath flows in 30 minute local time bins. The blue bars show the dawn vs. dusk average, excluding 11:30 to 12:30, while the box plot (black) gives the 25th, 50th, and 75th percentiles of the points included in this average. The blue dashed line is the mirror of the dusk velocities across the y-axis, while the red is the dawn velocities mirrored across the x-axis.

made with the spacecraft time and its velocity since the magnetopause may be moving in response to solar wind conditions at a rate which we cannot determine. However, the time elapsed from the boundary over which the deficit exists suggests that a significant fraction of magnetosheath flows are reduced from the expected asymptotic value of 200 km s^{-1} (*Desroche et al.*, 2013). The spread of values indicated by the percentile bars is clearly larger on the dawn side, which may not be strictly due to asymmetric local time sampling of the spacecraft, but has physical significance in terms of variability in flow conditions. Additionally, the right side of Figure 4.4 shows the time elapsed from bow shock crossings into the magnetosheath where time now increases from right to left. The apparent dawn-dusk symmetry for flows in proximity to the bow shock shows that the flow deficit exists for only the magnetosheath nearest to the magnetopause.

4.1.3 Discussion

Our interpretation of the dawn-dusk asymmetry of Saturn's magnetosheath flows is summarized in Figure 4.5. The region of reduced flow is illustrated by the shaded region (red), showing a gradient in flow deficit as a function of proximity to the magnetopause boundary.

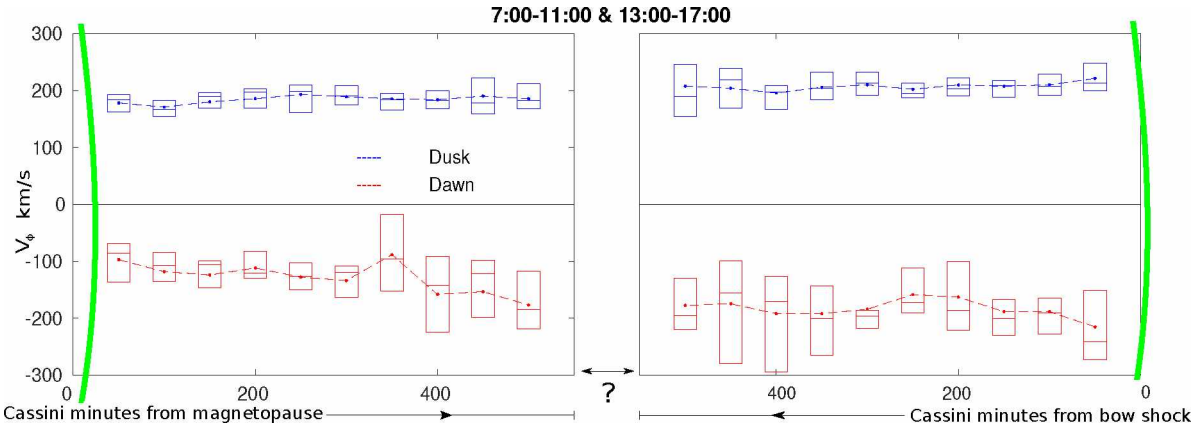

Figure 4.4: The first 500 minutes after each magnetopause (left) or bow shock (right) boundary crossing. The value of each point above is calculated as an average of the relevant time bin across all boundary crossings in the corresponding prenoon or postnoon sectors given in the title. The error bars give the 25th, 50th, and 75th percentiles of the data used to calculate the average. Green curves represent the boundaries, and the question mark portrays that we are always unsure as to the actual distance to either boundary.

The Kelvin-Helmholtz vortices (green) highlight the dawn-dusk asymmetry modeled by *Ma et al.* (2015), whereby vortices observed in the dusk sector were formed in the subsolar region and advected duskward by corotational flows in the magnetosphere. Post-noon, the flow-shear is minimized and thus the KH waves no longer actively grow. The highly KH unstable dawnside boundary, on the other hand, can mediate momentum transfer.

Intermittent reconnection associated with KH could play an important role in quantifying the role of a viscous-like interaction; therefore, we use this concept as a starting point to discuss the dawnside momentum transfer. An estimate of the momentum transfer process can be made by considering the flux conservative form of the momentum equation in steady state which is given by *Vasyliunas* (2015), i.e.,

$$\nabla \cdot \left[\rho \mathbf{u}\mathbf{u} + \mathbf{P} + \frac{\mathrm{B}^2}{2\mu_\mathrm{o}}\mathbf{I} - \frac{\mathbf{B}\mathbf{B}}{\mu_\mathrm{o}} \right] = 0 \tag{4.1}$$

If we assume that the momentum flux density of the magnetosheath flow is conserved in the absence of momentum transfer from the magnetosphere, then $\nabla \cdot \rho\mathbf{u}\mathbf{u} = 0$. For tangential momentum transfer normal to the boundary surface and the assumption of isotropic pressure, only the first and last terms of the steady state momentum equation can represent shear stresses through off diagonal elements. Let $+\hat{\mathbf{t}}$ be the tangential magnetosheath flow (tailward) direction and $+\hat{\mathbf{n}}$ be the direction normal to the magnetopause boundary, pointing from the magnetosphere to the magnetosheath. If the magnetosheath flow is modified (i.e., reduced) due to Maxwell shear stresses at the magnetopause boundary, then $\mathbf{B}\mathbf{B} \approx -\mathrm{B_t}\mathrm{B_n}\hat{\mathbf{t}}\hat{\mathbf{n}}$

(blue lines in Figure 4.5). Indeed we can also consider the Reynolds stress, $(\rho u_t u_n)\hat{\mathbf{t}}\hat{\mathbf{n}}$; however, since the momentum flux due to Maxwell stresses is 2-3 times larger (*Miura*, 1984), we omit this contribution from our calculations.

The momentum transfer from the solar wind to the magnetosphere was investigated by *Delamere and Bagenal* (2013) in terms of the limiting case where the IMF fully threads the magnetopause boundary. In this limit, the giant magnetospheres can essentially be treated as a comet-like interaction where the solar wind is mass loaded by the magnetospheric plasma sources. Following the Walén relation for an Alfvénic interaction, the maximum momentum flux density delivered to the magnetosphere is

$$\frac{\mathbf{BB}}{\mu_o} \approx \frac{M_{sw} B_{IMF}^2}{\mu_o}\hat{\mathbf{t}}\hat{\mathbf{n}} \tag{4.2}$$

where M_{SW} is the solar wind Mach number and B_{IMF} is the IMF strength. The volume integral of the steady momentum equation can be written as a surface integral via the divergence theorem, or

$$\int (\rho u_t u_t)_{sh} da_t = \int \frac{B_t B_n}{\mu_o} da_n \tag{4.3}$$

where the subscript "*sh*" refers to magnetosheath quantities and where da_t refers to the magnetosheath inflow/outflow surfaces and da_n is the magnetopause boundary. The ratio of tangential area to the normal area is estimated to be $a_t/a_n \sim 1/5$ for an affected magnetosheath width ~ 3 R_s and a distance along the magnetopause boundary from 7 to 10 LT $\sim$15 R_S. This area ratio estimate avoids the flank/tail region where flows may not be corotational and is based on the effected magnetosheath width from the data (Figure 4.4). The average magnetosheath number density in this region from the numerical moments is 0.18 cm^{-3}. If we assume that the interplanetary magnetic field, on average, is 0.5 nT (*Jackman and Arridge*, 2011), and use the flow deficit from the expected value calculated from the data $(\Delta u_t)_{sh} \sim 75$ km s^{-1}, then we find

$$\rho(\Delta u_t)_{sh}^2 \left(\frac{\mu_o}{M_{sw} B_{IMF}^2}\right)\left(\frac{a_t}{a_n}\right) \sim 0.2 \tag{4.4}$$

Thus, the momentum flux deficit is consistent with the solar wind transferring a significant fraction of the maximum possible momentum to the magnetosphere in the dayside sector. The fully draped IMF field configuration is not expected to be realized until farther downstream in the tail region, yet the momentum transfer is found to be substantial.

Alternatively, we could consider preferential mass transport from the magnetosphere, leading to a net mass loading of the magnetosheath. In the case of KH, the $\rho u_t u_n$ term in Eq. 4.1 would be unbalanced, with more momentum flux directed from the magnetosphere

to the magnetosheath. For a diffusive transport process like KAW, the effective mass loading of the sheath could be treated with a mass loading term on the right hand side of Eq. 4.1, such that $\rho(\Delta u^2)_{sh} a_t = \dot{M} u_{ms}$, where $\dot{M}$ is the net mass loading rate of the sheath and u_{ms} is the magnetospheric flow speed (upper limit) in the Saturn/Sun reference frame. For u_{ms} = 100 km s^{-1} and $a_t = 3{\times}4$ R_s^2, $\dot{M} \sim 1$ kg s^{-1}. This is a small fraction of the plasma mass transport rates of 50 - 100 kg s^{-1} from Enceladus (*Fleshman et al.*, 2013).

Finally, we conclude that our findings are consistent with the 7% dawnward shift of the magnetopause boundary discussed by *Pilkington et al.* (2015), who also attributed their finding to "the intrinsic asymmetry in plasma flow around the planet with respect to the direction of solar wind flow." Although the solar wind is the primary driver of the system, magnetospheric phenomena could also contribute to the dynamics of the plasma flow. In simulations by *Kivelson and Jia* (2014), a system of field aligned currents rotating with the planet produces modulations in field and plasma conditions which occur at the planetary oscillation period. The asymmetry in the shape of the magnetopause which they found in simulations was similar, albeit larger, than that found from the data study by *Pilkington et al.* (2015), suggesting that internal drivers could also influence dawn/dusk asymmetry. Fundamentally, however, the solar wind interaction must be at the root of observed dawn/dusk asymmetries.

4.1.4 Conclusions

We summarize our findings as follows:

- Cassini plasma data shows an asymmetry of $\sim$ 75 km s^{-1} between the dawn and dusk sides of Saturn's magnetosheath. We interpret this as a consequence of the flow shear between the solar wind and corotational magnetosphere plasma which is maximized on the pre-noon flank.

- Saturn's interaction with the solar wind could be dominated by viscous-like processes at the magnetopause boundary – a situation that is very different from Earth where large-scale Dungey reconnection dominates.

- The momentum deficit in Saturn's dawnside magnetosheath is consistent with maximum momentum transfer via magnetic shear stresses from the solar wind.

- The large momentum transfer to the magnetosphere suggests that local time asymmetries in magnetospheric dynamics are strongly influenced by the solar wind interaction.

- The dawn flank is subject to significant flow shears and is likely subject to ongoing Kelvin-Helmholtz instability and related intermittent and small-scale reconnection.

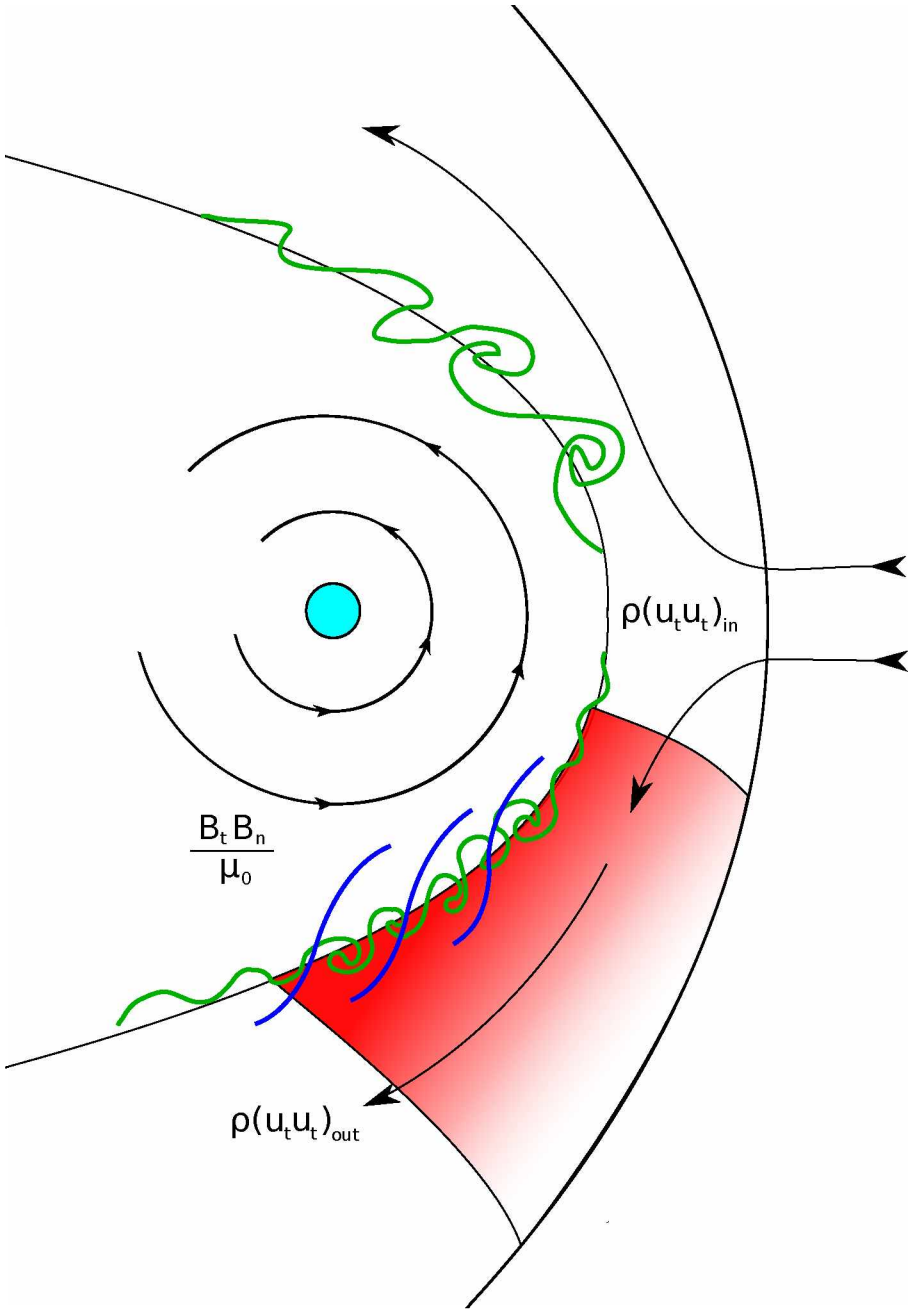

Figure 4.5: Magnetic field lines (blue) thread the dawnside magnetopause boundary in the presence of Kelvin-Helmholtz waves (green). The tangential and normal components of the magnetic field across the magnetopause boundary constitute Maxwell shear stresses, facilitating momentum transfer. The shaded area shows a gradient representing the severity of the momentum deficit.

- Similar considerations are applicable to any giant magnetosphere whose corotating magnetodisc creates a sheared flow with the solar wind which is asymmetric in local time, i.e. Jupiter. The hydrodynamic conditions of this configuration imply an asymmetry of the type we present here.

4.2 Identifying Active Kelvin-Helmholtz Vortices on Saturn's Magnetopause Boundary

Abstract[2]

For $\sim$ 2000 magnetopause encounters observed by Cassini, we analyze plasma and magnetic field near the boundary. This boundary can be unstable to the Kelvin-Helmholtz instability (KHI) which causes significant magnetic field fluctuations and variations in plasma properties. Bulk flow near the magnetopause indicates KH activity when reversed from the expected direction. Hybrid simulations of the KHI indicate heating and transport can be significant in an actively growing vortex and also that current sheets are ubiquitous. Cassini observations are filtered for disturbed magnetic field events near the magnetopause and a turbulent heating rate density and mass diffusion coefficient are calculated. We test the hypothesis that enhanced values for these quantities provide an unambiguous means of identifying active KH events. The meaning of "near" Saturn's magnetopause is approximate with no solar wind monitor. Data within 100 minutes of a magnetopause encounter are considered.

4.2.1 Introduction

The solar wind interaction with Saturn's rapidly rotating magnetodisc involves asymmetric flow shear between the subcorotating outer magnetosphere and magnetosheath. Flow shear is the primary suspect for tangential drag coupling the solar wind to the magnetosphere in a viscous-like process (*Axford and Hines*, 1961) rather than large-scale reconnection. Contrasting with Earth, a viscous-like interaction has been suggested as dominant at Saturn compared to global-scale reconnection (*Masters*, 2018).

Kelvin-Helmholtz instabilities (KHI) mix plasmas (*Ma et al.*, 2017; *Fairfield et al.*, 2000; *Hasegawa et al.*, 2004), drive magnetic reconnection (*Ma et al.*, 2014a), and transport momentum across the magnetopause (*Burkholder et al.*, 2017; *Delamere et al.*, 2018). The boundary width is typically $\sim$ 1 R_s (Saturn radius) (*Masters et al.*, 2011) but varies, which is important since the flow shear magnitude (Δv) determines the growth rate (*Miura and Pritchett*, 1982). *Ma et al.* (2015) showed growth rates on the dawn magnetopause are large

[2]Manuscript coauthors: P. A. Delamere, J. R. Johnson, C. S. Ng

enough that a diffuse boundary layer forms on the order of minutes. In addition, KH vortices induce turbulence through secondary instabilities (*Matsumoto and Hoshino*, 2004) which can dissipate magnetic field energy (*Saur*, 2004). A turbulent cascade has been demonstrated in hybrid simulations of the KHI (*Delamere et al.*, 2018), where three dimensional effects were particularly important.

Initial attempts to identify KH at Saturn's magnetopause included boundary normal analysis (*Masters et al.*, 2009) and bipolar magnetic field signatures (current sheets) (*Delamere et al.*, 2013). Surprisingly, these studies concluded the dusk flank (minimum flow shear) was KH active. *Ma et al.* (2015) demonstrated quasi-static KH structures are indeed prevalent post-noon due to advection from the pre-noon sector. The goal of this paper is to identify actively growing (i.e., nonlinear roll-up phase) KH vortices at Saturn's magnetopause boundary.

Values for a turbulent heating rate density q and diffusive transport coefficient $D_\perp$ are substantial in hybrid simulations of the KHI during the active nonlinear growth phase. We are therefore motivated to use Cassini magnetometer (MAG) (*Dougherty et al.*, 2004) data to estimate q and $D_\perp$ as proxies for KHIs. In addition, we use numerical moments (*Thomsen and Delapp*, 2005; *Thomsen et al.*, 2010; *Wilson et al.*, 2008) of the Cassini Plasma Spectrometer (CAPS) to identify reversed flows as another signature of active KH. Using the magnetopause boundary identifications from *Delamere et al.* (2013), we determine the local time distribution and global occurrence rate of active KHIs near Saturn's magnetopause.

4.2.2 Magnetopause Boundary Plasma Flows

During the active nonlinear roll-up phase of the KHI, plasma circulates vortically. Magnetosheath plasma moving toward the subsolar point suggests flow reversal observed within an active KH vortex. For magnetospheric plasma at the magnetopause, flow reversed from corotation is likely swirling within a KH vortex. Interchange motions and other density fluctuations could also be responsible for structure on the magnetospheric side of the boundary (*Goertz*, 1983), as the specifics of the internal transport mechanism are not well known.

Delamere et al. (2013) identified 1919 magnetopause crossings during 2004-2012. Figure 4.6(a) gives average azimuthal velocity (v_ϕ) in the magnetosheath from CAPS at these magnetopause encounters. The data are numerical ion moments from CAPS energy spectrograms (http://www.caps.lanl.gov/moments.html). CAPS' field-of-view is important and we use the magnetosheath filtering proposed by *Burkholder et al.* (2017). Averages are calculated for magnetosheath data within 100 minutes of the crossing. For a static boundary, 100 minutes corresponds to 0.5 R_s for a 5 km/s spacecraft velocity. Conversely, 100 minutes gives 8 R_s for a magnetopause expanding at the fast mode speed $C_f \sim 80$ km/s. In Figure 4.6(a),

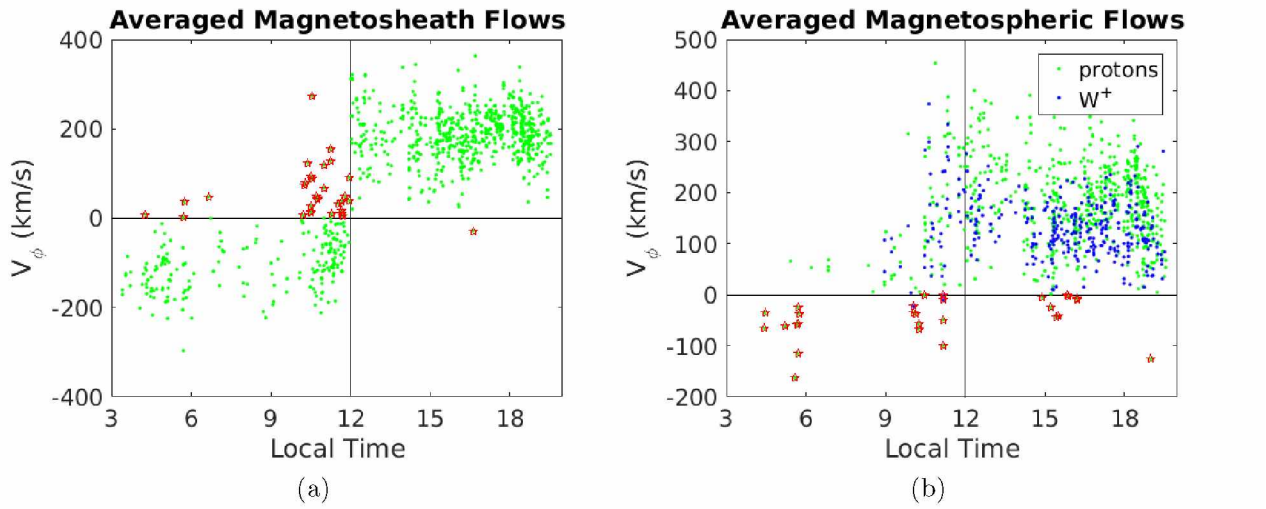

Figure 4.6: Magnetosheath (a) and magnetosphere (b) azimuthal flow (v_ϕ) averaged over 100 minutes nearest a magnetopause boundary crossing.

starred events indicate when average magnetosheath flow was reversed from tailward. In Figure 4.6(b), average v_ϕ for magnetopause traversals is given for protons and W^+ (sum of water group ions) in the magnetosphere. The average occurs for the same time interval as Figure 4.6(a). Starred events indicate when the flow was reversed from corotation.

Figure 4.6(a) gives 31 magnetosheath events with 1 event post-noon and the remainder pre-noon. A majority of reversed flows occur from 10-12 local time (LT). Figure 4.6(b) shows 25 magnetospheric reversed flow events. The dawn sector shows 16 events and 9 events occur LT > 12. This gives a KH active dawn magnetopause $14 \pm 2.8\%$ of the time and $1 \pm 1.4\%$ for the dusk. The LT sector 10-12 is active $18 \pm 3.7\%$ of the time, where flow shear is maximized and stationary KH vortices can form due to balanced momentum flux. Interestingly, this estimate for the KH occurrence rate is similar to $\sim 19\%$ determined at Earth (*Kavosi and Raeder*, 2015).

Due to momentum flux balance, the down-tail advection of an active KH should be $\sim \Delta v/2$ so reversed flow observations require the correct trajectory. Since the expected magnitude of magnetosheath velocity is ~ 200 km/s for dawn and dusk flanks (*Desroche et al.*, 2013), cases in Figure 4.6 with significantly reduced flows could indicate KH activity. The starred points LT < 6 in Figure 4.6(b) may be generated by internal transport, but proximity to the magnetopause (≤ 100 mins) suggests a KH origin.

4.2.3 Heating Rate Density and Diffusion Coefficient

For a discussion of q based on weak and strong MHD turbulence, see *Ng et al.* (2018). We take q in the strong turbulence regime:

$$q = \frac{\delta B_\perp^3 k_\perp}{\sqrt{u_0^3 \rho}} \tag{4.5}$$

where $\delta B_\perp$ is the perpendicular magnetic field fluctuation at an inverse scale $k_\perp$, a perpendicular wavenumber in the inertial range, and ρ is mass density. At Jupiter and Saturn, q has been calculated using a formalism for strong kinetic Alfvén wave (KAW) turbulence and magnetohydrodynamic (MHD) turbulence (*Saur*, 2004; *von Papen et al.*, 2014; *Kaminker et al.*, 2017; *Ng et al.*, 2018). At Saturn, *Kaminker et al.* (2017) estimates the global average $q \sim 10^{-17}$ W/m^3.

Diffusive ion transport perpendicular to magnetic field lines was discussed in *Johnson and Cheng* (1997) and a general form of the diffusion coefficients is presented in Equation (1) of *Chaston et al.* (2009):

$$D_W \approx \sqrt{\frac{\pi}{8}} \sum_{j=1}^{6} \sum_k \frac{1}{|k_{||}| v_{ti}} \left| \frac{E_Y}{B_0} \right|^2 d_j \tag{4.6}$$

where we neglect cross terms d_{4-6} as they are generally small compared with d_{1-3}. In the limit of small $k_\perp \rho_i$, the d_3 term dominates and

$$\lim_{k_\perp \rho_i \to 0} R_{11}^2 \to k_\perp^2 \rho_i^2 e^{-1/\beta}.$$

Finally, taking v_{ti} (ion thermal velocity) $\sim v_A$ (Alfvén velocity), and normalizing in terms of the quantity that controls the transport, which, for the case of d_3, is the mirror force:

$$D_\perp = \sqrt{\frac{\pi}{2}} \frac{v_A}{|k_{||}|} e^{-1/\beta} \sum_{k_\perp \rho_i < 1} \left| \frac{\delta B_{||}}{B_0} \right|^2 k_\perp^2 \rho_i^2 \tag{4.7}$$

where ρ_i is the ion gyroradius, β is plasma beta (chosen as $\beta = 1$ due to superthermal population), and $\delta B_{||}/B_0$ is the normalized parallel magnetic field fluctuation at an inverse scale $k_\perp$. The parallel wavenumber $k_{||} = 2\pi/R_{Saturn}$ is chosen as a lower limit from the scale height of the magnetodisc resonant cavity. Equation 4.7 describes the transport contribution from transit-time damping (*Johnson and Cheng*, 1997; *Chaston et al.*, 2009), which occurs because KAWs drive density and pressure perturbations that produce magnetic field strength fluctuations (magnetic bottles). Resonant particles experience field-aligned acceleration by mirror forces, which results in modified perpendicular drift motion and ion transport across

field lines. This KAW driven mechanism can quantify transport but large gyroradius effects, magnetic reconnection, and superdiffusion would not be included.

The relative magnitudes of d_{1-6} will be the subject of future studies using hybrid simulations where the spectrum of electric field fluctuations is available. We neglect the other terms in Equation 4.6 for these order of magnitude estimates and to facilitate direct comparison between hybrid simulations and Cassini observations.

4.2.4 Hybrid Simulations

Three-dimensional hybrid simulations (see *Delamere et al.* (2018) for model description) of the KHI are conducted with Saturn-like parameters (see Table 1 in *Delamere et al.* (2018)). The electron pressure term included in the electron momentum equation captures the effects of parallel electric fields associated with KAWs. These results represent initial findings from a study with broader implications for turbulent heating and transport in the hybrid model.

To find q, the two-dimensional Fourier power spectrum $P(k_\perp)$ of $\delta B_\perp$ is calculated from a slice along the magnetic field. Since $P(k)k \sim \delta b^2$ (*Leamon et al.*, 1999), we can calculate $(P(k_\perp)k_\perp)^{3/2} \sim \delta B_\perp^3$ which is convolved with $k_\perp$ in Equation 4.5. Similarly, given the power spectrum $P'(k_\perp)$ of $\delta B_{||}/B_0$, we calculate $P'(k_\perp)k_\perp \sim |\delta B_{||}/B_0|^2$. Density and temperature for Equations 4.5 and 4.7 are averaged over the simulation volume, giving $q \sim 2 \times 10^{-14}$ W/m^3 and $D_\perp \sim 4 \times 10^9$ m^2/s.

The temporal variation of average energy gives $q \sim 3 \times 10^{-15}$ W/m^3, a lower limit because q tends to increase with simulation run time. We also note that the grid resolution (0.4×ion inertial length) was insufficient to adequately resolve the dissipation scale. The slope of mixed cells vs. time gives $D_\perp \sim 1 \times 10^{10}$ m^2/s, where a mixed cell has 75% particles from one side of the boundary and 25% from the other (*Delamere et al.*, 2011). This is a factor ~ 3 greater than above because magnetic reconnection, large ion gyroradius effects, and "superdiffusion" (*Cowee et al.*, 2009) are not quantified by Equation 4.7.

4.2.5 Disturbed magnetic fields near Saturn's magnetopause

At Saturn's magnetopause, magnetic reconnection couples the planetary and solar wind magnetic fields, generating Maxwell stresses, however large-scale Dungey-type reconnection has been shown to be inconsequential compared to a viscous interaction (*Masters*, 2018). KHIs, believed to be a primary component of the viscous interaction, drive intermittent reconnection and produce significant magnetic field fluctuations. A KH active magnetopause will contrast starkly with an inactive boundary. Panels (a) and (b) of Figure 4.7 give example quiet and disturbed magnetic fields observed near Saturn's magnetopause.

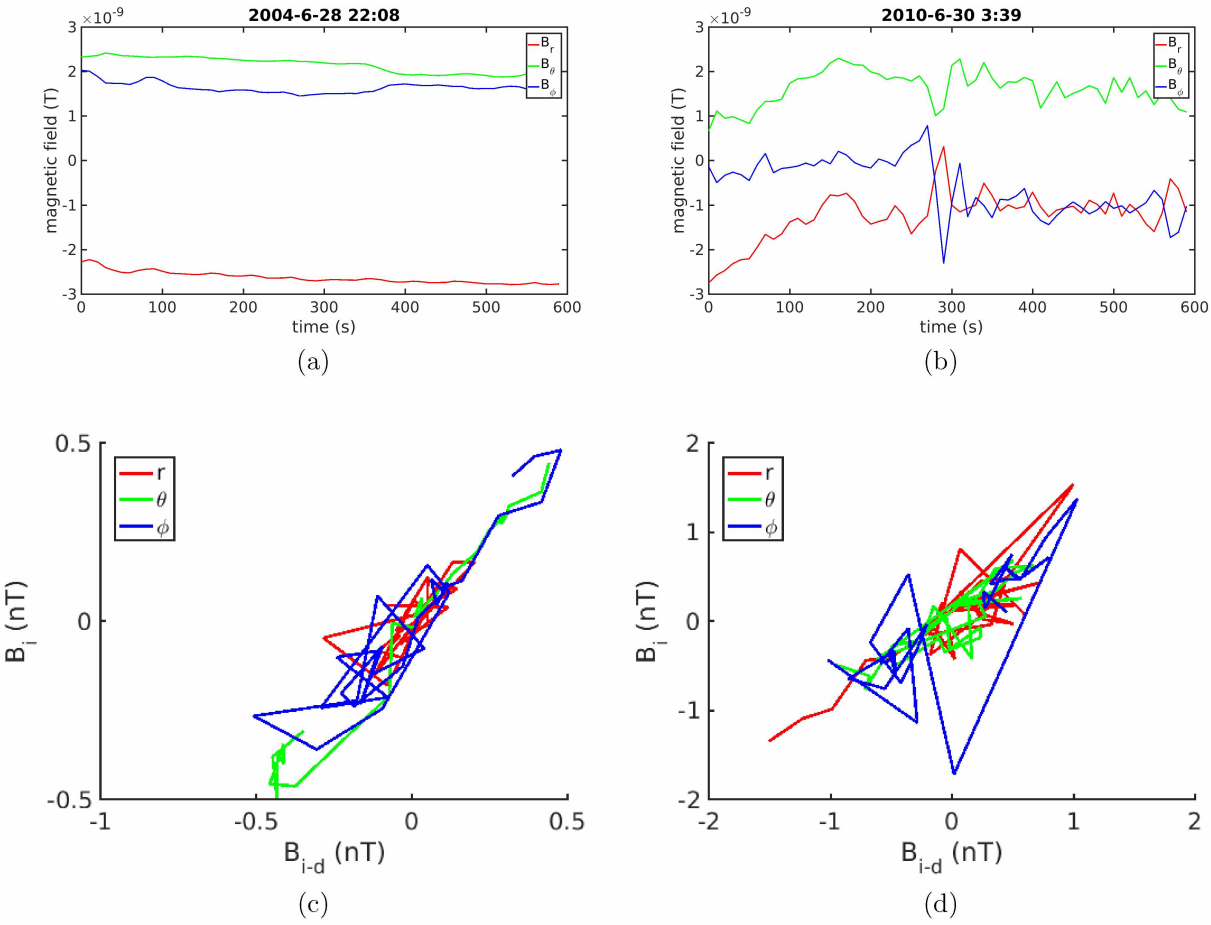

Figure 4.7: Quiet (a) and active (b) magnetic fields near Saturn's magnetopause. Note the current sheet crossing in (b) at $t \sim 300$. Panels (c) and (d) show embedding diagrams for (a) and (b), respectively.

With 10 minute sliding windows, we analyze 10-second averaged MAG time series for $> 42,000$ windows within 100 minutes of Saturn's magnetopause. All windows come from the magnetospheric side of the magnetopause. Each window is classified as active or quiet using three measures of magnetic activity. The threshold between quiet and active is difficult to precisely define, however the requirement of a current sheet crossing can help to resolve this ambiguity.

First, the fluctuation $\delta\mathbf{B} = \mathbf{B}(t) - \mathbf{B}_0$ is calculated from the magnetic field time series $\mathbf{B}(t)$, where $\mathbf{B}_0$ is the time averaged $\mathbf{B}$. The measure of magnetic activity is $\delta B = \sqrt{\delta B_r^2 + \delta B_\theta^2 + \delta B_\phi^2}$ (KRTP coordinates) averaged over the 10 minute window. Second, the eigenvalue problem is solved for directions of minimum, intermediate, and maximum variance n_μ:

$$\sum_{\nu=1}^{3} M^{B}_{\mu\nu} n_\nu = \lambda n_\mu$$

where the variance matrix for the magnetic field is given by $M^{B}_{\mu\nu} = \langle B_\mu B_\nu \rangle - \langle B_\mu \rangle \left\langle B_\nu \right\rangle$ (*Paschmann and Daly*, 1998). For eigenvalues $[\lambda_1, \lambda_2, \lambda_3]$ the geometric mean $\mathcal{E} = (\lambda_1 \lambda_2 \lambda_3)^{1/3}$ gives a measure of the total variance for $\mathbf{B}(t)$.

Third, a method is borrowed from nonlinear time series analysis known as delay-coordinate embedding (*Bradley and Kantz*, 2015). Embedding diagrams are similar to hodograms, however, 2-dimensional hodograms are given in coordinates x and y as $(B_{ix},\ B_{iy})$ for a common time i, while embedding coordinates take the form $(B_{ix},\ B_{(i-d)x})$ for a common component x where d is the delay length. For an n-dimensional embedding, n points with temporal separation d become an n-vector. Typically, the motivation for time series embedding is to avoid intersections. The n is chosen so the trajectory does not cross itself and this gives the number of degrees of freedom for the system. The number of degrees of freedom for turbulence would be very large but fortunately a lower dimensional embedding can be informative. An ad hoc method is developed here for determining active vs. quiet magnetic fields with $n = 2$. Additionally d is usually chosen from the mutual information or auto correlation function such that the linear component of the trajectory is neglected. Here $d = 10$ seconds (1-point separation) since quiet conditions exhibit a linear behavior traversing through a steady magnetic field configuration (e.g., *Caudal* (1986) force-balanced magnetodisc model) radially increasing or decreasing in strength.

We define a quantity from the embedding representative of magnetic activity. The many variations associated with a fluctuating time series produce many intersections. The size of the box necessary to enclose the trajectory also carries information about the range of fluctuations. The nonlinear measure of magnetic activity $\mathcal{N}$ sums all intersections individually from B_r, B_θ, and B_ϕ to give $\mathcal{N} = (number\ intersections) * \ell$ where $\ell = \ell_{r1} + \ell_{r2} + \ell_{\theta 1} + \ell_{\theta 2} + \ell_{\phi 1} + \ell_{\phi 2}$ is the sum of side lengths for the smallest rectangle enclosing each component's trajectory. Panels (c) and (d) of Figure 4.7 show the embedding for quiet and active intervals in (a) and (b), respectively.

To set numerical thresholds for active vs. quiet, histograms of $\log_{10}(\mathcal{E})$, $\log_{10}(\mathcal{N})$, and $\log_{10}(\delta B)$ are fitted with a Gaussian, although none of the measures for magnetic activity have an exact normal distribution; they are left-skewed. The thresholds are one standard deviation to the right of each distribution's peak. This semi-arbitrary threshold is motivation for choosing multiple measures of the magnetic activity to give confidence in choosing windows that lie near the threshold. Finally, the analysis requires at least one current sheet (sign change of two or more magnetic field components) to be labeled a KH active window

(*Delamere et al.*, 2011). This gives a boundary with active magnetic fields $3 \pm 0.2\%$ of the time. With respect to local time active magnetic fields occur $5 \pm 0.4\%$ of the time near the magnetopause LT < 12, $2 \pm 0.3\%$ of the time LT > 12, and $12 \pm 0.7\%$ between local times 10-12.

4.2.5.1 Cassini Heating rate density

Cassini's observed q is approximated with $k_\perp = 2\pi f/[v_{rel}\sin(\theta_{vB})]$ as given by *von Papen et al.* (2014), where f is the frequency range resolved in the power spectrum, θ_{vB} is the angle between the flow vector and magnetic field, and v_{rel} is the flow velocity relative to Cassini. These velocities can be determined using an empirically fitted radial profile (*Thomsen et al.*, 2010). For a given one-second averaged MAG time series, the one-dimensional power spectrum $P(f)$ of $\delta B_\perp$ is calculated with a Morlet Wavelet Transform (*Tao et al.*, 2015). Similarly to Section 4, $(P(f)f)^{3/2} \sim \delta B_\perp^2$ can be integrated with a factor $k_\perp$, as in Equation 4.7. The remaining factor $1/\sqrt{\mu_0^3\rho}$ gives q, with density determined by an empirical profile (*Thomsen et al.*, 2010).

Panels (a)-(c) of Figure 4.8 show the LT distribution of magnetic activity colored by q for magnetospheric windows within 100 minutes of the magnetopause. There are more points compared to Figure 4.6 because MAG data availability is far better than CAPS and every window is shown rather than averages. The q distributions are similar indicating the methods agree well. Each measure shows a clear trend of larger q for larger measure of magnetic activity, and a significant hot spot from LT $\sim 10 - 13$.

Histograms in Figure 4.9(a) show distributions of q near (100 mins) Saturn's magnetopause. The dawn and dusk sectors both have geometric mean $q \sim 2 \times 10^{-17}$ W/m^3, while active events have geometric mean $q \sim 1 \times 10^{-15}$ W/m^3. The broader dawn distribution suggests asymmetry in the heating characteristics on the dawn vs. dusk magnetopause. The red axis in Figure 4.9(a) shows the geometric mean of q as a function of time from magnetopause crossing. Average q maximizes nearest the boundary and decreases moving away.

To estimate the relevance of these events for the global energy budget, it is important to note plasma parcels near the subsolar magnetopause boundary take ~ 6 hours before being swept down-tail to exit the magnetosphere. Given $q \sim 10^{-15}$ W/m^3 present for 6 hours, plasma temperatures can change by $100s$ of eV for average Saturn parameters. This is a significant amount of heating given typical temperatures in the outer magnetosphere of $10^2 - 10^3$ eV (*Thomsen et al.*, 2010). However it is important to note that these events are an episodic spot heating. As a consequence of ideal flux circulation, it may also be true that magnetic fluctuations dissipate in the magnetosphere while plasma escapes to the solar wind.

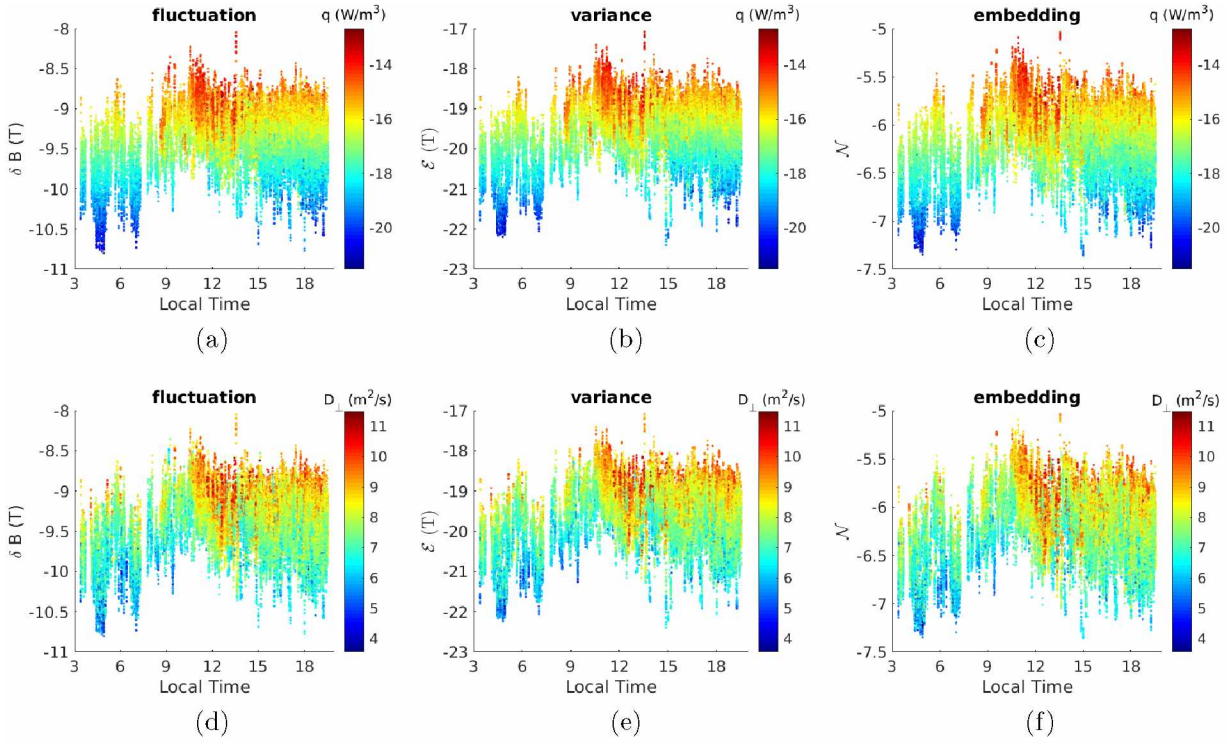

Figure 4.8: Measure of magnetic activity vs. local time for all windows within 100 minutes of magnetopause. Panels (a)-(c) are colored with $\log_{10} q$ and (d)-(f) are colored with $\log_{10} D_\perp$. The y-axes give $\log_{10} f$ for f the particular measure of magnetic activity.

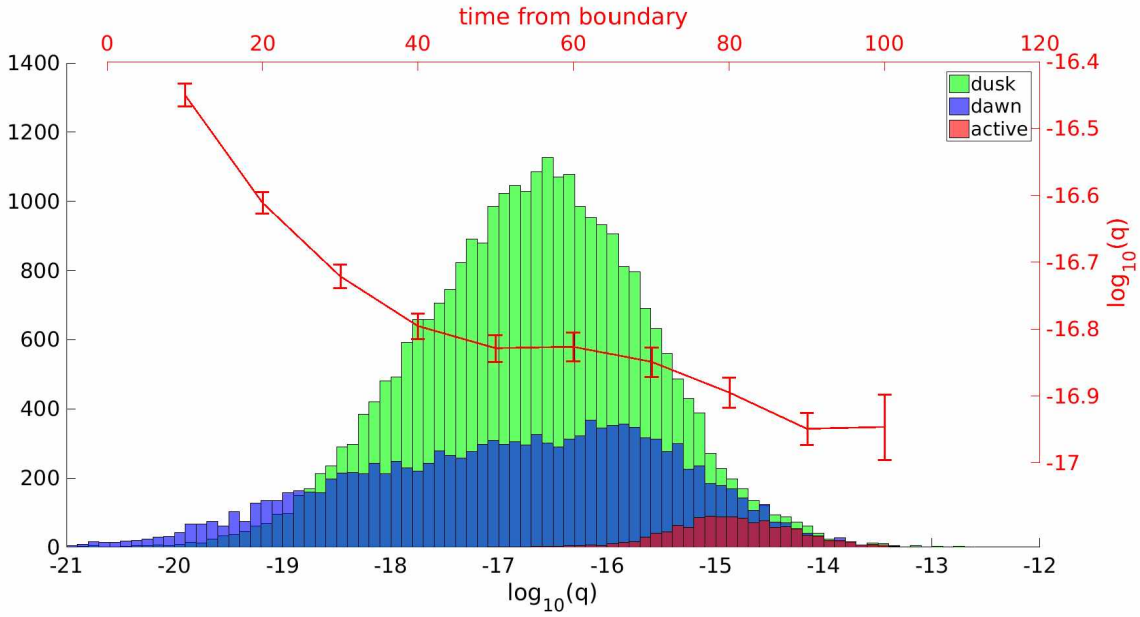

(a)

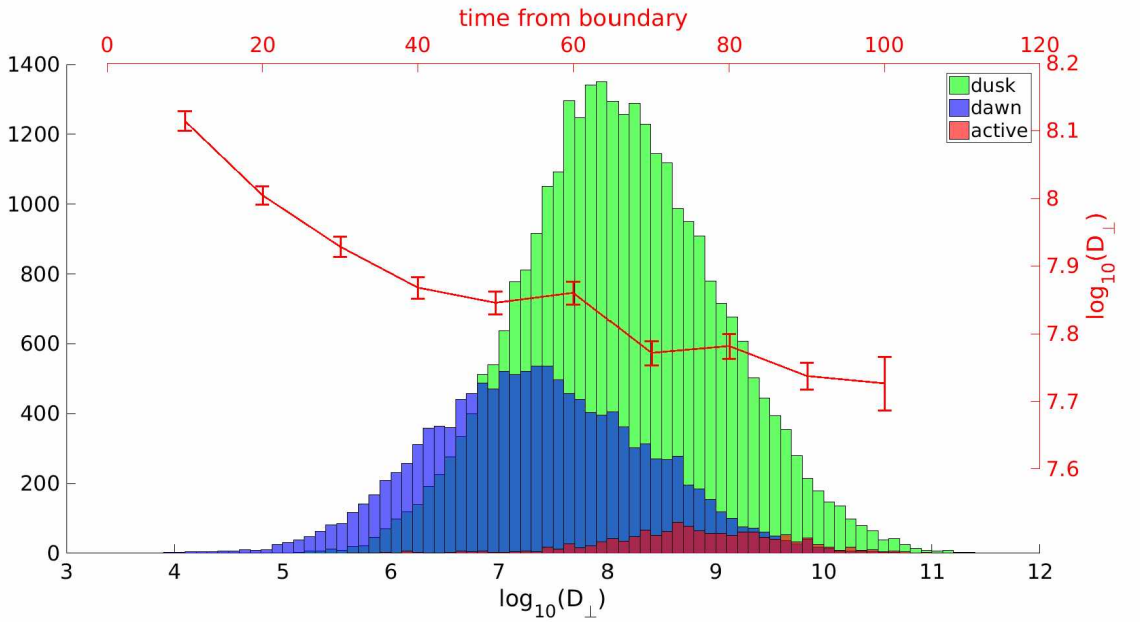

(b)

Figure 4.9: Black axes give histograms of q (a) and $D_\perp$ (b) for dawn (blue), dusk (green), and active windows (red) within 100 minutes of the magnetopause. Red axes show average with time from magnetopause crossing over all local times.

4.2.5.2 Cassini Diffusion Coefficient

To calculate $D_\perp$ in Equation 4.7, the one-dimensional Fourier power spectrum $P'(f)$ of $\delta B_{||}/B_0$ is derived from a one-second averaged MAG time series. As in Section 4, $P'(f)f \sim |\delta B_{||}/B_0|^2$. We take density and temperature profiles from *Thomsen et al.* (2010) to calculate v_A and ρ_i. Panels (d)-(f) of Figure 4.8 show the LT distribution of magnetic activity colored by $D_\perp$ for magnetospheric windows within 100 minutes of the magnetopause. The distributions are similar for each measure of magnetic activity and again there is a hot spot at the subsolar point extending down the dawn flank. This is also a feature of the terrestrial magnetopause (*Yao et al.*, 2011). There is a trend of larger $D_\perp$ for larger measure of magnetic activity, similarly to results for q.

Figure 4.9(b) shows histograms of $D_\perp$ near Saturn's magnetopause, similar to Figure 4.9(a). There is LT asymmetry, with dusk geometric mean $D_\perp \sim 1 \times 10^8$ m^2/s, and dawn geometric mean $D_\perp \sim 2 \times 10^7$. The active events have geometric mean $D_\perp \sim 7 \times 10^8$ m^2/s. It is interesting that many of the largest values for $D_\perp$ are not included in the active events, suggesting that none of the chosen measures for magnetic activity captures a strong dependence on the parallel magnetic field fluctuation. Such fluctuations in magnetic field strength may naturally occur in the high beta plasma near Saturn's magnetopause. As in panel (a), the red axis for panel (b) shows average $D_\perp$ vs. time from magnetopause boundary, which decreases moving away from the boundary. Again it is important to note enhanced transport events would be episodic. Islands of magnetospheric W^+ plasma would be formed in the magnetosheath as found 15% of the time by *Sergis et al.* (2013), which agrees with the estimated occurrence rates of active KH in the LT sector 10-12 from sections 2 and 5.

An estimate for mass transported through the boundary with $D_\perp \sim 10^9$ m^2/s can be obtained from the diffusion equation. The empirical density profile from *Thomsen et al.* (2010) can approximate $\nabla^2 n$ at $R = 25R_{Saturn}$. This is likely a bad approximation to the magnetopause density gradient, particularly within the active KH, but gives a zeroth order approximation. The resulting $\frac{\partial n}{\partial t} = 0.62$ m^{-3}s^{-1} integrated over a volume approximating the dawn-side boundary layer gives a transport rate of ~ 0.1 kg/s. This is only 0.2% of the 55 kg/s escaping the magnetosphere on average (*Neupane et al.*, 2019). Using the upper limit $D_\perp \sim 10^{10}$ m^2/s from the hybrid simulation the transport rate is still only 1 kg/s, indicating the dominant region of mass loss is down-tail. Although, the global mass budget may still depend on KHIs since they could play a role in the nonlinear development of instabilities with much sharper gradients.

4.2.6 Conclusions

Since Saturn's boundary layer width (and associated magnetopause Δv) varies, active KH vortices may be rarely observed. The dawn magnetopause has large KH growth rates so the boundary quickly diffuses into a broad layer with an uncertain lifetime. The dusk magnetopause is mostly structured by non-evolving KH waves advecting downtail rather than actively rolling-up (*Ma et al.*, 2015; *Zhang et al.*, 2018). We summarize our findings as follows:

- Reversed flows near Saturn's magnetopause indicate active KH vortices ∼14% of the time pre-noon and ∼1% post-noon. A majority of pre-noon events occur in the LT sector 10-12 (∼ 18% occurrence rate) where there can be a stationary KH vortex.
- Theoretical values for q and $D_\perp$ in hybrid simulations of the KHI using Equations 4.5 and 4.7 are $q \sim 10^{-14}$ W/m^3 and $D_\perp \sim 10^9$ m^2/s for typical Saturn parameters.
- Active magnetic fields with current sheet crossings are found on the magnetospheric side of the magnetopause boundary ∼ 5% of the time LT$>$ 12, ∼ 2% for LT$<$ 12, 12% from LT 10-12, and 3% globally.
- Active magnetic fields can be associated with q and $D_\perp$ comparable to the hybrid simulation, particularly at LT 10-12.
- Values of q and $D_\perp$ significantly above the background allows a possible identification of KH active intervals, however the high beta environment renders this method imprecise due to the background $\delta B_{||}/B_0$.
- The hot spot for large q and $D_\perp$ in the subsolar region as well as prominence of reversed flows in the LT sector 10-12 resolves the conundrum of the dawn-vs-dusk prevalence of KH waves and confirms the findings of *Ma et al.* (2015).

Future studies will correlate CAPS and MAG data given their different time resolutions and availability.

Chapter 5

Summary and Future Work

Driven magnetic reconnection is a ubiquitous process in a dynamic space plasma. This thesis has produced model-data comparisons in such environments, specifically focusing on two distinctly different problems with the common theme of twisting magnetic field lines. The hybrid fluid-kinetic model is used to explore kinetic scale processes and the patchy network of intermittent reconnection sites produced within a swirling Kelvin-Helmholtz vortex. In the MHD approximation a quasi-static evolution of the magnetic field breaks the frozen-in condition when a critical threshold for the current density and parallel electric field is reached, while remaining in an equilibrium until such a point. Although different approaches are taken for the different problems, the results of reconnection always involve mixing, energization, and observable variations in the magnetic field. These studies have come at a time where space physics is preparing to leap forward in its understanding, with missions like Magnetospheric Multi-Scale, Juno, and Parker Solar Probe producing phenomenal data in never before visited extremes and a new generation of spacecraft in the making. On the simulation side, there remains a bevy of studies to conduct using the hybrid model to understand transport and heating. We also look forward to comparisons with global MHD simulations to understand the role of the Kelvin-Helmholtz instability for the global mass and energy budgets at Jupiter and Saturn. In addition, the solar MHD model is ripe with interesting physics that has not been systematically explored. This is because the complexity of the model is atypical for reconnection studies which have mostly taken an idealized approach.

5.1 Summary of Results

5.1.1 Magnetic Connectivity in the Corona as a Source of Structure in the Solar Wind

The structure of the solar magnetic field is produced by many thousands of kilogauss flux concentrations, which, while evolving on a spectrum of temporal and spatial scales, are always responsible for topologically disconnected regions. These topological boundaries map Alfvénic perturbations from different source regions into the same vicinity. An inhomogenous photosphere implies a discontinuous perturbation at these surfaces which can drive strong field aligned and perpendicular currents. Integral properties of the magnetic field and plasma allow to identify these very thin topological boundaries. The presence of magnetic reconnection occurring on both open and closed flux in the model is confirmed from the field line integrated parallel electric field. The simulations also show strong gradients in the in-situ plasma properties which evolve on or near these flux surfaces. These boundaries represent structure which may source flux tube boundaries observed in the solar wind at 1 AU by ACE (*Borovsky*, 2008).

5.1.2 Magnetic Reconnection of Solar Flux Tubes and Reconnection Signatures in the Solar Wind

Building on the reconnection results from the first study of solar flux tubes, magnetic field lines in the vicinity of a separatrix surface were traced to determine their time-dependent connectivity. Specifically, open flux tubes exchange field lines across these boundaries implying a changing perturbation to a fluid element on open flux. The signatures of magnetic reconnection are a key component to understanding the role that magnetic topology can play in sourcing solar wind structure, since they may be observable from a remote location. The structure of the reconnection outflow has been investigated plenty in the past, however here we also include the boundaries of the bulge region that propagates ahead of the reconnection jet and find the properties remarkably similar to the edges of the jet. The two-dimensional simulations indicate that outflow boundaries will contain a layer satisfying the Walén relation and also separate a total pressure balanced plasma with smaller density and thermal pressure. These changes depend on the asymmetries and other specifics of the reconnection layer, however careful analysis of a large number of solar wind current sheets indicates that many of them are consistent with this picture. While the location of the X-line for these reconnection boundaries can not be determined, diamagnetic drift stabilization suppresses reconnection in the typically plasma $\beta > 1$ conditions near Earth, so that the reconnection site is likely closer to the sun or in the corona for many of the events.

5.1.3 Local Time Asymmetry of Saturn's Magnetosheath Flows

The classic picture of a magnetopause that is a hard boundary to the solar wind is thrown away, at least at Saturn, where Kelvin-Helmholtz waves are driven by intense shear flows. Intermittent reconnection allows the solar wind to grab hold of the magnetosphere and facilitate two way transport of mass and momentum. It is surprising that no previous studies have analyzed the magnetosheath flows with respect to local time, considering the significant asymmetry in the magnitude of the flow shear. We have been able to do such a study thanks to the grueling hand-identification of the magnetopause boundary in both particle and magnetic field data throughout 7+ years of Cassini orbits. That we find significantly reduced flows in the dawn-side magnetosheath is a smoking gun for the action of Kelvin-Helmholtz.

5.1.4 Identifying Active Kelvin-Helmholtz Vortices on Saturn's Magnetopause Boundary

Many previous studies which have attempted to identify Kelvin-Helmholtz have confoundingly concluded that they are more prevalent on the dusk portion of Saturn's magnetopause as compared to the dawn. Not only is this contrary to expectation, where the Kelvin-Helmholtz growth rate and occurrence frequency should be largest in the region of maximum flow shear, but is also contrary to our asymmetric magnetosheath flow results. By more carefully analyzing flows near the magnetopause, the occurrence frequency of reversed flows gives a picture of Kelvin-Helmholtz that agrees with expectation. We have also produced a similar result by considering the local time distribution of active magnetic fields with current sheet crossings, as this is the signature we can expect a spacecraft to see from the hybrid simulation. It turns out that a more precise definition of Kelvin-Helmholtz is necessary to identify these waves, since non-evolving Kelvin-Helmholtz structures can often be found advecting down the dusk flank. The magnetic field fluctuations associated with the non-linear rollup phase of the Kelvin-Helmholtz instability can be responsible for significant plasma heating and diffusive transport. It was hoped that these properties would allow an unambiguous identification of active Kelvin-Helmholtz, but our results indicate this is not the case because the high plasma β environment at Saturn is naturally abundant with magnetic field fluctuations. However, it is true that events with current sheet crossings and fluctuating magnetic fields have values for the heating rate density and diffusive transport coefficient which are similar to the hybrid simulation.

5.2 Future Work

5.2.1 Transport in Three-Dimensional Kelvin-Helmholtz Simulations

Recent work by *Ma et al.* (Submitted - 2019) has produced very interesting results concerning the mechanism of transport in hybrid simulations compared with Hall MHD simulations. *Ma et al.* (Submitted - 2019) initialized two-dimensional simulations of the KHI using very similar parameters in the two different frameworks. While both simulations produced essentially the same amount of transport, the Hall MHD simulation does so through the production of large magnetic islands while the hybrid simulations show transport that is primarily facilitated by diffusion. The obvious next step is to perform three-dimensional simulations to make comparisons between the hybrid simulation and Hall MHD. The patchy network of intermittent reconnection sites produced in the hybrid simulation is particularly important in three-dimensions, and may shed further light on the specific physical mechanism driving transport.

5.2.2 Reconnection Signatures in the Solar Wind

Not included in Chapter 3 are examples for which both sides of the outflow boundary can be identified. An event of this type is shown in Figure 5.1. The spacecraft coordinate system has been used here, but a rotation into a coordinate system defined by the directions of maximum, intermediate, and minimum variance shows anti-parallel components of the magnetic field at both strong rotations. Also for this case plasma $\beta \sim 5$ suggesting a reconnection site much closer to the sun. We have identified at least 20 such events, which, for the analysis in Chapter 3, we consider each boundary individually. However as Chapter 3 mentions, such events allow a determination of the B_n component with the correct normalization, as well as an estimate for the distance to the X-line. In the future we could consider a number of case studies and also compile more events of this type from the recent MMS data.

5.2.3 Evolution of the Solar Wind Throughout the Heliosphere

The incredibly close perihelion for Parker Solar Probe (see Figure 5.2) provides a key platform for understanding the evolution of solar wind structure from the sun to 1 AU and beyond. These observations are important since they allow to determine better input parameters for modeling in an extremely difficult to measure plasma environment. In conjunction with remote solar observations (SOHO, SDO) and solar wind monitoring (ACE, DSCOVR, STEREO) a sequence of observations can track solar wind flow throughout the heliosphere.

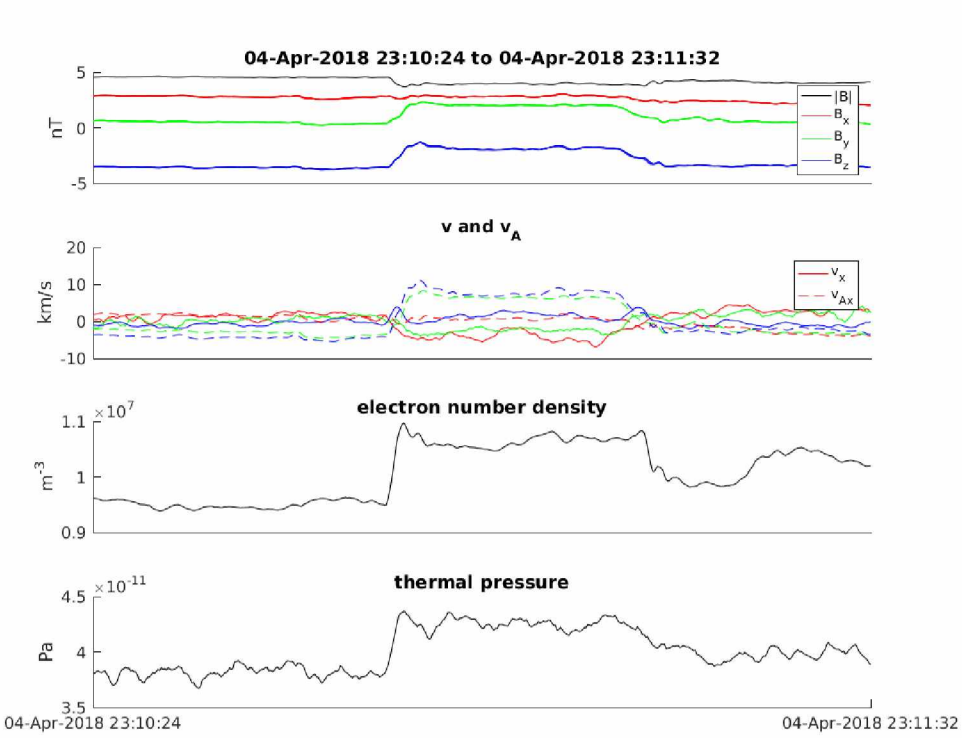

Figure 5.1: Solar wind current sheet example where both sides of the outflow boundary can be identified.

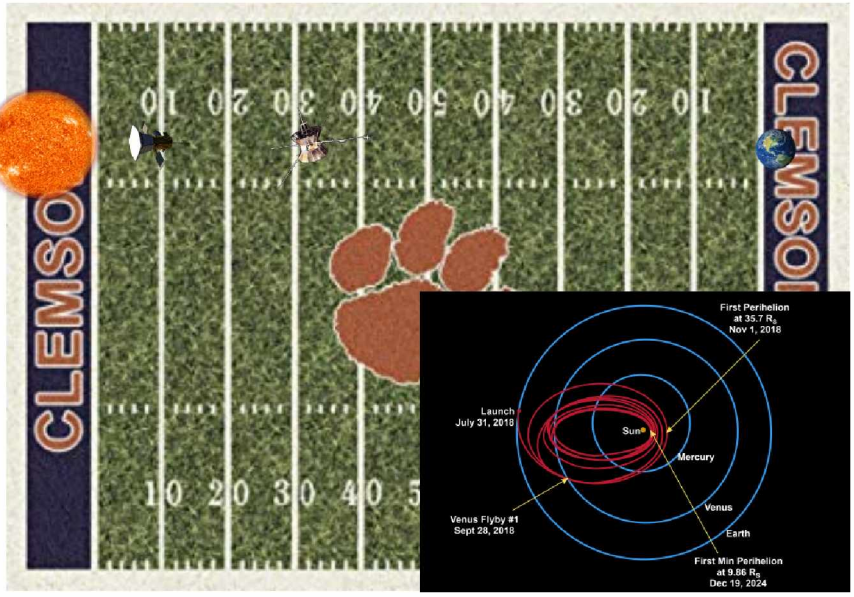

Figure 5.2: Relative distances to the sun for Parker Solar Probe's closest approach (3 yards), the Helios II spacecraft on closest approach (30 yards), and Earth (100 yards). Inset shows the evolution for the orbit of Parker Solar Probe. *Inset reproduced from http://parkersolarprobe.jhuapl.edu/.*

"Probe", being the nomenclature adopted in the community, is much more likely to observe reconnection originating in the corona and will allow to understand how much the reconnection contributes to the nonadiabatic heating of the solar wind. We can additionally compare the structure of current sheets observed in the corona with our observations by MMS at 1 AU. It would also be interesting to perform a mapping of the electric current observed by Parker Solar Probe in relation to the topological boundaries of the solar magnetic field. Building on the theme of solar wind evolution throughout the heliosphere, the Juno spacecraft recorded solar wind data during its interplanetary cruise, which can also be used for comparison with MMS and Parker Solar Probe observations. Ultimately, space weather forecasting can become a sound science using a carefully constructed hierarchy of modeling and data from the sun to 1 AU.

Appendix A: Growth Rate of the Kelvin-Helmholtz Instability

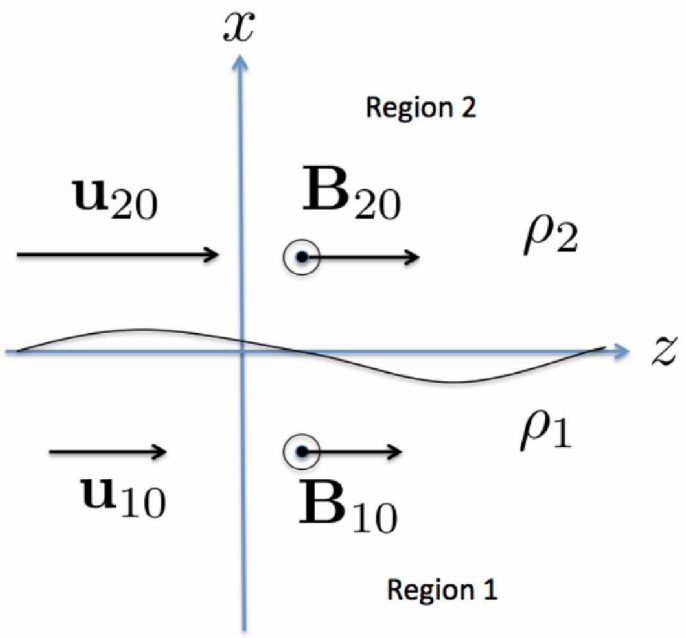

Figure A.1: Coordinate system for the Kelvin-Helmholtz instability.

First we need the momentum equation

$$\rho\Big(\frac{\partial \mathbf{u}}{\partial t} + \mathbf{u}\cdot\nabla\mathbf{u}\Big) = \frac{1}{\mu_0}(\nabla\times\mathbf{B})\times\mathbf{B} - \nabla p \tag{1}$$

and Faraday's Law

$$\frac{\partial \mathbf{B}}{\partial t} = \nabla\times(\mathbf{u}\times\mathbf{B}). \tag{2}$$

Now linearize using the perturbation quantities

$$p = p_0 + p_1$$

$$\mathbf{B} = \mathbf{B_0} + \mathbf{B_1}$$
$$\mathbf{u} = \mathbf{u_0} + \frac{\partial \mathbf{x}}{\partial t}$$

where the surface wave takes the form

$$\mathbf{B_1} \sim e^{-k_x|x| - i(k_y y + k_z z - \omega t)}$$

so that upon neglecting the nonlinear terms equations (1) and (2) can be written

$$\rho_0 \frac{\partial^2 \mathbf{x}}{\partial^2 t} = \frac{1}{\mu_0}(\nabla \times \mathbf{B_1}) \times \mathbf{B_0} - \nabla p_1 \tag{3}$$

$$\frac{\partial \mathbf{B_1}}{\partial t} = \nabla \times \Big(\frac{\partial \mathbf{x}}{\partial t} \times \mathbf{B_0}\Big). \tag{4}$$

We can integrate (4) to obtain

$$\mathbf{B_1} = \nabla \times (\mathbf{x} \times \mathbf{B_0}) \tag{5}$$

and then expand the quantities

$$(\nabla \times \mathbf{B_1}) \times \mathbf{B_0} = \mathbf{B_1} \times (\nabla \times \mathbf{B_0}) - \nabla(\mathbf{B_1} \cdot \mathbf{B_0}) + (\mathbf{B_1} \cdot \nabla)\mathbf{B_0} + (\mathbf{B_0} \cdot \nabla)\mathbf{B_1} \tag{6}$$

$$\nabla \times (\mathbf{x} \times \mathbf{B_0}) = \mathbf{x}(\nabla \cdot \mathbf{B_0}) - \mathbf{B_0}(\nabla \cdot \mathbf{x}) + (\mathbf{B_0} \cdot \nabla)\mathbf{x} - (\mathbf{x} \cdot \nabla)\mathbf{B_0} \tag{7}$$

which can be simplified for the case of incompressible flow ($\nabla \cdot \mathbf{u} = 0$) and a uniform $\mathbf{B_0}$

$$(\nabla \times \mathbf{B_1}) \times \mathbf{B_0} = (\mathbf{B_0} \cdot \nabla)\mathbf{B_1} - \nabla(\mathbf{B_1} \cdot \mathbf{B_0}) \tag{8}$$

$$\nabla \times (\mathbf{x} \times \mathbf{B_0}) = (\mathbf{B_0} \cdot \nabla)\mathbf{x}. \tag{9}$$

Substituting (8) into (3)

$$\rho_0 \frac{\partial^2 \mathbf{x}}{\partial^2 t} = \frac{1}{\mu_0}[(\mathbf{B_0} \cdot \nabla)\mathbf{B_1} - \nabla(\mathbf{B_1} \cdot \mathbf{B_0})] - \nabla p_1 \tag{10}$$

which can be rewritten

$$\rho_0 \frac{\partial^2 \mathbf{x}}{\partial^2 t} = \frac{1}{\mu_0}(\mathbf{B_0} \cdot \nabla)\mathbf{B_1} - \nabla\Big(p_1 + \frac{\mathbf{B_1} \cdot \mathbf{B_0}}{\mu_0}\Big) \tag{11}$$

and we can also substitute (9) into (5) to obtain

$$\mathbf{B_1} = (\mathbf{B_0} \cdot \nabla)\mathbf{x}. \tag{12}$$

Now we define $\tilde{p} = p_1 + \frac{\mathbf{B_1}\cdot\mathbf{B_0}}{\mu_0}$ and (11) can be written

$$\rho_0 \frac{\partial^2 \mathbf{x}}{\partial^2 t} = \frac{1}{\mu_0}(\mathbf{B_0}\cdot\nabla)(\mathbf{B_0}\cdot\nabla)\mathbf{x} - \nabla\tilde{p}. \tag{13}$$

Assuming plane wave solutions such that $\partial/\partial t \to -i\omega$ and $\nabla \to i\mathbf{k}$

$$\Big[\omega^2\rho_0 - \frac{1}{\mu_0}(\mathbf{B_0}\cdot\mathbf{k})^2\Big]\mathbf{x} = \nabla\tilde{p} \tag{14}$$

and since $\mathbf{v_A} = \mathbf{B}/\sqrt{\mu_0\rho_0}$ we can write

$$\rho_0\Big[\omega^2 - (\mathbf{v_A}\cdot\mathbf{k})^2\Big]\mathbf{x} = \nabla\tilde{p}. \tag{15}$$

To find $\nabla\tilde{p}$ we must go back to Faraday's law which can be written

$$\frac{\partial \mathbf{B}}{\partial t} = \nabla\times(\mathbf{u}\times\mathbf{B}) = (\mathbf{B}\cdot\nabla)\mathbf{u} - (\mathbf{u}\cdot\nabla)\mathbf{B}$$

and linearized with $\frac{\partial}{\partial t} \to -i\omega\prime$ for a doppler shifted frequency

$$-i\omega\prime\mathbf{B}_1 = i(\mathbf{B}_0\cdot\mathbf{k})\mathbf{u}_1 - i(\mathbf{u}_0\cdot\mathbf{k})\mathbf{B}_1.$$

Since $\omega\prime - \mathbf{u}_0\cdot\mathbf{k} = \omega$ we have

$$\omega\mathbf{B}_1 = -(\mathbf{B}_0\cdot\mathbf{k})\mathbf{u}_1$$

and we can rewrite (11)

$$\rho_0\frac{\partial \mathbf{u}_1}{\partial t} = \frac{-1}{\mu_0}(\mathbf{B}_0\cdot\nabla)(\mathbf{B_0}\cdot\mathbf{k})\mathbf{u}_1 - \nabla\tilde{p}$$

$$-i\omega\rho_0\mathbf{u}_1 = -i\frac{(\mathbf{B}_0\cdot\mathbf{k})^2}{\mu_0\omega}\mathbf{u}_1 - \nabla\tilde{p}$$

so the perturbed pressure is

$$\nabla\tilde{p} = i\Big[\omega\rho_0 - \frac{(\mathbf{B}_0\cdot\mathbf{k})^2}{\mu_0\omega}\Big]\mathbf{u}_1$$

which we can take the divergence of

$$\nabla^2\tilde{p} = i\Big[\omega\rho_0 - \frac{(\mathbf{B}_0\cdot\mathbf{k})^2}{\mu_0\omega}\Big](\nabla\cdot\mathbf{u}_1)$$

and since $\nabla\cdot\mathbf{u}_1 = 0$ we have $\nabla^2 \to 0$ which is $k_x^2 - k_y^2 - k_z^2 = 0$ and the displacement normal to the boundary is

$$x = \frac{\pm k_x \tilde{p}}{\rho_0 \Big[\omega^2 - (\mathbf{v_A} \cdot \mathbf{k})^2\Big]}. \tag{16}$$

Now we consider the above for two different sides of the shear flow layer

$$x_1 = \frac{-k_x \tilde{p_1}}{\rho_{01} \Big[\omega^2 - (\mathbf{v_{A1}} \cdot \mathbf{k})^2\Big]}. \tag{17}$$

$$x_2 = \frac{k_x \tilde{p_2}}{\rho_{02} \Big[(\omega - \mathbf{k} \cdot (\mathbf{u_{10}} - \mathbf{u_{20}}))^2 - (\mathbf{v_{A2}} \cdot \mathbf{k})^2\Big]}. \tag{18}$$

where the frequency in region 2 must be doppler shifted by the velocity change across the shear flow layer. The displacement as well as the perturbed pressures must be continuous across the layer, giving the dispersion relation

$$\rho_{01}[\omega^2 - (\mathbf{k} \cdot \mathbf{v_{A1}})^2] + \rho_{02}[(\omega - \mathbf{k} \cdot (\mathbf{u_{10}} - \mathbf{u_{20}}))^2 - (\mathbf{v_{A2}} \cdot \mathbf{k})^2] = 0. \tag{19}$$

Solving the quadratic for ω, we obtain

$$\omega = \alpha_2 \mathbf{k} \cdot (\mathbf{u_{20}} - \mathbf{u_{10}}) \pm \Big(\alpha_1 (\mathbf{k} \cdot \mathbf{v_{A1}})^2 + \alpha_2 (\mathbf{k} \cdot \mathbf{v_{A2}})^2 - \alpha_1 \alpha_2 [\mathbf{k} \cdot (\mathbf{u_{20}} - \mathbf{u_{10}})]^2\Big)^{1/2}$$

with $\alpha_i = \rho_{0i}/(\rho_{01} + \rho_{02})$. We can see that Kelvin-Helmholtz are stabilized for

$$\alpha_1 (\mathbf{k} \cdot \mathbf{v_{A1}})^2 + \alpha_2 (\mathbf{k} \cdot \mathbf{v_{A2}})^2 > \alpha_1 \alpha_2 [\mathbf{k} \cdot (\mathbf{u_{20}} - \mathbf{u_{10}})]^2$$

and finally for a shear layer unstable to Kelvin-Helmholtz waves the growth rate is

$$\gamma = (\alpha_1 \alpha_2 [\mathbf{k} \cdot (\mathbf{u_{20}} - \mathbf{u_{10}})]^2 - \alpha_1 (\mathbf{k} \cdot \mathbf{v_{A1}})^2 - \alpha_2 (\mathbf{k} \cdot \mathbf{v_{A2}})^2)^{1/2}$$

which is similar to the result by *Chandrasekhar* (1961) who considered a uniform magnetic field.

Appendix B : Diffusive Transport Coefficient for Kinetic Alfvén Waves

Here we derive equation 4.7, which quantifies the turbulent transport of plasma driven by the so-called transit-time damping process as described in Chapter 4.

We begin with the $j = 3$ term from Equation (1) of *Chaston et al.* (2009)

$$D_\perp = \sqrt{\frac{\pi}{8}} \sum_k \frac{1}{|k_{||}| v_{ti}} \left| \frac{E_Y(k)}{B_0} \right|^2 \left(2 \frac{\sigma^2 \eta^2}{k_\perp^2 \rho_i^2} \right) 2 \int_0^\infty x^3 J_1(\lambda x) J_1(\lambda x) e^{-x^2 - \zeta^2} dx$$

where $\lambda = k_\perp \rho_i$ and $\zeta = \omega / \sqrt{2} k_{||} v_{ti}$. The Bessel functions of the first kind can be written using a series expansion around $\lambda x = 0$

$$J_\alpha(\lambda x) = \sum_{m=0}^{\infty} \frac{(-1)^m}{m! \Gamma(m + \alpha + 1)} \left(\frac{\lambda x}{2} \right)^{2m+\alpha}$$

so in the limit $k_\perp \rho_i \to 0$ the $m = 0$ term dominates and we have

$$J_1(\lambda x) \approx \frac{1}{\Gamma(2)} \frac{\lambda x}{2} = \frac{\lambda x}{2}.$$

Now we simplify the diffusion coefficient

$$D_\perp = \sqrt{\frac{\pi}{8}} \sum_k \frac{1}{|k_{||}| v_{ti}} \left| \frac{E_Y(k)}{B_0} \right|^2 \sigma^2 \eta^2 e^{-\zeta^2} \int_0^\infty x^5 e^{-x^2} dx$$

perform the substitution $x^2 = y$ and the integral

$$\int_0^\infty x^5 e^{-x^2} dx = \int_0^\infty \frac{y^2}{2} e^{-y} dy = 1.$$

For $k_\perp \rho_i \to 0$, the kinetic Alfvén wave dispersion relation yields $\omega \approx k_{||} v_A$ so we can write

$$\zeta^2 = \frac{\omega^2}{2 k_{||}^2 v_{ti}^2} \approx \frac{v_A^2}{2 v_{ti}^2} = \frac{1}{\beta}$$

where β is the plasma beta and the diffusion coefficient is

$$D_\perp = \sqrt{\frac{\pi}{8}} \sum_k \frac{1}{|k_{||}| v_{ti}} \left| \frac{E_Y(k)}{B_0} \right|^2 \sigma^2 \eta^2 e^{-1/\beta}.$$

Finally, we can substitute $|E_Y(k)/B_0|^2 \sigma^2 \eta^2 = |\delta B_{||}(k)/B_0|^2 v_A^2 k_\perp^2 \rho_i^2$ and we have the result

$$D_\perp = \sqrt{\frac{\pi}{8}} \sum_k \frac{v_A^2}{|k_{||}| v_{ti}} \left| \frac{\delta B_{||}(k)}{B_0} \right|^2 k_\perp^2 \rho_i^2 e^{-1/\beta}$$

which is equation 4.7 for $v_{ti} \approx v_A$. Note that the sum over k applies to the $k_\perp$ where $k_\perp \rho_i$ is small. In our case we take $k_\perp \rho_i < 1$.

Appendix C: Three-dimensional hybrid simulation of viscous-like processes at Saturn's magnetopause boundary

Abstract[1]

Saturn's magnetosheath flows exhibit significant dawn/dusk asymmetry. The dawnside flows are reduced from expectation, suggesting significant momentum transport through the magnetopause boundary where the flow shear is maximized. It has been suggested that the solar wind interaction with the giant magnetospheres is, in fact, dominated by a viscous-like interaction governed by the Kelvin-Helmholtz instability. In three dimensions, the Kelvin-Helmholtz instability can generate small-scale and intermittent magnetic reconnection due, in part, to a twisted magnetic field topology. The net result is a field line threading of the magnetopause boundary and the generation of Maxwell shear stresses. Here we present three-dimensional hybrid simulations (kinetic ions and massless fluid electrons) of conditions similar to Saturn's dawnside magnetopause boundary to quantify the viscous-like, tangential drag. Using model-determined momentum fluxes, we estimate the effect on dawnside sheath flows and find very good agreement with observations.

Introduction

The solar wind interaction with Saturn's magnetosphere involves substantial tangential drag at the dawnside magnetopause boundary (*Burkholder et al.*, 2017). In collisionless plasmas, the tangential drag can be described as viscous-like (*Axford and Hines*, 1961); however, the specific physical mechanisms that allow momentum transport at the magnetopause boundary are poorly understood. The strong flow shears on the dawnside magnetopause boundary suggest that the Kelvin-Helmholtz (KH) instability may play a key role (*Masters et al.*, 2010;

[1]Manuscript authors: P. A. Delamere, B. L. Burkholder, X. Ma

Delamere et al., 2011; *Masters et al.*, 2012; *Wilson et al.*, 2012; *Masters et al.*, 2014; *Ma et al.*, 2015). Recent studies to quantify sheared flow-driven transport have demonstrated that in three dimensions the interaction between the Kelvin-Helmholtz instability and magnetic reconnection can lead to significant mass transport facilitated through intermittent, mid-latitude reconnection (*Ma et al.*, 2017). Typically the equatorial regions are KH unstable, while mid- and high-latitude regions are KH stable (*Desroche et al.*, 2013). This means that interplanetary magnetic field (IMF) and magnetospheric magnetic fields are twisted locally, forming a pair of strong guide field (component) reconnection sites at mid latitudes. Reconnection can occur asynchronously, generating open flux; however, *Ma et al.* (2017) showed in three dimensional magnetohydrodynamic simulations that double (synchronous) reconnection dominated. The synchronous reconnection allows for plasma transport through flux tube exchange between the reconnection sites. *Ma et al.* (2017) found diffusion coefficients under northward interplanetary magnetic field conditions at Earth to be as high as 10^{10} m^2/s.

Recently, global MHD simulations have demonstrated a viscous-like interaction at Saturn's dawnside magnetopause boundary. Using the Block Adaptive Tree Solar wind Roe-type Upwind Scheme (BATS-R-US) 3-D MHD model, *Sulaiman et al.* (2017) demonstrated a dawn-dusk asymmetry in Saturn's sheath flows immediately adjacent to the magnetopause boundary with terminator flank values approaching 50% of the solar wind speed, but with the dawn side ($\sim$ 10 local time) experiencing roughly a factor of two reduction in flow speed compared to the dusk ($\sim$ 14 local time). Similarly, using the multi-fluid, Lyon-Fedder-Mobarry (MFLFM) 3-D MHD model for Jupiter, *Zhang et al.* (2018) showed an even larger (3$\times$) asymmetry at the same 10 and 14 local time locations. Using sheath flows derived from the Cassini Plasma Spectrometer instrument, *Burkholder et al.* (2017) showed that, on average, the dawn-sector is reduced by a factor < 2 compared with the dusk sector immediately adjacent to the magnetopause boundary; however, there are instances where the asymmetry exceeds 3$\times$, indicating substantial variability. The average reduction in dawnside flow (compared with dusk) for all data points taken within 500 minutes of the magnetopause boundary crossing was 55 km/s. Assuming a spacecraft velocity of 6 km/s and a static magnetopause boundary location, this corresponds to a region of roughly 3 R_S (Saturn radii). A corresponding region inside of the bow shock shows dawn-dusk symmetry.

While the global simulations appear to capture the dawn-dusk asymmetry, there remains the issue of the specific physical mechanism responsible for the momentum transport. On relatively coarse simulation grids, the global simulations are subject to numerical diffusion, yielding an effective viscosity. While the numerics may capture the qualitative nature of the interaction, an elucidation of the specific physical mechanisms is lacking. It is the intent of

this paper to demonstrate the momentum transport mechanism using high resolution three-dimensional (3-D) hybrid simulations of Saturn's dawnside magnetopause boundary. Specifically, we initialize a local simulation with parameters representative of Saturn's dawnside magnetopause and directly calculate the momentum transport under a variety of conditions. We find that momentum transport is dominated by off-diagonal (shear stresses) terms in the Maxwell and Reynolds stress tensors. These terms are often comparable and we will show that the momentum transport is consistent with observations.

The results of this study have broad application to dawn/dusk asymmetries in Jupiter's magnetosphere and the ongoing Juno mission. Comparative studies are also directly relevant to the viscous-like processes at Earth's magnetopause boundary.

Hybrid Simulation

The hybrid code (kinetic ions and massless fluid electrons) was first proposed by *Harned* (1982), and the particular algorithms for our code were developed by *Swift* (1995, 1996) and *Delamere et al.* (1999); *Delamere* (2009). The code assumes quasineutrality, and is nonradiative. The Lorentz force equation is solved following the Boris method (*Boris*, 1970; *Birdsall and Langdon*, 1991). The electric field and magnetic fields are calculated on a Yee grid (*Yee*, 1966), ensuring easy curl calculations while maintaining a divergence-free magnetic field. The magnetic field equations are updated with a second-order, predictor-corrector method. Specifically, the particles are advanced by the ion equation of motion $m_i \frac{d\mathbf{v}_i}{dt} = q(\mathbf{E} + \mathbf{v}_i \times \mathbf{B})$ where $\mathbf{v}_i$ is the ion particle velocity, $\mathbf{E}$ is the electric field, $\mathbf{B}$ is the magnetic field, m_i is the ion mass, and q is the elementary charge. The massless electron momentum equation is used to find the electric field, $\mathbf{E} = -\mathbf{u}_e \times \mathbf{B} - \nu(\mathbf{u}_e - \mathbf{u}_i) - \nabla P_e/(nq)$ where $\mathbf{u}_e$ and P_e are the electron flow velocity and thermal pressure and ν is the electron-ion collision frequency. The electron fluid is assumed to be isothermal such that $\nabla P_e = T_e \nabla n$. Ampere's law is $\mathbf{u}_e = \mathbf{u}_i - \frac{1}{\mu_o n q} \nabla \times \mathbf{B}$ where $\mathbf{u}_i$ is the ion bulk flow velocity determined with standard particle-in-cell shape functions (i.e., particle to grid weighting). The magnetic field is advanced from Faraday's law.

We note that electron pressure effects can be captured by the hybrid simulation to model kinetic Alfvén waves (KAW). For instance, in the high electron beta approximation, the dispersion relation for the KAW is $\omega^2 \approx k_\parallel^2 v_A^2 \left[1 + (1 + T_e/T_i)\, k_\perp^2 \rho_i^2\right]$ where ρ_i is the ion Larmor radius, and v_A is the Alfvén speed. In addition, at ion inertial scales the kinetic Alfvén mode resolves the Alfvén and ion-ion hybrid resonances of the fast magnetosonic/whistler branch. The hybrid code captures kinetic aspects of magnetopause boundary processes including mode conversion of compressional fast mode waves to KAWs.

Table C.1: Simulation parameters

mass, (AMU)	1
density, n_p (10^6 m^{-3})	0.4
mass density, ρ_o (10^{-22} kg m^{-3})	6.7
ion inertial length, c/ω_{pi} (km)	360
magnetic field, B_0 (nT)	5
Alfvén speed, v_A (km/s)	173
plasma β	1
initial in-plane magnetic field, B_{x0} (nT)	0.2
magnetic shear profile	$B_{x0}\tanh[(z-z_0)/L_0]$
velocity shear layer profile	$0.8v_A\tanh[(z-z_0)/L_0]$
scale length of shear profile, L_o	1.0 c/ω_{pi}
grid resolution	0.5 c/ω_{pi}
electron temperature (eV)	10

The three-dimensional simulations used in this study follow from the two-dimensional simulations of KH by *Delamere et al.* (2011) where the magnetic field was primarily in the ignorable (y) direction. Here we expand the simulation domain along the magnetic field y direction, and include a small magnetic field component in the flow shear plane (xz). The x and y boundary conditions are periodic. The z boundary is open with $\partial_z = 0$. The flow shear profile is given by $0.8v_A\tanh[(z-z_0)/L_0]$, where v_A is the magnetosheath Alfvén velocity and L_0 is the scale of the velocity jump. The magnetic field is nearly parallel with a small sheared in-plane B_x component. Table C.1 summarizes our baseline parameters that are representative of Saturn's dawnside magnetopause boundary. In this paper we only consider the thermal plasma (protons only) as a baseline case. A more realistic simulation for future study would include heavy ions (*Delamere et al.*, 2011) and the superthermal population (*Sergis et al.*, 2013). We anticipate that heavy and/or superthermal ions will increase diffusive transport, potentially enhancing the viscous-like interaction. We use a plasma $\beta \sim 1$ following observations of the thermal plasma (*Wilson et al.*, 2012) and a grid resolution of 0.5 c/ω_{pi}, where c/ω_{pi} is the ion inertial length. Under these conditions the proton thermal gyromotion is resolved.

Results

Figure C.1 shows an example from a 3-D simulation at $t = 88$ (Ω_i^{-1}) . The color slices in the xz plane show particle mixing. Particles are initialized with values of 0 (blue) or 1 (red) depending on location with respect to the velocity shear boundary and thus intermediate colors indicated the extent of mixing. The KH vortices quickly mix the plasma (e.g., "superdiffu-

sion" described by *Cowee et al.* (2010)) due to large ion gyroradius effects and relatively thin boundaries. The grey isosurface indicates the 50% mixing boundary and serves as a proxy for the distorted magnetopause boundary. Magnetic field lines (colored by local mixing) are shown, traced from the bottom to top boundary. The variation in the y direction is evident as is the twisting of the magnetic field. The patchy red isosurfaces indicate regions with parallel electric fields and thus regions where strong guide field/component reconnection is occurring.

Hybrid simulations of the KH instability are self seeding. That is, the surface waves grow from the random fluctuations associated with coarse particle statistics and typically appear initially at the shortest wavelength resolved by the grid ($\sim 1.5\ c/\omega_{pi}$). The fastest growing mode in a compressible plasma ranges between $k_x L_0$ and $2k_x L_0$, or 6 to 12 c/ω_{pi} (*Miura and Pritchett*, 1982). Larger wavelengths have lower growth rates, but larger amplitudes, resulting in an inverse cascade to larger scales (*Delamere et al.*, 2011). Figure C.2 shows a power spectrum of perpendicular (i.e., B_x, B_z) magnetic field fluctuations at $t = 192\ \Omega_i^{-1}$. The dotted vertical line corresponds to $k_x = \pi/(c/\omega_{pi})$. The red line has a spectral index of -5/3 and the blue line has a spectral index of -8/3 consistent with a turbulent cascade in the respective inertial and dissipative ranges (*Galtier et al.*, 2005). Turbulent magnetic fluctuations are seen throughout Saturn's magnetosphere (*von Papen et al.*, 2014; *Kaminker et al.*, 2017), and KH-related ion heating could be an important aspect of boundary layer processes.

The phase of the surface waves also varies along the magnetic field due to the stochastic nature of the initial perturbation. Figure C.3 shows the xy plane taken from the center of flow shear region at $t = 64\ \Omega_i^{-1}$, illustrating the field-aligned structure of B_x, u_x, and the particle mixing. A surface wave that is 180° out of phase with a wave in another region will locally twist the magnetic field, potentially leading to strong guide field reconnection. The reconnection process is similar to the double reconnection process discussed by *Ma et al.* (2017) for the KH instability at Earth. However, in this case reconnection can occur in many locations if $k_\parallel$ is large. Due to the limited box size, the simulations eventually saturate at an $m = 1$ mode and the parallel dimension can also be considered ignorable. In reality, the KH waves can continue to grow and $k_\parallel$ is determined, in part, by the extent of the KH unstable region of the magnetopause boundary (*Desroche et al.*, 2013).

An estimate of the momentum transfer can be made by considering the flux conservative form of the momentum equation in steady state

$$\frac{\partial \rho \mathbf{u}}{\partial t} + \nabla \cdot \left[\rho \mathbf{u}\mathbf{u} + \mathbf{P} + \frac{B^2}{2\mu_o}\mathbf{I} - \frac{\mathbf{B}\mathbf{B}}{\mu_o} \right] = 0. \tag{20}$$

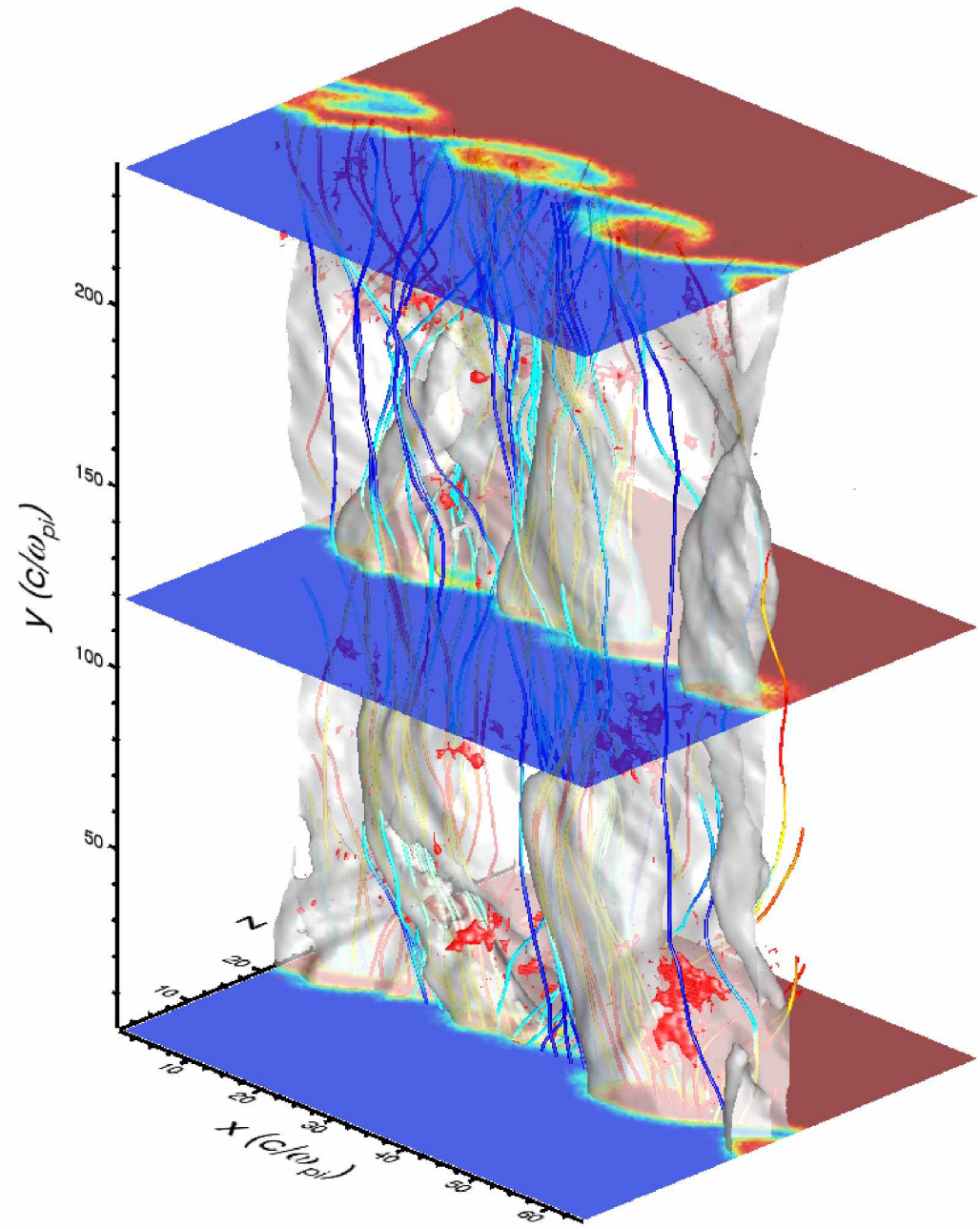

Figure C.1: Results from the 3-D hybrid KH simulation at $t = 88$ (Ω_i^{-1}). The color slices indicate particle mixing, the grey surface is the 50% mixing boundary (i.e., magnetopause), the red isosurfaces are regions of parallel electric fields, and the sample magnetic field lines are colored by particle mixing.

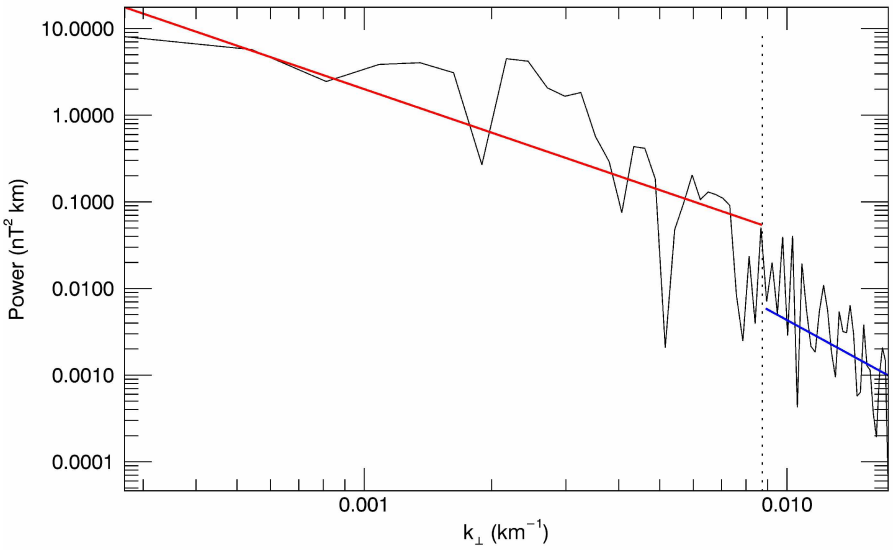

Figure C.2: Power spectrum of magnetic field fluctuations in the central vortex region at $t = 152$ (Ω_i^{-1}). The dotted vertical line corresponds to $k_\perp = \pi/(c/\omega_{pi})$. The red line has a spectral index of -5/3 and the blue line has a spectral index of -8/3.

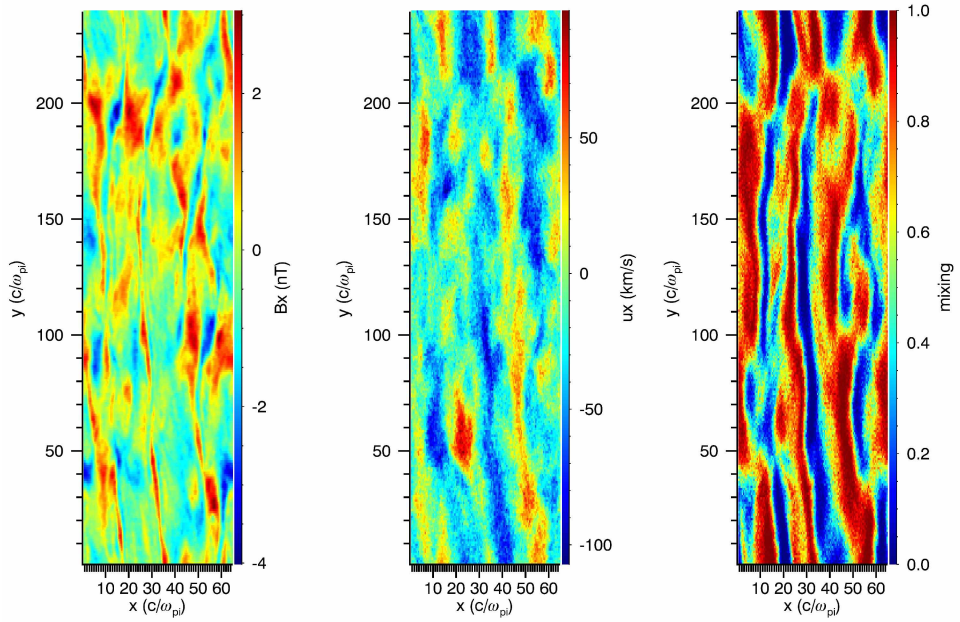

Figure C.3: The central xy plane taken at $t = 64$ (Ω_i^{-1}), showing B_x, u_x, and mixing. The phase of the KH waves varies in the y direction generating significant structure in the field-aligned direction.

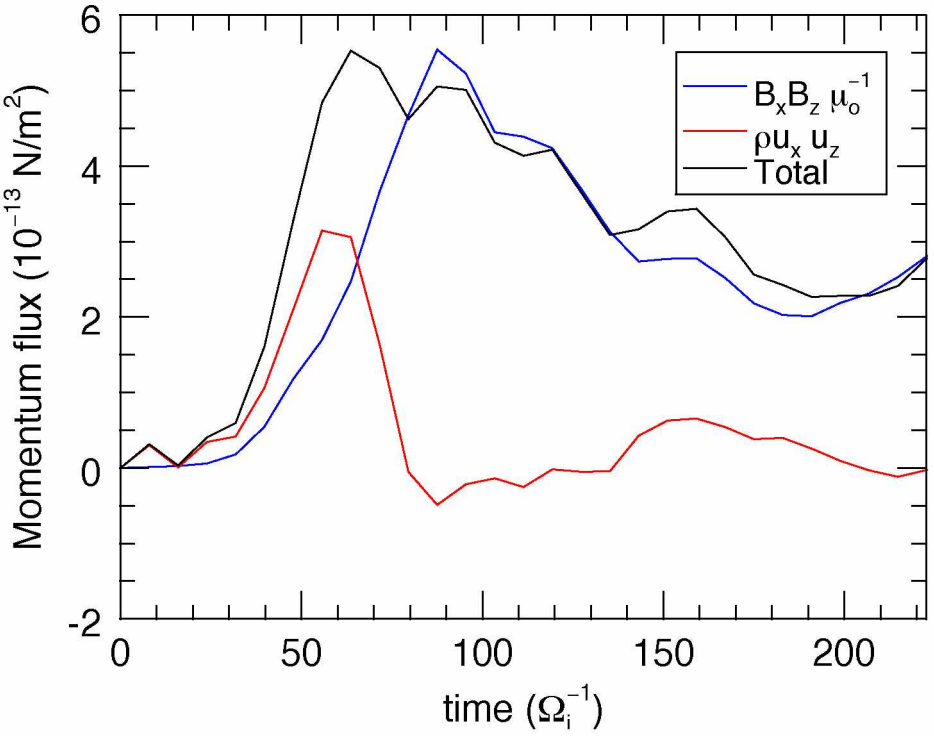

Figure C.4: Shear stresses as a function of time. Both Reynolds (T_{xz}^R) and Maxwell (T_{xz}^M) stresses contribute to the momentum transport, but T_{xz}^M provides the dominant contribution.

Strictly speaking, the KH instability is a dynamic process, but we treat the average state of the magnetopause boundary as static (i.e., between the limits of a diffuse boundary layer and actively growing vortices). The volume integral of the steady state momentum equation can be written as a surface integral via the divergence theorem,

$$\int \nabla \cdot \left[\rho \mathbf{uu} + \mathbf{P} + \frac{B^2}{2\mu_o}\mathbf{I} - \frac{\mathbf{BB}}{\mu_o}\right] dV = \oint \left[\rho \mathbf{uu} + \mathbf{P} + \frac{B^2}{2\mu_o}\mathbf{I} - \frac{\mathbf{BB}}{\mu_o}\right] \cdot d\mathbf{a} = 0. \qquad (21)$$

Here we integrate over the central xz plane shown in Figure C.3, comparing the off-diagonal elements of the $\rho\mathbf{uu}$ (Reynolds) and $\mathbf{BB}/\mu_o$ (Maxwell) terms. Specifically, we are interested in tangential x-directed momentum transported in the normal z direction, or $T_{xz}^R = \rho u_x u_z$ and $T_{xz}^M = B_x B_z/\mu_o$. Figure C.4 compares T_{xz}^M with T_{xz}^R as a function of time, showing the overall net positive contribution of the Maxwell stresses, though the Reynolds stresses also contribute. The momentum fluxes increase rapidly as the instability progresses through the inverse cascade, but at later times decrease as the simulation saturates in the $m = 1$ mode.

Estimate of dawnside sheath flow reduction

An estimate of the effect on Saturn's dawnside sheath flow can be made using the momentum transport rate from the hybrid simulations. Following Figure C.5, we let $+\hat{\mathbf{t}}$ (tangential) be

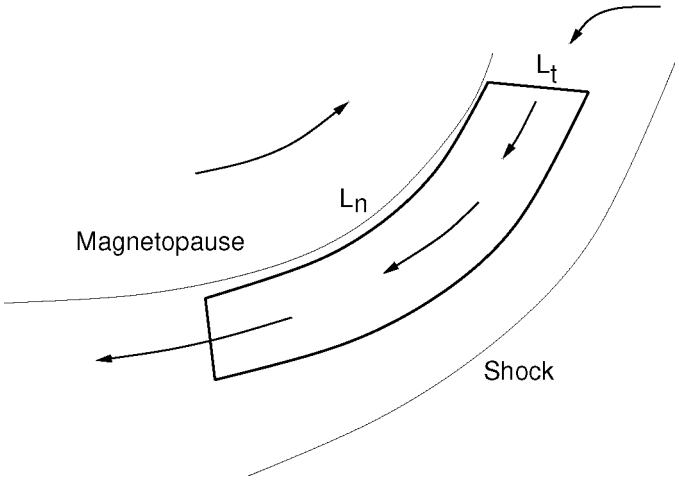

Figure C.5: An equatorial cross section of the volume considered for evaluating the momentum transport to Saturn's dawnside magnetosheath.

toward the subsolar point and $+\hat{\mathbf{n}}$ (normal) be toward the planet (simulation coordinates). Assume a volume of the sheath with equal inflow (1) and outflow (2) areas with width L_t and area $a_t = L_t \delta z$ where δz is the vertical scale of the KH unstable region of the magnetopause boundary. The area on the magnetopause boundary (3) is $a_n = L_n dz$, so the ratio of the areas is, e.g., L_n/L_t.

For the case of no viscous stress (on the magnetopause boundary surface a_n) the tangential component of the force balance equation (Eq. 21) is

$$\rho_1 u_1^2 a_t - \rho_2 u_2^2 a_t + P_1 a_t - P_2 a_t = 0. \tag{22}$$

If we assume that $\rho_1 u_1^2 \ll \rho_2 u_2^2$ (assume negligible dynamic pressure at inflow boundary, okay for subsolar point), then the pressure difference can be expressed in terms of the asymptotic sheath flow, u_2, or

$$\rho_2 u_2^2 = P_1 - P_2 \tag{23}$$

where P represents both thermal plasma pressure and magnetic pressure associated with MHD flow of shocked plasma in the sheath.

Now consider the case where viscous stresses (tangential drag) are present on the magnetopause boundary, but assume that P_1 and P_2 are unchanged due to modified flow. For the sake of a rough estimate (upper limit), we assume that Eq. 23 is valid and Eq. 21 becomes

$$P_1 a_t - P_2 a_t - \rho_2 (u_2')^2 a_t - \frac{B_n B_t}{\mu_o} a_n + \rho_3 u_n u_t a_n = 0 \tag{24}$$

which implies

$$(\Delta u_2)^2 = \frac{1}{\rho_2} \left(\frac{B_n B_t}{\mu_o} - \rho_3 u_n u_t \right) \frac{a_n}{a_t} \tag{25}$$

where $(\Delta u_2)^2 = u_2^2 - (u_2')^2$ and where ρ_3 is the mass density on the magnetopause boundary.

Typical upper limit values for the Maxwell and Reynolds stresses on the RHS from the hybrid simulations are 4×10^{-13} N/m^2, the average sheath mass density is $\rho_2 = 0.18$ cm^{-3}, and $a_n/a_t = L_n/L_t \sim 15/3 = 5$. For these parameters $\Delta u_2 \sim 80$ km/s. This is consistent with the observed flow reduction in Saturn's dawn side magnetosheath where the expected asymptotic flow is 200 km/s.

Conclusions

The viscous-like interaction between the solar wind and Saturn's magnetosphere is manifested by significant dawn-dusk asymmetries in magnetosheath flows (*Burkholder et al.*, 2017). Using a three-dimensional hybrid simulation we have quantified the momentum transport at Saturn's Kelvin-Helmholtz unstable magnetopause boundary. We conclude as follows:

- At the root of the viscous-like interaction are Maxwell shear stresses generated at the magnetopause boundary by magnetic field line threading.
- Small-scale and intermittent reconnection facilitate field line threading of the boundary at multiple reconnection sites.
- Magnetic field fluctuations are turbulent and plasma heating is expected.
- Diffusive plasma transport leads to a rapid mixing of magnetosphere and solar wind plasma.
- The episodic nature of the KH instability may account for the wide range of dawnside sheath flows reported by *Burkholder et al.* (2017).

Future studies will investigate the effect of heavy and/or superthermal ions as well as turbulent heating and associated diffusive transport. Momentum fluxes from our local simulations will also be compared with global simulations (e.g., *Zhang et al.* (2018)) to determine whether numerical effects (i.e., viscosity) are an accurate approximation to the realistic kinetic-scale physics that cannot be resolved in global simulations.

Bibliography

Adamson, E., J. Büchner, and A. Otto (2013), On the role of current dissipation in the energization of coronal bright points, *Astronomy and Astrophysics*, *557*, A118, doi: 10.1051/0004-6361/201321281.

Alfvén, H. (1942), Existence of Electromagnetic-Hydrodynamic Waves, *Nature*, *150*, 405–406, doi:10.1038/150405d0.

Alfvén, H. (1957), On the theory of comet tails, *Tellus*, *9*(1), 92–96, doi:10.1111/j.2153-3490.1957.tb01855.x.

Altschuler, M. D., and G. Newkirk (1969), Magnetic Fields and the Structure of the Solar Corona. I: Methods of Calculating Coronal Fields, *Solar Physics*, *9*, 131–149, doi: 10.1007/BF00145734.

Antiochos, S. K., C. R. DeVore, J. T. Karpen, and Z. Mikić (2007), Structure and dynamics of the sun's open magnetic field, *The Astrophysical Journal*, *671*(1), 936.

Archontis, V. (2008), Magnetic flux emergence in the sun, *Journal of Geophysical Research: Space Physics*, *113*(A3), doi:10.1029/2007JA012422.

Arnold, L., G. Li, X. Li, and Y. Yan (2013), Observation of flux-tube crossings in the solar wind, *The Astrophysical Journal*, *766*(1), 2.

Aulanier, G., Pariat, E., and Démoulin, P. (2005), Current sheet formation in quasi separatrix layers and hyperbolic flux tubes, *Astronomy and Astrophysics*, *444*(3), 961–976, doi:10.1051/0004-6361:20053600.

Axford, W. I. (1964), Viscous interaction between the solar wind and the earth's magnetosphere, *12*, 45.

Axford, W. I., and C. O. Hines (1961), A unifying theory of high latitude geophysical phenomena and geomagnetic storms, *Can. J. Phys.*, *39*, 1433–1464.

Bahng, J., and M. Schwarzschild (1961), Lifetime of Solar Granules., *The Astrophysical Journal*, *134*, 312, doi:10.1086/147160.

Bame, S. J., J. R. Asbridge, W. C. Feldman, and J. T. Gosling (1977), Evidence for a structure-free state at high solar wind speeds, *Journal of Geophysical Research*, *82*, 1487–1492, doi:10.1029/JA082i010p01487.

Bandyopadhyay, R., A. Chasapis, R. Chhiber, T. N. Parashar, B. A. Maruca ,..., and R. J. Strangeway (2018), Solar wind turbulence studies using MMS fast plasma investigation data, *The Astrophysical Journal*, *866*(2), 81, doi:10.3847/1538-4357/aade93.

Bartley, W. C., R. P. Bukata, K. G. McCracken, and U. R. Rao (1966), Anisotropic cosmic radiation fluxes of solar origin, *Journal of Geophysical Research*, *71*(13), 3297–3304, doi:10.1029/JZ071i013p03297.

Biernat, H. K., M. F. Heyn, R. P. Rijnbeek, V. S. Semenov, and C. J. Farrugia (1989), The structure of reconnection layers: Application to the earth's magnetopause, *Journal of Geophysical Research: Space Physics*, *94*(A1), 287–298, doi:10.1029/JA094iA01p00287.

Birdsall, C. K., and A. B. Langdon (1991), *Plasma Physics via Computer Simulation*, CRC Press.

Birn, J., J. F. Drake, M. A. Shay, B. N. Rogers, R. E. Denton, M. Hesse, M. Kuznetsova, Z. W. Ma, A. Bhattacharjee, A. Otto, and P. L. Pritchett (2001), Geospace environmental modeling (gem) magnetic reconnection challenge, *Journal of Geophysical Research: Space Physics*, *106*(A3), 3715–3719, doi:10.1029/1999JA900449.

Birn, J., M. Hesse, and K. Schindler (2006), Entropy conservation in simulations of magnetic reconnection, *Physics of Plasmas*, *13*(9), 092117, doi:10.1063/1.2349440.

Birn, J., M. Hesse, K. Schindler, and S. Zaharia (2009), Role of entropy in magnetotail dynamics, *Journal of Geophysical Research (Space Physics)*, *114*, A00D03, doi:10.1029/2008JA014015.

Boris, J. (1970), The acceleration calculation from a scalar potential, MATT-152, Plasma Physics Laboratory, Princeton University.

Borovsky, J. E. (2006), Eddy viscosity and flow properties of the solar wind: Co-rotating interaction regions, coronal-mass-ejection sheaths, and solar-wind/magnetosphere coupling, *Physics of Plasmas*, *13*(5), doi:10.1063/1.2200308.

Borovsky, J. E. (2008), Flux tube texture of the solar wind: Strands of the magnetic carpet at 1 au?, *Journal of Geophysical Research: Space Physics*, *113*(A8), doi: 10.1029/2007JA012684, a08110.

Borovsky, J. E. (2010), On the variations of the solar wind magnetic field about the parker spiral direction, *Journal of Geophysical Research: Space Physics*, *115*(A9), doi: 10.1029/2009JA015040.

Bradley, E., and H. Kantz (2015), Nonlinear time-series analysis revisited, *Chaos: An Interdisciplinary Journal of Nonlinear Science*, *25*(9), 097,610, doi:10.1063/1.4917289.

Bruno, R., V. Carbone, P. Veltri, E. Pietropaolo, and B. Bavassano (2001), Identifying intermittency events in the solar wind, *Planetary and Space Science*, *49*(12), 1201 – 1210, doi:https://doi.org/10.1016/S0032-0633(01)00061-7, nonlinear Dynamics and Fractals in Space.

Buffington, A., M. M. Bisi, J. M. Clover, P. P. Hick, B. V. Jackson, and T. A. Kuchar (2008), Analysis of plasma-tail motions for comets c/2001 q4 (NEAT) and c/2002 t7 (LINEAR) using observations from SMEI, *The Astrophysical Journal*, *677*(1), 798–807, doi:10.1086/529039.

Burkholder, B., P. A. Delamere, X. Ma, M. F. Thomsen, R. J. Wilson, and F. Bagenal (2017), Local time asymmetry of Saturn's magnetosheath flows, *Geophys. Res. Lett.*, *44*, 5877–5883, doi:10.1002/2017GL073031.

Burkholder, B. L., and A. Otto (Submitted - 2019), Magnetic reconnection of solar flux tubes and coronal reconnection signatures in the solar wind at 1 au, *Journal of Geophysical Research: Space Physics*.

Burkholder, B. L., A. Otto, P. A. Delamere, and J. E. Borovsky (2018), Magnetic connectivity in the corona as a source of structure in the solar wind, *Journal of Geophysical Research: Space Physics*, *0*.

Burkholder, B. L., P. A. Delamere, J. R. Johnson, and C. S. Ng (Submitted - 2019), Identifying active kelvin-helmholtz vortices on saturn's magnetopause boundary, *Journal of Geophysical Research: Space Physics*.

Candelaresi, S., D. I. Pontin, and G. Hornig (2016), Effects of field-line topology on energy propagation in the corona, *The Astrophysical Journal*, *832*(2), 150.

Cassak, P. A., and M. A. Shay (2007), Scaling of asymmetric magnetic reconnection: General theory and collisional simulations, *Physics of Plasmas*, *14*(10), 102114, doi: 10.1063/1.2795630.

Caudal, G. (1986), A self-consistent model of Jupiter's magnetodisc including the effects of centrifugal force and pressure, *Journal of Geophysical Research*, *91*, 4201–4221, doi: 10.1029/JA091iA04p04201.

Chandrasekhar, S. (1961), *Hydrodynamic and hydromagnetic stability*.

Chaston, C. C., J. R. Johnson, M. Wilber, M. Acuna, M. L. Goldstein, and H. Reme (2009), Kinetic alfvén wave turbulence and transport through a reconnection diffusion region, *Phys. Rev. Lett.*, *102*, 015,001, doi:10.1103/PhysRevLett.102.015001.

Close, R. M., C. E. Parnell, and E. R. Priest (2004), Separators in 3d quiet-sun magnetic fields, *Solar Physics*, *225*(1), 21–46.

Close, R. M., C. E. Parnell, D. W. Longcope, and E. R. Priest (2005), Coronal flux recycling times, *Solar Physics*, *231*(1), 45–70, doi:10.1007/s11207-005-6878-1.

Cowee, M. M., D. Winske, and S. P. Gary (2009), Two-dimensional hybrid simulations of superdiffusion at the magnetopause driven by Kelvin-Helmholtz instability, *Journal of Geophysical Research (Space Physics)*, *114*, 10,209–+, doi:10.1029/2009JA014222.

Cowee, M. M., D. Winske, and S. P. Gary (2010), Hybrid simulations of plasma transport by Kelvin-Helmholtz instability at the magnetopause: Density variations and magnetic shear, *Journal of Geophysical Research (Space Physics)*, *115*, 6214–+, doi:10.1029/2009JA015011.

Crooker, N. U., J. T. Gosling, and S. W. Kahler (2002), Reducing heliospheric magnetic flux from coronal mass ejections without disconnection, *Journal of Geophysical Research: Space Physics*, *107*(A2), SSH 3–1–SSH 3–5, doi:10.1029/2001JA000236.

David, C., A. H. Gabriel, and F. Bely-Dubau (1997), Temperature Structure in Coronal Holes, in *Fifth SOHO Workshop: The Corona and Solar Wind Near Minimum Activity*, *ESA Special Publication*, vol. 404, edited by A. Wilson, p. 319.

De Moortel, I., and Galsgaard, K. (2006), Numerical modelling of 3d reconnection due to rotational footpoint motions, *Astronomy and Astrophysics*, *451*(3), 1101–1115, doi: 10.1051/0004-6361:20054587.

DeForest, C. E., R. A. Howard, M. Velli, N. Viall, and A. Vourlidas (2018), The Highly Structured Outer Solar Corona, *The Astrophysical Journal*, *862*, 18, doi:10.3847/1538-4357/aac8e3.

Delamere, P. A. (2009), Hybrid code simulations of the solar wind interaction with Pluto, *Journal of Geophysical Research (Space Physics)*, *114*, 3220–+, doi:10.1029/2008JA013756.

Delamere, P. A. (2015), *Magnetotails in the Solar System*, chap. Solar wind interaction with the giant magnetospheres and Earth's magnetosphere, John Wiley and Sons, Inc.

Delamere, P. A., and F. Bagenal (2010), Solar wind interaction with Jupiter's magnetosphere, *Journal of Geophysical Research (Space Physics)*, *115*, 10,201–+, doi:10.1029/2010JA015347.

Delamere, P. A., and F. Bagenal (2013), Magnetotail structure of the giant magnetospheres: Implications of the viscous interaction with the solar wind, *Journal of Geophysical Research (Space Physics)*, *118*, 7045–7053, doi:10.1002/2013JA019179.

Delamere, P. A., D. W. Swift, and H. C. Stenbaek-Nielsen (1999), A three-dimensional hybrid code simulation of the December 1984 solar wind AMPTE release, *Geophys. Res. Lett.*, *26*, 2837–2840, doi:10.1029/1999GL900602.

Delamere, P. A., R. J. Wilson, and A. Masters (2011), Kelvin-Helmholtz instability at Saturn's magnetopause: Hybrid simulations, *Journal of Geophysical Research (Space Physics)*, *116*, A10222, doi:10.1029/2011JA016724.

Delamere, P. A., R. J. Wilson, S. Eriksson, and F. Bagenal (2013), Magnetic signatures of Kelvin-Helmholtz vortices on Saturn's magnetopause: Global survey, *Journal of Geophysical Research (Space Physics)*, *118*, 393–404, doi:10.1029/2012JA018197.

Delamere, P. A., A. Otto, X. Ma, F. Bagenal, and R. J. Wilson (2015a), Magnetic flux circulation in the rotationally driven giant magnetospheres, *Journal of Geophysical Research (Space Physics)*, *120*, 4229–4245, doi:10.1002/2015JA021036.

Delamere, P. A., F. Bagenal, C. Paranicas, A. Masters, A. Radioti, B. Bonfond, L. Ray, X. Jia, J. Nichols, and C. Arridge (2015b), Solar Wind and Internally Driven Dynamics: Influences on Magnetodiscs and Auroral Responses, *Space Sci. Rev.*, *187*, 51–97, doi:10.1007/s11214-014-0075-1.

Delamere, P. A., B. Burkholder, and X. Ma (2018), Three-dimensional hybrid simulation of viscous-like processes at saturn's magnetopause boundary, *Geophysical Research Letters*, *45*(16), 7901–7908, doi:10.1029/2018GL078922.

Démoulin, P., J. C. Henoux, E. R. Priest, and C. H. Mandrini (1996a), Quasi-Separatrix layers in solar flares. I. Method., *Astronomy and Astrophysics*, *308*, 643–655.

Démoulin, P., E. R. Priest, and D. P. Lonie (1996b), Three-dimensional magnetic reconnection without null points: 2. application to twisted flux tubes, *Journal of Geophysical Research: Space Physics*, *101*(A4), 7631–7646, doi:10.1029/95JA03558.

DeRosa, M. L., and G. Barnes (2018), Does Nearby Open Flux Affect the Eruptivity of Solar Active Regions?, *The Astrophysical Journal*, *861*, 131, doi:10.3847/1538-4357/aac77a.

Desroche, M., F. Bagenal, P. A. Delamere, and N. Erkaev (2013), Conditions at the magnetopause of Saturn and implications for the solar wind interaction, *Journal of Geophysical Research (Space Physics)*, *118*, 3087–3095, doi:10.1002/jgra.50294.

Dougherty, M. K., S. Kellock, D. J. Southwood, A. Balogh, E. J. Smith, B. T. Tsurutani, B. Gerlach, K.-H. Glassmeier, F. Gleim, C. T. Russell, G. Erdos, F. M. Neubauer, and S. W. H. Cowley (2004), The Cassini Magnetic Field Investigation, *Space Science Reviews*, *114*, 331–383, doi:10.1007/s11214-004-1432-2.

Dungey, J. W. (1961), Interplanetary magnetic field and the auroral zones, *Phys. Rev. Lett.*, *6*(2), 47–48, doi:10.1103/PhysRevLett.6.47.

Edmondson, J. K., B. J. Lynch, S. K. Antiochos, D. C. R., and T. H. Zurbuchen (2009), Reconnection-driven dynamics of coronal-hole boundaries, *The Astrophysical Journal*, *707*(2), 1427.

Edmondson, J. K., S. K. Antiochos, C. R. DeVore, and T. H. Zurbuchen (2010), Formation and reconnection of three-dimensional current sheets in the solar corona, *The Astrophysical Journal*, *718*(1), 72.

Effenberger, F., K. Thust, L. Arnold, R. Grauer, and J. Dreher (2011), Numerical simulation of current sheet formation in a quasi separatrix layer using adaptive mesh refinement, *Physics of Plasmas*, *18*(3), 032,902, doi:10.1063/1.3565018.

Fairfield, D. H., A. Otto, T. Mukai, S. Kokubun, R. P. Lepping, J. T. Steinberg, A. J. Lazarus, and T. Yamamoto (2000), Geotail observations of the Kelvin-Helmholtz instability

at the equatorial magnetotail boundary for parallel northward fields, *J. Geophys. Res.*, *105*, 21,159–21,174, doi:10.1029/1999JA000316.

Fisk, L. A., and T. H. Zurbuchen (2006), Distribution and properties of open magnetic flux outside of coronal holes, *Journal of Geophysical Research: Space Physics*, *111*(A9), doi:10.1029/2005JA011575, a09115.

Fisk, L. A., T. H. Zurbuchen, and N. A. Schwadron (1999), On the Coronal Magnetic Field: Consequences of Large-Scale Motions, *The Astrophysical Journal*, *521*, 868–877, doi:10.1086/307556.

Fleshman, B. L., P. A. Delamere, F. Bagenal, and T. Cassidy (2013), A 1-D model of physical chemistry in Saturn's inner magnetosphere, *Journal of Geophysical Research (Planets)*, *118*, 1567–1581, doi:10.1002/jgre.20106.

Fuselier, S. A., R. Frahm, W. S. Lewis, A. Masters, J. Mukherjee, S. M. Petrinec, and I. J. Sillanpaa (2014), The location of magnetic reconnection at saturn's magnetopause: A comparison with earth, *Journal of Geophysical Research: Space Physics*, *119*(4), 2563–2578, doi:10.1002/2013JA019684, 2013JA019684.

Gabriel, A. H. (1976), A magnetic model of the solar transition region, *Philosophical Transactions of the Royal Society of London Series A*, *281*, 339–352, doi:10.1098/rsta.1976.0031.

Galsgaard, K., R. V. Reddy, and G. J. Rickard (1997), Energy release sites in magnetic fields containing single or multiple nulls, *Solar Physics*, *176*(2), 299–325, doi:10.1023/A:1004932005518.

Galtier, S., A. Pouquet, and A. Mangeney (2005), On spectral scaling laws for incompressible anisotropic magnetohydrodynamic turbulence on spectral scaling laws for incompressible anisotropic magnetohydrodynamic turbulence, *Physics of Plasmas*, *12*(092310).

Geiss, J., G. Gloeckler, and R. von Steiger (1995), Origin of the Solar Wind From Composition Data, *Space Science Reviews*, *72*, 49–60, doi:10.1007/BF00768753.

Goertz, C. K. (1983), Detached plasma in saturn's front side magnetosphere, *Geophysical Research Letters*, *10*(6), 455–458, doi:10.1029/GL010i006p00455.

Gosling, J. T., H. Tian, and T. D. Phan (2011), Pulsed Alfvén Waves in the Solar Wind, *The Astrophysical Journal Letters*, *737*, L35, doi:10.1088/2041-8205/737/2/L35.

Harned, D. S. (1982), Quasineutral hybrid simulation of macroscopic plasma phenomena, *J. Comput. Phys*, *47*, 452.

Hasegawa, H., M. Fujimoto, T. Phan, H. Reme, A. Balogh, M. Dunlop, C. Hashimoto, and R. TanDokoro (2004), Transport of solar wind into earth's magnetosphere through rolled-up kelvin-helmholtz vortices, *NATURE*, *430*, 755–758, doi:10.1038/nature02799.

He, J.-S., C.-Y. Tu, H. Tian, and E. Marsch (2010), Solar wind origins in coronal holes and in the quiet Sun, *Advances in Space Research*, *45*, 303–309, doi:10.1016/j.asr.2009.07.020.

Hesse, M., and K. Schindler (1988), A theoretical foundation of general magnetic reconnection, *Journal of Geophysical Research: Space Physics*, *93*(A6), 5559–5567, doi:10.1029/JA093iA06p05559.

Higginson, A. K., and B. J. Lynch (2018), Structured slow solar wind variability: Streamer-blob flux ropes and torsional alfvn waves, *The Astrophysical Journal*, *859*(1), 6.

Higginson, A. K., S. K. Antiochos, C. R. DeVore, P. F. Wyper, and T. H. Zurbuchen (2017a), Dynamics of coronal hole boundaries, *The Astrophysical Journal*, *837*(2), 113.

Higginson, A. K., S. K. Antiochos, C. R. DeVore, P. F. Wyper, and T. H. Zurbuchen (2017b), Formation of heliospheric arcs of slow solar wind, *The Astrophysical Journal Letters*, *840*(1), L10.

Hsieh, M.-S., and A. Otto (2014), The influence of magnetic flux depletion on the magnetotail and auroral morphology during the substorm growth phase, *Journal of Geophysical Research: Space Physics*, *119*(5), 3430–3443, doi:10.1002/2013JA019459.

Iwai, K., K. Shibasaki, S. Nozawa, T. Takahashi, S. Sawada, J. Kitagawa, S. Miyawaki, and H. Kashiwagi (2014), Coronal magnetic field and the plasma beta determined from radio and multiple satellite observations, *Earth, Planets and Space*, *66*(1), 149, doi:10.1186/s40623-014-0149-z.

Jackman, C. M., and C. S. Arridge (2011), Solar Cycle Effects on the Dynamics of Jupiter's and Saturn's Magnetospheres, *Solar Phys.*, *274*, 481–502, doi:10.1007/s11207-011-9748-z.

Janvier, M., G. Aulanier, V. Bommier, B. Schmieder, P. Démoulin, and E. Pariat (2014), Electric Currents in Flare Ribbons: Observations and Three-dimensional Standard Model, *The Astrophysical Journal*, *788*, 60, doi:10.1088/0004-637X/788/1/60.

Johnson, J. R., and C. Z. Cheng (1997), Kinetic Alfvén waves and plasma transport at the magnetopause, *Geophys. Res. Let*, *24*, 1423–1426, doi:10.1029/97GL01333.

Kaminker, V., P. A. Delamere, C. S. Ng, T. Dennis, A. Otto, and X. Ma (2017), Local time dependence of turbulent magnetic fields in saturn's magnetodisc, *Journal of Geophysical Research: Space Physics*, *122*(4), 3972–3984, doi:10.1002/2016JA023834.

Kavosi, S., and J. Raeder (2015), Ubiquity of kelvin helmholtz waves at earth's magnetopause, *Nature Communications*, doi:10.1038/ncomms8019.

Keiling, A., C. M. Jackman, and P. A. Delamere (Eds.) (2015), *Magnetotails in the Solar System*, *Washington DC American Geophysical Union Geophysical Monograph Series*, vol. 207, doi:10.1002/9781118842324.

Kivelson, M. G., and X. Jia (2014), Control of periodic variations in saturn's magnetosphere by compressional waves, *Journal of Geophysical Research: Space Physics*, *119*(10), 8030–8045, doi:10.1002/2014JA020258, 2014JA020258.

Knetter, T., F. M. Neubauer, T. Horbury, and A. Balogh (2003), Discontinuity observations with cluster, *Advances in Space Research*, *32*(4), 543–548, doi:10.1016/S0273-1177(03)00335-1.

Knetter, T., F. M. Neubauer, T. Horbury, and A. Balogh (2004), Four-point discontinuity observations using cluster magnetic field data: A statistical survey, *Journal of Geophysical Research: Space Physics*, *109*(A6), doi:10.1029/2003JA010099.

La Belle-Hamer, A. L., A. Otto, and L. C. Lee (1994), Magnetic reconnection in the presence of sheared plasma flow: Intermediate shock formation, *Physics of Plasmas*, *1*(3), 706–713, doi:10.1063/1.870816.

Lai, H. R., H. Y. W. C. T. Russell, C. S. Arridge, and M. K. M. K. Dougherty (2012), Reconnection at the magnetopause of saturn: Perspective from fte occurrence and magnetosphere size, *J. Geophys. Res.*, *117*(A5), A05,222.

Leamon, R. J., C. W. Smith, N. F. Ness, and H. K. Wong (1999), Dissipation range dynamics: Kinetic Alfvén waves and the importance of β_e, *Journal of Geophysical Research*, *104*, 22,331–22,344, doi:10.1029/1999JA900158.

Levy, R. H., H. E. Petschek, and G. L. Siscoe (1964), Aerodynamic aspects of the magnetospheric flow, *AIAA Journal*, *2*, 2065–2076, doi:10.2514/3.2745.

Lin, Y., and L. C. Lee (1993), Structure of the dayside reconnection layer in resistive mhd and hybrid models, *Journal of Geophysical Research: Space Physics*, *98*(A3), 3919–3934, doi:10.1029/92JA02363.

Lin, Y., and L. C. Lee (1995), Simulation study of the riemann problem associated with the magnetotail reconnection, *Journal of Geophysical Research: Space Physics*, *100*(A10), 19,227–19,237, doi:10.1029/95JA01549.

Lin, Y., L. C. Lee, and C. F. Kennel (1992), The role of intermediate shocks in magnetic reconnection, *Geophysical Research Letters*, *19*(3), 229–232, doi:10.1029/91GL03008.

Linker, J. A., R. Lionello, Z. Mikić, V. S. Titov, and S. K. Antiochos (2011), The evolution of open magnetic flux driven by photospheric dynamics, *The Astrophysical Journal*, *731*(2), 110.

Lockwood, M., and M. Hapgood (1998), On the cause of a magnetospheric flux transfer event, *Journal of Geophysical Research*, *103*, 26,453–26,478, doi:10.1029/98JA02244.

Longcope, D. W. (2005), Topological methods for the analysis of solar magnetic fields, *Living Reviews in Solar Physics*, *2*(1), 7, doi:10.12942/lrsp-2005-7.

Longcope, D. W., and C. E. Parnell (2009), The Number of Magnetic Null Points in the Quiet Sun Corona, *Solar Physics*, *254*, 51–75, doi:10.1007/s11207-008-9281-x.

Ma, X. (2012), Kelvin-helmholtz instability and magnetic reconnection at the earth's magnetospheric boundary, Ph.D. thesis, University of Alaska Fairbanks, Fairbanks, Alaska.

Ma, X., and A. Otto (2013), Mechanisms of field-aligned current formation in magnetic reconnection, *Journal of Geophysical Research (Space Physics)*, *118*, 4906–4914, doi:10.1002/jgra.50457.

Ma, X., and A. Otto (2014), Nonadiabatic heating in magnetic reconnection, *Journal of Geophysical Research: Space Physics*, *119*(7), 5575–5588, doi:10.1002/2014JA019856.

Ma, X., A. Otto, and P. A. Delamere (2014a), Interaction of magnetic reconnection and Kelvin-Helmholtz modes for large magnetic shear: 1. Kelvin-Helmholtz trigger, *Journal of Geophysical Research (Space Physics)*, *119*, 781–797, doi:10.1002/2013JA019224.

Ma, X., A. Otto, and P. A. Delamere (2014b), Interaction of magnetic reconnection and Kelvin-Helmholtz modes for large magnetic shear: 2. Reconnection trigger, *Journal of Geophysical Research (Space Physics)*, *119*, 808–820, doi:10.1002/2013JA019225.

Ma, X., B. Stauffer, P. A. Delamere, and A. Otto (2015), Asymmetric kelvin-helmholtz propagation at saturn's dayside magnetopause, *Journal of Geophysical Research: Space Physics*, *120*(3), 1867–1875, doi:10.1002/2014JA020746.

Ma, X., A. Otto, and P. A. Delamere (2016), Magnetic reconnection with a fast perpendicular sheared flow, *Journal of Geophysical Research: Space Physics*, *121*(10), 9427–9442, doi:10.1002/2016JA023107.

Ma, X., P. Delamere, A. Otto, and B. Burkholder (2017), Plasma transport driven by the three-dimensional kelvin-helmholtz instability, *Journal of Geophysical Research: Space Physics*, *122*(10), 10,382–10,395, doi:10.1002/2017JA024394.

Ma, X., P. A. Delamere, K. Nykyri, B. L. Burkholder, B. R. Neupane, and R. C. Rice (Submitted - 2019), Comparison between fluid simulation with test particles and hybrid simulation for the kelvin-helmholtz instabililty, *Journal of Geophysical Research: Space Physics*.

Mariani, F., B. Bavassano, U. Villante, and N. F. Ness (1973), Variations of the occurrence rate of discontinuities in the interplanetary magnetic field, *Journal of Geophysical Research*, *78*(34), 8011–8022, doi:10.1029/JA078i034p08011.

Masson, S., E. Pariat, G. Aulanier, and C. J. Schrijver (2009), The Nature of Flare Ribbons in Coronal Null-Point Topology, *The Astrophysical Journal*, *700*, 559–578, doi:10.1088/0004-637X/700/1/559.

Masson, S., G. Aulanier, E. Pariat, and K.-L. Klein (2012), Interchange slip-running reconnection and sweeping sep beams, *Solar Physics*, *276*(1), 199–217.

Masson, S., É. Pariat, G. Valori, N. Deng, C. Liu, H. Wang, and H. Reid (2017), Flux rope, hyperbolic flux tube, and late extreme ultraviolet phases in a non-eruptive circular-ribbon flare, *Astronomy and Astrophysics*, *604*, A76, doi:10.1051/0004-6361/201629654.

Masters, A. (2018), A more viscous-like solar wind interaction with all the giant planets, *Geophysical Research Letters*, *45*(15), 7320–7329, doi:10.1029/2018GL078416.

Masters, A., N. Achilleos, C. Bertucci, M. K. Dougherty, S. J. Kanani, C. S. Arridge, H. J. McAndrews, and A. J. Coates (2009), Surface waves on Saturn's dawn flank magnetopause driven by the Kelvin-Helmholtz instability, *Planetery and Space Science*, *57*, 1769–1778, doi:10.1016/j.pss.2009.02.010.

Masters, A., N. Achilleos, M. G. Kivelson, N. Sergis, M. K. Dougherty, M. F. Thomsen, C. S. Arridge, S. M. Krimigis, H. J. McAndrews, S. J. Kanani, N. Krupp, and A. J. Coates (2010), Cassini observations of a Kelvin-Helmholtz vortex in Saturn's outer magnetosphere, *Journal of Geophysical Research (Space Physics)*, *115*, A07225, doi:10.1029/2010JA015351.

Masters, A., D. G. Mitchell, A. J. Coates, and M. K. Dougherty (2011), Saturn's low-latitude boundary layer: 1. Properties and variability, *JGR*, doi:10.1029/2010JA016421.

Masters, A., N. Achilleos, J. C. Cutler, A. J. Coates, M. K. Dougherty, and G. H. Jones (2012), Surface waves on Saturn's magnetopause, *Planet. Space Sci.*, *65*, 109–121, doi: 10.1016/j.pss.2012.02.007.

Masters, A., M. Fujimoto, H. Hasegawa, C. T. Russell, A. J. Coates, and M. K. Dougherty (2014), Can magnetopause reconnection drive Saturn's magnetosphere?, *Geophys. Res. Let*, *41*, 1862–1868, doi:10.1002/2014GL059288.

Matsumoto, Y., and M. Hoshino (2004), Onset of turbulence induced by a Kelvin-Helmholtz vortex, *Geophys. Res. Let*, *31*, 2807–+, doi:10.1029/2003GL018195.

McAndrews, H. J., C. J. Owen, M. F. Thomsen, B. Lavraud, A. J. Coates, M. K. Dougherty, and D. T. Young (2008), Evidence for reconnection at saturn's magnetopause, *Journal of Geophysical Research: Space Physics*, *113*(A4), doi:10.1029/2007JA012581, a04210.

McComas, D. J., F. Bagenal, and R. W. Ebert (2014), Bimodal size of jupiter's magnetosphere, *Journal of Geophysical Research: Space Physics*, *119*(3), 1523–1529, doi: 10.1002/2013JA019660.

McCracken, K. G., and N. F. Ness (1966), The collimation of cosmic rays by the interplanetary magnetic field, *Journal of Geophysical Research*, *71*(13), 3315–3318, doi: 10.1029/JZ071i013p03315.

McLaughlin, J. A., A. W. Hood, and I. de Moortel (2011), Review Article: MHD Wave Propagation Near Coronal Null Points of Magnetic Fields, *Space Science Reviews*, *158*, 205–236, doi:10.1007/s11214-010-9654-y.

Miura, A. (1984), Anomalous transport by magnetohydrodynamic Kelvin-Helmholtz instabilities in the solar wind-magnetosphere interaction, *J. Geophys. Res.*, *89*, 801–818, doi: 10.1029/JA089iA02p00801.

Miura, A., and P. L. Pritchett (1982), Nonlocal stability analysis of the mhd kelvin-helmholtz instability in a compressible plasma, *Journal of Geophysical Research: Space Physics*, *87*(A9), 7431–7444, doi:10.1029/JA087iA09p07431.

Mozer, F. S., and A. Retinò (2007), Quantitative estimates of magnetic field reconnection properties from electric and magnetic field measurements, *Journal of Geophysical Research: Space Physics*, *112*(A10), doi:10.1029/2007JA012406.

Mullan, D. J., and C. W. Smith (2006), Solar wind statistics at 1 au: Alfven speed and plasma beta, *Solar Physics*, *234*(2), 325–338, doi:10.1007/s11207-006-2077-y.

Murphy, N. A., C. E. Parnell, and A. L. Haynes (2015), The appearance, motion, and disappearance of three-dimensional magnetic null points, *Physics of Plasmas*, *22*(10), 102,117, doi:10.1063/1.4934929.

Neugebauer, M. (2006), Comment on the abundances of rotational and tangential discontinuities in the solar wind, *Journal of Geophysical Research: Space Physics*, *111*(A4), doi:10.1029/2005JA011497.

Neugebauer, M., and J. Giacalone (2010), Progress in the study of interplanetary discontinuities, *AIP Conference Proceedings*, *1216*(1), 194–197, doi:10.1063/1.3395834.

Neupane, B. R., P. A. Delamere, R. J. Wilson, and X. Ma (2019), Quantifying mass and magnetic flux transport in saturn's magnetosphere, *Journal of Geophysical Research: Space Physics*, *124*(3), 1916–1926, doi:10.1029/2018JA026022.

Ng, C. S., P. A. Delamere, V. Kaminker, and P. A. Damiano (2018), Radial transport and plasma heating in jupiter's magnetodisc, *Journal of Geophysical Research: Space Physics*, *123*(8), 6611–6620, doi:10.1029/2018JA025345.

Otto, A., and K. Nykyri (2003), Kelvin-Helmholtz instability and magnetic reconnection: Mass transport at the LLBL, *Washington DC American Geophysical Union Geophysical Monograph Series*, *133*, 53–62, doi:10.1029/133GM05.

Otto, A., J. Büchner, and B. Nikutowski (2007), Force-free magnetic field extrapolation for MHD boundary conditions in simulations of the solar atmosphere, *Astronomy and Astrophysics*, *468*, 313–321, doi:10.1051/0004-6361:20054495.

Owens, M. J., R. T. Wicks, and T. S. Horbury (2011), Magnetic discontinuities in the near-earth solar wind: Evidence of in-transit turbulence or remnants of coronal structure?, *Solar Physics*, *269*(2), 411–420, doi:10.1007/s11207-010-9695-0.

Parker, E. N. (1958), Dynamics of the Interplanetary Gas and Magnetic Fields., *The Astrophysical Journal*, *128*, 664, doi:10.1086/146579.

Parker, E. N. (1963), Generalization and Extension of the Basic Solar Wind Model, in *Interplanetary dynamical processes*, pp. 244–248, Interscience Publishers, New York.

Parker, E. N. (1972), Topological Dissipation and the Small-Scale Fields in Turbulent Gases, *The Astrophysical Journal*, *174*, 499, doi:10.1086/151512.

Parnell, C. E., J. M. Smith, T. Neukirch, and E. R. Priest (1996), The structure of three dimensional magnetic neutral points, *Physics of Plasmas*, *3*(3), 759–770, doi: 10.1063/1.871810.

Parnell, C. E., A. L. Haynes, and K. Galsgaard (2010), Structure of magnetic separators and separator reconnection, *Journal of Geophysical Research: Space Physics*, *115*(A2).

Paschmann, G., and P. W. Daly (1998), *Analysis Methods for Multi-Spacecraft Data*, 185 pp.

Paschmann, G., and S. J. Schwartz (2000), ISSI Book on Analysis Methods for Multi-Spacecraft Data, in *Cluster-II Workshop Multiscale / Multipoint Plasma Measurements*, *ESA Special Publication*, vol. 449, edited by R. A. Harris, p. 99.

Paschmann, G., I. Papamastorakis, N. Sckopke, G. Haerendel, B. Sonnerup, S. J. Bame, J. R. Asbridge, J. Gosling, C. T. Russel, and R. C. Elphic (1979), Plasma acceleration at the earth's magnetopause: Evidence for reconnection, *Nature*, *282*, doi:10.1038/282243a0.

Petschek, H. E. (1964), Magnetic Field Annihilation, *NASA Special Publication*, *50*, 425.

Pilkington, N. M., N. Achilleos, C. S. Arridge, P. Guio, A. Masters, L. C. Ray, N. Sergis, M. F. Thomsen, A. J. Coates, and M. K. Dougherty (2015), Asymmetries observed in Saturn's magnetopause geometry, *Geophys. Res. Let*, *42*, 6890–6898, doi:10.1002/2015GL065477.

Platten, S. J., C. E. Parnell, A. L. Haynes, E. R. Priest, and D. H. Mackay (2014), The solar cycle variation of topological structures in the global solar corona, *Astronomy and Astrophysics*, *565*, A44, doi:10.1051/0004-6361/201323048.

Pollock, C., T. Moore, A. Jacques, J. Burch, U. Gliese ,. . . , and M. Zeuch (2016), Fast plasma investigation for magnetospheric multiscale, *Space Science Reviews*, *199*(1), 331–406, doi: 10.1007/s11214-016-0245-4.

Pontin, D. I., and P. F. Wyper (2015), The effect of reconnection on the structure of the sun's open-closed flux boundary, *The Astrophysical Journal*, *805*(1), 39.

Pontin, D. I., G. Hornig, and E. R. Priest (2004), Kinematic reconnection at a magnetic null point: spine-aligned current, *Geophysical & Astrophysical Fluid Dynamics*, *98*(5), 407–428, doi:10.1080/0309192042000272324.

Pontin, D. I., G. Hornig, and E. R. Priest (2005), Kinematic reconnection at a magnetic null point: fan-aligned current, *Geophysical & Astrophysical Fluid Dynamics*, *99*(1), 77–93, doi:10.1080/03091920512331328071.

Pontin, D. I., A. Bhattacharjee, and K. Galsgaard (2007), Current sheet formation and nonideal behavior at three-dimensional magnetic null points, *Physics of Plasmas*, *14*(5), 052,106, doi:10.1063/1.2722300.

Pontin, D. I., E. R. Priest, and K. Galsgaard (2013), On the nature of reconnection at a solar coronal null point above a separatrix dome, *The Astrophysical Journal*, *774*(2), 154.

Priest, E. R. (1984), *Solar Magnetohydrodynamics*, Geophysics and Astrophysics Monographs, Springer Netherlands.

Priest, E. R., and P. Démoulin (1995), Three dimensional magnetic reconnection without null points: 1. basic theory of magnetic flipping, *Journal of Geophysical Research: Space Physics*, *100*(A12), 23,443–23,463, doi:10.1029/95JA02740.

Priest, E. R., and D. I. Pontin (2009), Three-dimensional null point reconnection regimes, *Physics of Plasmas*, *16*(12), 122,101, doi:10.1063/1.3257901.

Priest, E. R., D. P. Lonie, and V. S. Titov (1996), Bifurcations of magnetic topology by the creation or annihilation of null points, *Journal of Plasma Physics*, *56*, 507–530, doi:10.1017/S0022377800019449.

Priest, E. R., T. N. Bungey, and V. S. Titov (1997), The 3D topology and interaction of complex magnetic flux systems, *Geophysical and Astrophysical Fluid Dynamics*, *84*, 127–163, doi:10.1080/03091929708208976.

Roudier, T., Švanda, M., Rieutord, M., Malherbe, J. M., Burston, R., and Gizon, L. (2014), Structure and evolution of solar supergranulation using sdo/hmi data, *Astronomy and Astrophysics*, *567*, A138, doi:10.1051/0004-6361/201423577.

Santos, J. C., J. Büchner, and A. Otto (2011), Development of electric currents in a magnetic field configuration containing a magnetic null point, *Astronomy and Astrophysics*, *525*, A3, doi:10.1051/0004-6361/201014758.

Saur, J. (2004), Turbulent Heating of Jupiter's Middle Magnetosphere, *The Astrophysical Journal*, *602*, L137–L140, doi:10.1086/382588.

Schatten, K. H., J. M. Wilcox, and N. F. Ness (1969), A model of interplanetary and coronal magnetic fields, *Solar Physics*, *6*, 442–455, doi:10.1007/BF00146478.

Schindler, K., and J. Birn (1993), On the cause of thin current sheets in the near-earth magnetotail and their possible significance for magnetospheric substorms, *Journal of Geophysical Research: Space Physics*, *98*(A9), 15,477–15,485, doi:10.1029/93JA01047.

Schindler, K., M. Hesse, and J. Birn (1988), General magnetic reconnection, parallel electric fields, and helicity, *Journal of Geophysical Research: Space Physics*, *93*(A6), 5547–5557, doi:10.1029/JA093iA06p05547.

Schwarzschild, M. (1959), Photographs of the Solar Granulation Taken from the Stratosphere., *The Astrophysical Journal*, *130*, 345, doi:10.1086/146725.

Seehafer, N. (1978), Determination of constant α force-free solar magnetic fields from magnetograph data, *Solar Physics*, *58*(2), 215–223.

Seki, K., A. Nagy, C. M. Jackman, F. Crary, D. Fontaine, P. Zarka, P. Wurz, A. Milillo, J. Slavin, D. Delcourt, M. Wiltberger, R. Ilie, X. Jia, S. Ledvina, M. Liemohn, and R. W. Schunk (2015), A review of general physical and chemical processes related to plasma sources and losses for solar system magnetospheres, *Space Science Reviews*, *192*, doi:10.1007/s11214-015-0170-y.

Sergis, N., C. M. Jackman, A. Masters, S. M. Krimigis, M. F. Thomsen, D. C. Hamilton, D. G. Mitchell, M. K. Dougherty, and A. J. Coates (2013), Particle and magnetic field properties of the saturnian magnetosheath: Presence and upstream escape of hot magnetospheric plasma, *Journal of Geophysical Research: Space Physics*, *118*(4), 1620–1634, doi:10.1002/jgra.50164.

Smith, E. J. (1973), Observed properties of interplanetary rotational discontinuities, *Journal of Geophysical Research*, *78*(13), 2088–2093, doi:10.1029/JA078i013p02088.

Sonnerup, B. U. Ö. (1979), *Magnetic Field Reconnection*, vol. 3, pp. 45–108.

Sonnerup, B. U. Ö., I. Papamastorakis, G. Paschmann, and H. Lühr (1987), Magnetopause properties from ampte/irm observations of the convection electric field: Method development, *Journal of Geophysical Research: Space Physics*, *92*(A11), 12,137–12,159, doi:10.1029/JA092iA11p12137.

Sonnerup, B. U. Ö., G. Paschmann, and T.-D. Phan (1995), Fluid Aspects of Reconnection at the Magnetopause: In Situ Observations, *Washington DC American Geophysical Union Geophysical Monograph Series*, *90*, 167, doi:10.1029/GM090p0167.

Sonnerup, B. U. ., G. Paschmann, I. Papamastorakis, N. Sckopke, G. Haerendel, S. J. Bame, J. R. Asbridge, J. T. Gosling, and C. T. Russell (1981), Evidence for magnetic field reconnection at the earth's magnetopause, *Journal of Geophysical Research: Space Physics*, *86*(A12), 10,049–10,067, doi:10.1029/JA086iA12p10049.

Sulaiman, A. H., X. Jia, N. Achilleos, N. Sergis, D. A. Gurnett, and W. S. Kurth (2017), Large-scale solar wind flow around saturn's nonaxisymmetric magnetosphere, *Journal of Geophysical Research: Space Physics*, *122*(9), 9198–9206, doi:10.1002/2017JA024595, 2017JA024595.

Swift, D. W. (1995), Use of a hybrid code to model the earth's magnetosphere, *Geophys. Res. Lett.*, *22*, 311.

Swift, D. W. (1996), Use of a hybrid code for global-scale plasma simulation, *J. Comput. Phys.*, *126*, 109.

Swisdak, M., B. Rogers, J. F. Drake, and M. Shay (2003), Diamagnetic suppression of component magnetic reconnection at the magnetopause, *J. Geophysical Research*, *108*, doi: 10.1029/2002JA009726.

Tao, C., F. Sahraoui, D. Fontaine, J. de Patoul, T. Chust, S. Kasahara, and A. Retinò (2015), Properties of jupiter's magnetospheric turbulence observed by the galileo spacecraft, *Journal of Geophysical Research: Space Physics*, *120*(4), 2477–2493, doi: 10.1002/2014JA020749, 2014JA020749.

Thieme, K. M., R. Schwenn, and E. Marsch (1989), Are structures in high-speed streams signatures of coronal fine structures?, *Advances in Space Research*, *9*(4), 127 – 130, doi: https://doi.org/10.1016/0273-1177(89)90105-1.

Thomsen, M. F., and D. M. Delapp (2005), Numerical moments computation for CAPS/IMS, *Report la ur 05 1542*, Los Alamos National Laboratory.

Thomsen, M. F., D. B. Reisenfeld, D. M. Delapp, R. L. Tokar, D. T. Young, F. J. Crary, E. C. Sittler, M. A. McGraw, and J. D. Williams (2010), Survey of ion plasma parameters in Saturn's magnetosphere, *Journal of Geophysical Research (Space Physics)*, *115*, 10,220–+, doi:10.1029/2010JA015267.

Titov, V. S., G. Hornig, and P. Démoulin (2002), Theory of magnetic connectivity in the solar corona, *Journal of Geophysical Research: Space Physics*, *107*(A8), SSH 3–1–SSH 3–13, doi:10.1029/2001JA000278.

Torbert, R. B., C. T. Russell, W. Magnes, R. E. Ergun, P.-A. Lindqvist, ..., and K. Lappalainen (2016), The fields instrument suite on mms: Scientific objectives, measurements, and data products, *Space Science Reviews*, *199*(1), 105–135, doi:10.1007/s11214-014-0109-8.

Tu, C.-Y., and E. Marsch (1990), Evidence for a "background" spectrum of solar wind turbulence in the inner heliosphere, *Journal of Geophysical Research: Space Physics*, *95*(A4), 4337–4341, doi:10.1029/JA095iA04p04337.

Tu, C.-Y., and E. Marsch (1993), A model of solar wind fluctuations with two components: Alfvén waves and convective structures, *Journal of Geophysical Research: Space Physics*, *98*(A2), 1257–1276, doi:10.1029/92JA01947.

Tu, C.-Y., C. Zhou, E. Marsch, L.-D. Xia, L. Zhao, J.-X. Wang, and K. Wilhelm (2005), Solar wind origin in coronal funnels, *Science*, *308*(5721), 519–523, doi:10.1126/science.1109447.

Vasyliunas, V. M. (2015), *Magnetotail: Unsolved Fundamental Problem of Magnetospheric Physics*, pp. 1–19, John Wiley and Sons, Inc, doi:10.1002/9781118842324.ch1.

Viall, N. M., H. E. Spence, and J. Kasper (2009), Are periodic solar wind number density structures formed in the solar corona?, *Geophysical Research Letters*, *36*(23), doi:10.1029/2009GL041191, l23102.

von Papen, M., J. Saur, and O. Alexandrova (2014), Turbulent magnetic field fluctuations in saturn's magnetosphere, *Journal of Geophysical Research: Space Physics*, *119*(4), 2797–2818, doi:10.1002/2013JA019542.

Walén, C. (1944), On the Theory of Sunspots, *Arkiv for Matematik, Astronomi och Fysik*, *30*, 1–87.

Wilhelm, K., L. Abbo, F. Auchère, N. Barbey, L. Feng, A. H. Gabriel, S. Giordano, S. Imada, A. Llebaria, W. H. Matthaeus, G. Poletto, N.-E. Raouafi, S. T. Suess, L. Teriaca, and Y.-M. Wang (2011), Morphology, dynamics and plasma parameters of plumes and interplume regions in solar coronal holes, *The Astronomy and Astrophysics Review*, *19*(1), 35, doi:10.1007/s00159-011-0035-7.

Wilson, R. J., R. L. Tokar, M. G. Henderson, T. W. Hill, M. F. Thomsen, and D. H. Pontius (2008), Cassini plasma spectrometer thermal ion measurements in Saturn's inner magnetosphere, *Journal of Geophysical Research (Space Physics)*, *113*, 12,218–+, doi:10.1029/2008JA013486.

Wilson, R. J., P. A. Delamere, F. Bagenal, and A. Masters (2012), Kelvin-Helmholtz instability at Saturn's magnetopause: Cassini ion data analysis, *Journal of Geophysical Research (Space Physics)*, *117*, A03212, doi:10.1029/2011JA016723.

Wing, S., J. R. Johnson, C. C. Chaston, M. Echim, C. P. Escoubet, B. Lavraud, C. Lemon, K. Nykyri, A. Otto, J. Raeder, and C.-P. Wang (2014), Review of solar wind entry into and transport within the plasma sheet, *Space Science Reviews*, *184*(1), 33–86, doi: 10.1007/s11214-014-0108-9.

Yamada, M. (2011), Understanding the dynamics of magnetic reconnection layer, *Space Science Reviews*, *160*, 25–43, doi:10.1007/s11214-011-9789-5.

Yang, L., J. He, H. Peter, C. Tu, W. Chen, L. Zhang, E. Marsch, L. Wang, X. Feng, and L. Yan (2013), Injection of Plasma into the Nascent Solar Wind via Reconnection Driven by Supergranular Advection, *The Astrophysical Journal*, *770*, 6, doi:10.1088/0004-637X/770/1/6.

Yao, Y., C. C. Chaston, K.-H. Glassmeier, and V. Angelopoulos (2011), Electromagnetic waves on ion gyro-radii scales across the magnetopause, *Geophysical Research Letters*, *38*(9), doi:10.1029/2011GL047328.

Yee, K. (1966), Numerical solution of inital boundary value problems involving Maxwell's equations in isotropic media, *IEEE Transactions on Antennas and Propagation*, *14*, 302–307, doi:10.1109/TAP.1966.1138693.

Young, D. T., J. J. Berthelier, M. Blanc, J. L. Burch, A. J. Coates , ..., and C. Zinsmeyer (2004), Cassini plasma spectrometer investigation, *Space Science Reviews*, *114*(1), 1–112, doi:10.1007/s11214-004-1406-4.

Zhang, B., P. A. Delamere, X. Ma, B. Burkholder, M. Wiltberger, J. G. Lyon, V. G. Merkin, and K. A. Sorathia (2018), Asymmetric Kelvin-Helmholtz Instability at Jupiter's Magnetopause Boundary: Implications for Corotation-Dominated Systems, *Geophys. Res. Lett.*, *45*, 56–63, doi:10.1002/2017GL076315.

Zurbuchen, T. H. (2007), A new view of the coupling of the sun and the heliosphere, *Annual Review of Astronomy and Astrophysics*, *45*(1), 297–338, doi: 10.1146/annurev.astro.45.010807.154030.